

The Electrical Properties of Interfacial Double Layers

A thesis
submitted in partial fulfilment
of the requirements for the Degree
of
Doctor of Philosophy
at the
University of Waikato
by

Mark Hedley Jones



THE UNIVERSITY OF
WAIKATO
Te Whare Wānanga o Waikato

University of Waikato
2011

Abstract

When a solid comes in contact with a liquid, an interfacial double-layer is likely to form. They are too small to feel or see so their presence goes mostly unnoticed at the macroscopic level. Double layers stabilise some of our most important fluids – blood, milk, paints, and inks. Without the protection of double-layers, these mixtures clump and lose their fluidity.



This thesis looks at both electricity generation and the electrical impedance of interfacial double layers.



This thesis is separated into two parts, both linked to the behaviour of double-layers. In part I these layers are used as a means of converting fluid-mechanical energy into electrical energy. The primary application of such a harvester would be to power electronic water meters. Domestic water meters are typically installed where electrical connection is not feasible; harvesting energy here may make electronic metering more feasible long-term. My findings show that double layer based energy harvesters are not efficient enough for this application yet. Recent literature on the subject suggests large gains in efficiency may be possible using more exotic materials.

Part II models the electrical impedance of submerged electrodes. Double-layers play a large part in determining the electrical impedance between metal-fluid interfaces. This work is important to designers of medical implants; and by extension, anybody who relies on the implants themselves. Engineers use solutions of saline to mimic the environment experienced by their implants once implanted. This gives them a way to test the implant without injuring anyone. A way of characterising the interface between electrodes in solution is to model it mathematically. Such a model was created by my supervisor, Jonathan Scott. I use that model to compare electrodes placed in solutions of saline to those placed in a living animal. Measurements of the two show they are quite different from one another. I create a mixture using low-cost ingredients that closely resembles the electrical impedance of a live animal.

Acknowledgement

Thanks to Jonathan Scott (my chief supervisor), Steve Newcombe (Waikato University's award winning glass blower) and Peter Single (the senior electrical engineer at Saluda Medical) for their time, resources and patience. Thank you to my second supervisor, Marcus Wilson, for checking up every so often and help proof-reading. Thanks also go to the University of Waikato for a funding the first three years of this work with a Waikato Doctoral Scholarship. Without this funding I could not have undertaken this research. The support of my partner, Sarah, and my mother, Gina, has kept me on track. Lastly, thank you to everyone who has contributed to open-source projects, especially those part of:

- The Linux kernel and GNU tools
- Gnome desktop environment
- Inkscape vector drawing software
- Gimp image manipulation program
- The Arch Linux distribution
- \TeX and its derivative \LaTeX
- Python
- ngSpice

Work done throughout this thesis has relied heavily on these tools.

Contents

Abstract	i
Acknowledgement	ii
1 Introduction	1
1.1 Motivation	2
1.2 Statement of Originality	4
1.3 Publications arising from this work	4
1.4 Thesis Outline	5
2 Backgound	6
2.1 Double Layers	6
2.1.1 Formation	6
2.1.2 Physical Model	8
2.1.3 Anatomy	11
2.2 Streaming Cells	13
2.2.1 Literature Review	17
2.3 Impedance Modelling	23
I Double Layers on Insulators: Harvesting Energy	27
3 Streaming Cell Energy Harvesting	28
3.1 General Analysis	28
3.1.1 Mathematics	28
3.1.2 Electrical model	31
3.1.3 Optimisation	31
3.2 Building a Streaming Cell	36
3.2.1 First streaming cells	36
3.2.2 Robust streaming cells	39
3.3 Measurements	41

3.3.1	Experimental setup	41
3.3.2	Measurement issues	43
3.4	Results	45
3.4.1	Streaming voltage versus pressure	46
3.4.2	Output power versus load resistance	48
3.5	Discussion	48
3.6	Concluding remarks	52
4	Applicability to Water Metering	54
4.1	Current Trends in Water Metering	55
4.2	Envisioned harvester design	57
4.3	Quantifying harvestable energy	59
5	A Harvester's Energy Requirements	65
5.1	Microcontrollers	65
5.1.1	Selection of appropriate controllers	66
5.1.2	Power consumption benchmarks	66
5.1.3	Non-volatile memory	79
5.1.4	Analog-to-digital conversions.	80
5.2	Wireless Transmission	80
5.3	Total Energy Requirements	83
6	Conclusion	85
II	Double Layers on Conductors: Electrical Impedance	87
7	An Interfacial Model In The Electrical Domain	88
7.1	The Scott-Single Interface Model	88
7.1.1	The interface model	89
7.1.1.1	Interface series resistance: Resistor	90
7.1.1.2	Polar effects: Constant phase element	90
7.1.1.3	Faradaic reactions: diodes	93
7.1.1.4	Species depletion: memristors	95
7.1.2	Inter-electrode resistivity	97
7.2	Electrolyte: Phosphate Buffered Saline	98
7.3	Methods Of Parameter Extraction	100
7.3.1	Resistivity	101
7.3.2	Constant phase element and series resistance	102
7.3.3	Faradaic currents	103

8 Interface Parameters	106
8.1 Phosphate Buffered Saline	106
8.1.1 Resistor Mesh	107
8.1.2 Series Resistance And Constant Phase Element	109
8.1.3 Faradaic Current	116
8.1.3.1 Step based Faradaic measurements	118
8.1.3.2 Successful measurement of the Faradaic currents	120
8.1.4 Final Model	124
8.2 Biological parameter measurements	125
8.2.1 Resistor Mesh	127
8.2.2 Series Resistance And Constant Phase Element	129
8.2.3 Faradaic Current	133
8.2.4 Final Model	133
9 Recipes For Fluid Mimicry	135
9.1 Measurements	136
9.1.1 Configuration	136
9.1.2 Procedure	136
9.1.3 Ingredients Tried	138
9.1.4 Results	140
9.1.5 Discussion	144
III Appendices	147
A Charged Droplet Energy Harvester	148
A.1 How charge is generated	148
A.2 Replicating the experiment	151
A.3 Optimising output	151
A.3.1 Drop volume and frequency	151
A.3.2 Scale	158
B Streaming Cell Voltage Measurements	161
C Microprocessor Power Measurements	167
C.1 Measurement scripts	167
C.1.1 E5270 Scripts	167
C.2 Measurement data	167
C.2.1 Chips sleeping	168
C.2.2 Clocking	180
C.3 Microprocessor Test Code	180
C.3.1 ATMEL ATtiny13V and ATtiny25	180

C.3.2 Microchip 12F675	183
C.3.3 Microchip 16F1827	183
C.3.4 Freescale M9S08QG8	189
D Solution Impedance Measurement	191
D.1 Measurement Testing	191
D.1.1 Electrode array measuring resistors	191
D.1.2 Electrode array submerged in distilled water measuring resistors	194
D.1.3 Electrode array submerged in saline measuring resistors	196
Bibliography	199

List of Figures

2.1	Molecular model of the water molecule	6
2.2	Structural formula of a butterfat molecule	8
2.3	Counter-ions are oppositely charged, co-ions have like charge.	8
2.4	Structure of the Helmholtz layer.	9
2.5	Structure of the Goüy-Chapman layer.	10
2.6	Structure of the Goüy-Chapman-Stern layer.	11
2.7	Anatomy of the double layer	12
2.8	Formation of a double layer along a solid wall.	13
2.9	Double layer formation within a streaming cell that is in a state of equilibrium.	14
2.10	Double layer formation within a streaming cell that has a pressure differential applied.	16
2.11	Osterle's electrokinetic pumping cell, reproduced from [40] .	18
2.12	Illustration of hydrodynamic slip inside a channel cavity, where b is the slip length. Arrows indicate flow velocity in each of the three situations.	21
2.13	Diagram of an liquid-solid interface showing various types of molecule configurations, surface imperfections and polar molecules. This diagram is based on the work of Bard et al. [3]	24
2.14	Drawing of an eight electrode array used for spinal stimulation. The electrode is called an Octrode and is made by St. Jude Medical.	25
3.1	Schematic representation, commonly used in electronics, of a streaming cell with attached output resistance	31
3.2	Diagram of a cavitation device, taken from [54], reported to be able to generate over 50 V across its ends by pumping water through it.	36

3.3	Photo of the first generation of streaming device built, by summer research student Jonathon McMullan, to create the streaming voltages reported by Varga and Seymour.	37
3.4	Photo showing two examples of a second design of streaming cell made entirely from glass.	37
3.5	Photo showing half of a glass slide glued to acrylic base plate	40
3.6	Photo showing plastic shims sandwiched between two slide halves	40
3.7	Photo showing final assembly	40
3.8	Circuit diagram of the differential pressure sensor bridge circuit (taken from [23])	42
3.9	Diagram of equipment setup while measuring power output from the streaming cell harvesters	44
3.10	Plot showing un-adjusted streaming voltages versus applied pressure.	46
3.11	Plot showing adjusted streaming voltages versus applied pressure.	47
3.12	Scatter plot of voltage/pressure gradient versus channel height for each of the measured channels.	47
3.13	Plot of output power versus effective load resistance for a 71 µm high channel at a pressure of 260 kPa.	49
3.14	Measured data from Gu and Li's paper on streaming cells relating the streaming voltage and pressure differential to the channel height with distilled water as the working fluid . .	50
3.15	Measured data from Gu and Li's paper on streaming cells relating the streaming voltage and pressure differential to the channel height with a 1 mmol sodium chloride solution as the working fluid	51
3.16	Scatter plot with results of streaming cell measurements in terms of those made by Gu and Li [61] (for comparison). . .	51
4.1	Photograph of a domestic water meter, and installation, (Kent PSMT 25mm) typical of an Auckland residential area.	56
4.2	Photograph of the a wireless transmitting module from Waterware NZ. The device attaches to a compatible water meter and contains its own battery [35].	57
4.3	Diagram showing the intended design of streaming cell harvester suitable for domestic connection.	58
4.4	Sample profile showing constructed instances of washing machine use, a shower and a toilet flush. The washing machine's wash and rinse cycles are separated in time.	60

4.5	Log-log graph showing the pressure developed across the Kent PSM series mechanical water meters. Taken from [17].	61
4.6	Graph showing fitted curve to the pressure loss graph presented as fig. 4.5.	61
4.7	Calculated power dissipation by a typical domestic mechanical water meter for each of the sample profile events.	62
4.8	Profile of power dissipation within a mechanical water meter over a week for a two occupant dwelling.	63
5.1	Current consumed by investigated MCUs while in sleep mode.	68
5.2	Power consumed by the PIC16F1827 while processing	72
5.3	Power consumed by the PIC16F688 while processing	72
5.4	Power consumed by the PIC12F675 while processing	73
5.5	Power consumed by the ATtiny25V while processing	73
5.6	Power consumed by the ATtiny13V while processing	74
5.7	Power consumed by the MC9S08QG8 while processing	74
5.8	Per instruction cycle energy consumption comparison	76
5.9	Per instruction cycle energy consumption of the ATtiny13V	77
5.10	MCU comparison of instructions taken to complete a benchmark.	78
5.11	Energy consumed by each MCU per non-volatile erase/write operation.	79
5.12	Energy consumed by each MCU per ADC measurement.	81
5.13	Power draw from a HopeRF RFM12B transceiver module.	82
5.14	Power draw from a Digi International Xbee Series 2 transceiver module.	83
7.1	Electrodes submerged in an electrolyte solution, such a system can be described by the Scott-Single Interface Model.	89
7.2	Connection diagram of two electrodes (with their interface models) connected together by the resistivity of an electrolyte solution.	89
7.3	Electrical schematic of the electrode-electrolyte interface	90
7.4	Ralph Morrison's implementation of a constant phase element using an infinite array of resistor-capacitor pairs (taken from Morrison's paper – [38]).	91
7.5	Graph showing how a non 20 dB per frequency decade	92
7.6	Electrical symbol of a memristor, as is used in the original electrode-electrolyte interface model	95
7.7	Electrical schematic of the electrode-electrolyte interface without memristors (as used throughout this thesis)	96

7.8	St. Jude Medical Octrode. An eight electrode array commonly used in spinal stimulation implants. The electrode numbering shown here will be used throughout this work.	97
7.9	Resistor mesh used to model the electrical resistance between interface pairs. R_{li} is longitudinal resistance, R_{sri} and R_{eri} is the radial resistance for the spacers and electrodes respectively, and I is an interface.	99
7.10	Measurement schematic of trans-impedance measurements where electrodes eight and one are driven and the remainder are used in voltage differential measurements.	101
7.11	Measurement schematic of trans-impedance measurements where electrodes two and one are driven and the remainder are used in voltage differential measurements.	101
7.12	Log-log plot of frequency vs impedance magnitude of a single interface and inter-electrode impedance. The response of the CPE and that of the total series resistance is separated in the frequency domain.	103
8.1	Illustration of one of two measurement configurations used to measure the electrode transimpedances. Each of the electrode pairs were measured one-after-the-other using the shown equipment.	108
8.2	Measured and fitted values of trans-impedance for both measurement configurations. Voltage measurements are made between adjacent pairs of electrodes as current is pushed through the stimulus electrodes.	108
8.3	Illustrated voltage gradient in electrolyte solution at each electrode's surface when potential is applied across electrodes two and seven. Measurement of electrolyte voltage taken between electrodes 2 and 3.	110
8.4	Diagram showing the measurement configuration used to measure the CPE response and interface series resistance. . .	111
8.5	Impedance magnitude of both the measured interface response and the fitted response at each of the six concentrations of PBS.	111
8.6	Impedance phase of both the measured interface response and the fitted response at each of the six concentrations of PBS.	112
8.7	The SPICE model schematic used to find optimum values for parameters of the CPE and interface series resistance. Parameters for the resistor mesh are those determined previously. .	113

8.8 Plot showing fitted parameter values for the CPE impedance magnitude at 50 mHz and series resistance at each of the six concentrations of PBS (shown as markers). The solid trace shows the resulting fit between those values as a function of concentration.	114
8.9 Illustration of the cyclic voltammetry measurement configuration used to measure the response of the interface when driven into Faradaic conduction mode.	115
8.10 Graph showing measured Faradaic response of each concentration of PBS to a linearly increasing voltage between electrodes two and seven.	116
8.11 Graph showing measured response of two interfaces to a multiple step responses. Vertical dotted lines indicate when in time the step occurred. Dotted traces show points in time after each response. Measurements are between electrodes two and seven on the Octrode submerged in 1X PBS.	118
8.12 Graph showing CPE discharge curve after a step transition between each of voltage trace in increasing order. Measurements are between electrodes two and seven on the Octrode submerged in 1X PBS. A delay of 10 000 seconds elapsed between each step.	119
8.13 Graph showing measurements of four concentrations of PBS as each is stepped from 0.55 V to 0.95 V. Measurements are between electrodes two and seven on the Octrode. A delay of 64 seconds elapsed between each step. Dotted traces connect current measurements taken 10 s after each step.	120
8.14 Graph showing the electrical current draw associated with Faradaic reactions versus applied electrode overpotential. Measurements used the stepped method with a wait time of 64 s between transitions. Vertical bars mark the standard deviation of the final fourty measurements before the following step.	121
8.15 Graph comparing measured Faradaic response of a pair of interfaces (1.0X PBS) to the simultated response using fitted parameter values for i_0 and n . Each spike is a step in electrode overpotential, with the steps shown in the following graph.	122
8.16 Graph comparing the measured settled electrical currents of Faradaic reactions (in 1.0X PBS) for a pair of interfaces to simulated final values using the fitted parameter values for i_0 and n	123

8.17 Schematic of the electrode-electrolyte interface including parameter values for platinum and buffered saline.	124
8.18 Diagram showing the positioning of the St. Jude Medical Octrode electrode array inside the sheep spinal cavity.	125
8.19 Graph showing measured and simulated impedance magnitude for twenty five combinations of stimulus-measure pairs of electrodes.	127
8.20 Graph showing measured and simulated impedance phase for twenty five combinations of stimulus-measure pairs of electrodes.	128
8.21 Graph showing measured CPE impedance magnitude response before and after termination.	130
8.22 Graph showing measured CPE impedance phase response before and after termination.	130
8.23 Graph showing average CPE response in live sheep compared to the six solutions of PBS, visible as the grey traces, and simulated response based on fitted parameters.	131
8.24 Graph showing average CPE response in a live sheep's spinal cavity compared to six concentrations of PBS, visible as grey traces, and simulated response based on fitted parameters. .	132
9.1 Diagram showing the measurement configuration used to measure the CPE response and resistivity of mixed solutions	137
9.2 Diagram showing the execution of the measurement script .	139
9.3 Plot of impedance magnitude versus frequency (log-log) for distilled water.	140
9.4 Plot of impedance phase versus frequency (log-log) for distilled water.	141
9.5 Plot of impedance magnitude versus frequency (log-log) for 250 g cornflour mixed with 175 ml distilled water.	141
9.6 Plot of impedance phase versus frequency (log-log) for 250 g cornflour mixed with 175 ml distilled water.	142
9.7 Plot of impedance magnitude versus frequency (log-log) for 250 g cornflour mixed with 175 ml distilled water and 1.9 g table-salt.	142
9.8 Plot of impedance phase versus frequency (log-log) for 250 g cornflour mixed with 175 ml distilled water and 1.9 g table-salt.143	143
9.9 Plot of impedance magnitude versus frequency (log-log) for 250 g cornflour mixed with 180 ml distilled water and 1.9 g table-salt.	143
9.10 Plot of impedance phase versus frequency (log-log) for 250 g cornflour mixed with 180 ml distilled water and 1.9 g table-salt.144	144

9.11 Plot of impedance magnitude versus frequency (log-log) for 190 g cornflour mixed with 190 ml distilled water and 0.858 g table-salt.	145
9.12 Plot of impedance phase versus frequency (log-log) for 190 g cornflour mixed with 190 ml distilled water and 0.858 g table-salt.	145
A.1 Drawing of Lord Kelvin's electrostatic generator.	149
A.2 Drawing of the charging mechanism for Lord Kelvin's electrostatic generator	149
A.3 Simplified diagram of Lord Kelvin's water dropper configuration	150
A.4 Photo of experimental setup for charge on drip measurements.	152
A.5 Diagram of experimental setup for charge on drip experiments	153
A.6 Photo of the dropper and high voltage inductor.	154
A.7 Syringe pump used to produce drops and control flow rate.	155
A.8 Charge on drip versus drip volume for a fixed induction voltage of 2.5 kV.	155
A.9 Charge per volume versus drop volume for a fixed induction voltage of 2.5 kV.	156
A.10 Charge on drip versus ring induction voltage for a fixed drip volume	157
A.11 Current versus flow rate for an induction voltage of 3.8 kV and drop volume of 3.1 μL	158
A.12 Diagram of the electrostatic force and gravity acting on a drop of water.	159
B.1 Graph showing the voltage output with applied pressure differential across a 26 μm glass micro-channel (38 mV offset added)	162
B.2 Graph showing the voltage output with applied pressure differential across a 52 μm glass micro-channel (23 mV offset added)	162
B.3 Graph showing the voltage output with applied pressure differential across a 56 μm glass micro-channel (405 mV offset added)	163
B.4 Graph showing the voltage output with applied pressure differential across a 71 μm glass micro-channel (44 mV offset added)	163
B.5 Graph showing the voltage output with applied pressure differential across a 75 μm glass micro-channel (20 mV offset added)	164

B.6	Graph showing the voltage output with applied pressure differential across a 106 µm glass micro-channel (56 mV offset added)	164
B.7	Graph showing the voltage output with applied pressure differential across a 125 µm glass micro-channel (5 mV offset added)	165
B.8	Graph showing the voltage output with applied pressure differential across a 161 µm glass micro-channel (23 mV offset added)	165
B.9	Graph showing the voltage output with applied pressure differential across a 178 µm glass micro-channel (13 mV offset added)	166
B.10	Graph showing the voltage output with applied pressure differential across a 245 µm glass micro-channel (27 mV offset added)	166
C.1	Power usage of each microprocessor while in sleep mode	168
C.2	Current consumption of the Atmel ATtiny13V while clocking	172
C.3	Power consumption of the Atmel ATtiny13V while clocking	172
C.4	Energy consumed per instruction for the Atmel ATtiny13V	173
C.5	Current consumption of the Atmel ATtiny25V while clocking	173
C.6	Power consumption of the Atmel ATtiny25V while clocking	176
C.7	Energy consumed per instruction for the Atmel ATtiny25V	176
C.8	Current consumption of the Microchip PIC16F1827 while clocking	179
C.9	Power consumption of the Microchip PIC16F1827 while clocking	179
C.10	Energy consumed per instruction for the Microchip PIC16F1827	180
D.1	Diagram showing the instruments and electrode configuration used to test the measurement setup.	192
D.2	Plot of impedance magnitude versus frequency (log-log) for a 10 kΩ resistor placed between electrodes 1 and 2, and another 10 kΩ resistor placed between electrodes 2 and 5.	193
D.3	Plot of impedance phase versus frequency (log-log) for a 10 kΩ resistor placed between electrodes 1 and 2, and another 10 kΩ resistor placed between electrodes 2 and 5.	193
D.4	Plot of impedance magnitude versus frequency (log-log) for a 10 kΩ resistor placed between electrodes 1 and 2, and another 10 kΩ resistor placed between electrodes 2 and 5. The electrodes and resistors are submerged in distilled water.	194

D.5	Plot of impedance phase versus frequency (log-log) for a 10 k Ω resistor placed between electrodes 1 and 2, and another 10 k Ω resistor placed between electrodes 2 and 5. The electrodes and resistors are submerged in distilled water.	195
D.6	Plot of impedance magnitude versus frequency (log-log) for a 10 k Ω resistor placed between electrodes 1 and 2, and another 10 k Ω resistor placed between electrodes 2 and 5. The electrodes and resistors are submerged in saline.	195
D.7	Plot of impedance phase versus frequency (log-log) for a 10 k Ω resistor placed between electrodes 1 and 2, and another 10 k Ω resistor placed between electrodes 2 and 5. The electrodes and resistors are submerged in saline.	196
D.8	Cut-out from the local newspaper (Hamilton Press) of an article on the streaming cell research conducted during this thesis.	198

List of Tables

3.1	Table of materials used to construct the streaming potential cells	39
3.2	Description of labels used in the streaming cell measurement setup diagram	43
4.1	Average usage characteristics for a shower, washing machine and toilet. Data obtained from [21].	59
4.2	Calculated energy dissipation within a mechanical water meter for a single washing machine cycle, shower and toilet use.	63
4.3	Calculated total energy dissipation over a period of one week within a mechanical water meter for typical use of a washing machine, shower and toilet.	64
5.1	Feature comparison of selected MCUs.	67
5.2	Instruction set size for each tested MCU.	69
5.3	Daily energy expenditure of basic processing functionality .	84
5.4	Daily energy expenditure to transmit 160 characters every six hours	84
7.1	Ingredients used to produce one litre of stock solution of phosphate buffered saline.	99
7.2	Final dilutions of stock to create six 700 ml solutions ranging from 0.025X to 1X standard PBS concentration.	100
7.3	Parameters determined by an optimised fit between a simulated mesh and transimpedance measurements.	102
7.4	Parameters determined from impedance spectroscopy measurements of electrode-electrolyte interface.	104
7.5	Parameters determined from fitting diode parameters to measured response of Faradaic current.	105

8.1	Six PBS concentrations used to fit model parameters to.	107
8.2	Resistor mesh parameters for the electrode array in various concentrations of PBS. Electrolyte conductivity (σ) is expressed in units of S/cm	109
8.3	CPE and R_s parameters. Concentration is relative to the stock solution of phosphate buffered saline.	115
8.4	Faradaic parameters	123
8.5	Table of determined interface parameters for the St. Jude Medical Octrode in PBS.	124
8.6	Table of determined resistor mesh parameters for an electrode array in a live sheep's spinal cavity.	129
8.7	Table of determined interface parameters for an electrode array in a live sheep's spinal cavity.	133
C.1	Raw sleep measurements (Vdd 1.8V – 5.5V)	169
C.2	Atmel ATtiny13V clocking current (Vdd 1.8V – 3.6V).	170
C.3	Atmel ATtiny13V clocking current (Vdd 3.7V – 5.5V).	171
C.4	Atmel ATtiny25V clocking current (Vdd 3.7V – 5.5V)	174
C.5	Atmel ATtiny25V clocking current (VDD 3.7V – 5.5V)	175
C.6	Microchip PIC16F1827 clocking current (Vdd 0V – 3.6V)	177
C.7	Microchip PIC16F1827 clocking current (Vdd 3.7V – 5.5V)	178

Chapter 1

Introduction

Is it possible to harvest energy from water without moving parts? What is the electrical impedance between electrodes in an electrolyte solution? These questions form the basis of this thesis. Although seemingly unrelated, the answer to both lies in behaviour occurring wherever liquid comes into contact with a solid. That behaviour is the formation of arranged layers of liquid against the solid surface, called a double layer. This thesis is separated into two parts; each addressing one of the two questions related to double layers. Part I studies double layers on insulating solids as a means of energy conversion. Methods using these layers as a means of power harvesting are trialled and measured. A particular application of such a harvester is discussed and its feasibility assessed. Part II models the electrical impedance between two electrodes when submerged in an electrolyte. Double layers play a large role this impedance as they dictate the concentration of ions electrode's surface. Measurement of interface impedance allows for direct comparison between a range of environments into which electrodes are placed. This is important when designing an implant that will be placed inside a person. Before introducing background material on interfacial double layers, my motivation for doing this work is discussed. This is

followed by a statement of originality and an outline of the structure of this thesis.

1.1 Motivation

My thesis began with the question “is it possible to harvest energy from water without moving parts?” The purpose for such a harvester is to power an electronic water meter. Doing this without the moving parts of more traditional mechanisms, such as turbines, should increase the harvester’s life expectancy and be generally more robust. I started by looking at three possible harvesting mechanisms;

- piezoelectric vibrators
- electrostatic generators
- streaming potential cells

The piezoelectric vibrator was the equivalent of a water whistle with a vibrational energy harvester attached; the electrostatic generator was a version of Lord Kelvin’s Electrostatic Generator with a harvesting application; and the streaming potential cell was a mystery. We knew geologists used streaming potentials to measure underground water flow. The only thing we knew about the mechanism was that forcing water through something somehow generated a voltage. Learning about that mechanism and answering the following questions started me on the path that became this thesis.

1. Where does streaming voltage come from?
2. What role does the geometry of a streaming device play?
3. Could you change the materials to get more voltage?

After experimentation and energy budgeting, I eventually concluded that streaming cell harvesters are not yet practical. Low conversion efficiency, a susceptibility to clogging and the need for high manufacturing tolerances make them unsuited for domestic water metering. However, this research allowed me to gain a working knowledge of interfacial double layers.

During my doctoral studies my supervisor, Jonathan Scott, took a sabbatical at Saluda Medical in Sydney. At the time, Saluda were developing a medical implant for spinal stimulation. Jonathan and Saluda's senior electronic engineer developed an electrical model of the impedance presented by electrodes immersed in a solution of saline. That model uses electrical components to simulate the electrical impedance between an electrode and an electrolyte. This means it can be entered into electrical simulation software and used to simulate an implanted electrode. Much of the behaviour the model simulates is due to double layers. Saluda's engineers use a dilute solution of phosphate buffered saline to approximate human spinal cavities; into which their electrodes are implanted. They do not know how good this approximation is, it was the most appropriate mixture they had. The alternative is to embed an electrode in a live animal and measure the response - that is also what they do. Live animal experiments are costly and how they differ from solutions of saline is unknown. The interface model is the starting point for the second phase of my research; characterising the interface between an electrode and biological solutions. I leveraged my understanding of interfacial double layers to understand how the model worked, and use it correctly.

1.2 Statement of Originality

Measurements of the energy consumed during an EEPROM write, an ADC measurement, a single instruction being executed, and during sleep mode for six 8-bit microprocessors are my own. The relationship between an electrolyte's conductivity and the impedance of the constant phase element, presented in Part II, is my own. The recipe for a mixture that improves the match between live sheep spine and test solutions such as phosphate buffered saline is my own. The method of measuring Faradaic current that removes the effect of double layer capacitance between electrodes in an electrolyte is my own.

1.3 Publications arising from this work

- Jones, M.H. & Scott, J. (2014). *Scaling of Electrode-Electrolyte Interface Model Parameters In Phosphate Buffered Saline*. Published in IEEE Transactions on Biomedical Circuits and Systems, Issue 99.
- Jones, M.H. & Scott, J. (2014). *Feasibility of Harvesting Power to Run a Domestic Water Meter Using Streaming Cell Technology*. In proceedings of the 21st Electronics New Zealand Conference, ENZCON 2014, Waikato University, Hamilton, New Zealand.
- Jones, M.H. & Scott, J.B. (2011). *The energy efficiency of 8-bit low-power microcontrollers*. In Proceedings of the 18th Electronics New Zealand Conference, ENZCON 2011, Massey University, Palmerston North, 21-22 November 2011, pp. 87-90.

1.4 Thesis Outline

This thesis is broken into two parts. Part I is concerned with energy harvesting with double layers, specifically by the use of streaming cells. Part II measures and models the impedance of an interface, specifically those between implant electrodes. Put simply, Part I deals with double layers on insulating surfaces, and Part II deals with double layers on conductive surfaces.

[[Warning: This is likely to be wrong, the structure is still changing]] The first chapter of I (??) begins with background on streaming cells, followed by a review of related literature. Then in chapter 3, I build and measure the electrical output of ten streaming cells. This is used to determine the energy conversion efficiency of streaming cells fabricated using readily available methods. Next, chapter 4 looks into the possibility of using a streaming cell harvester to power an electronic water meter. The quantity of harvestable energy is estimated by modelling the water consumption in a typical New Zealand home. Chapter 5 looks at the components of an electronic water meter and estimates the amount of energy they are likely to need. Bringing these estimates and measurements together, ?? discusses the feasibility of energy harvesting using streaming cells. Finally, in chapter 6, the work done in part I is summarised and concluding comments are made on the findings.

Part II begins with background material on modelling interface impedance and a literature review, as chapter 1.

Chapter 2

Background

2.1 Double Layers

Modelling and measuring the electrical aspects of interfacial double layers draws on both electronic and chemical concepts. Those with an electronic background are unlikely to be familiar with double layers. This section provides background on what a double layer is and how one is formed, beginning with a discussion of liquids.

2.1.1 Formation

A double layer is an organised layer of liquid; two layers to be precise. Because double layers are a property of liquids, and most common liquids are water based, the properties of water is an appropriate place to start. The following properties of water are not necessary for the formation of

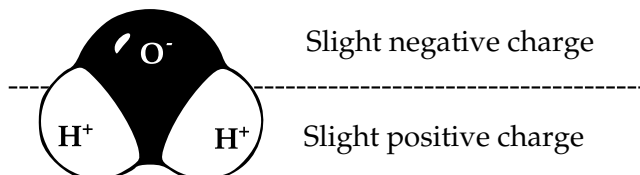


Figure 2.1: Molecular model of the water molecule

double layers, but knowing of them helps build a mental model of the system. At the microscopic scale, individual atoms and molecules within liquids interact with complexity. The density of atoms and molecules in water is extreme, 3.33×10^{22} H₂O molecules per millilitre. These molecules are polar, meaning that one side appears negatively charged while the other appears positively charged, shown in fig. 2.1. This causes them to respond to electric fields by rotating, so as to minimise their potential energy in the field. Because of this, any ions present become surrounded by arranged volumes of water. For example, a positive ion will be surrounded by water molecules orientated such that their hydrogen atoms all point away from the ion. It is also possible for water to spontaneously disassociate from H₂O into a proton (H⁺) and a hydroxide anion (OH⁻).

To form a double layer a liquid containing ions must meet a solid object with charged trapped at its surface. Once this happens, the ions within the liquid are drawn to, or repelled from, the solid's surface. The point where the two states of matter meet is called the interface. Those ions that have been drawn to the interface collect together to form a double layer. Double layers occur when using pure water as the liquid, because of its ability to disassociate, but mostly it is the ions from an electrolyte solution that form the layer [6]. The double layer is simply the collection of ions drawn from a liquid to the surface of a solid.

The term 'solid' may refer to the walls of a container or particulates suspended in solution. When a particulate is suspended throughout a solution it is referred to as an emulsion. For example, milk is such an emulsion of butterfat in water. Figure 2.2 shows the structure of a butterfat molecule; a long structure that behaves as a solid. The stability of an emulsion, such as milk, depends on the strength of the double layers that encapsulate each

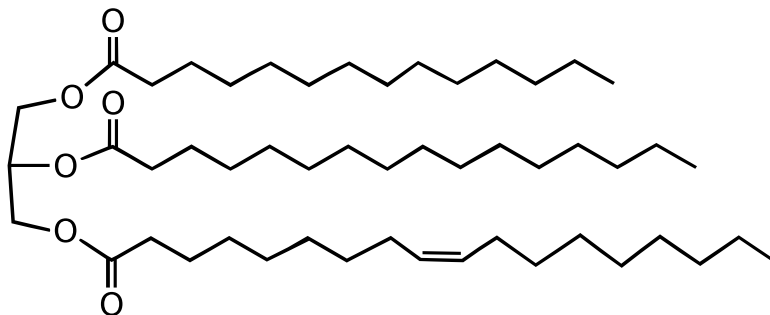


Figure 2.2: Structural formula of a butterfat molecule

- ⊖ counter-ion of ⊕
- ⊕ co-ion of ⊖
- ⊖ counter-ion of ⊗
- ⊗ co-ion of ⊖

Figure 2.3: Counter-ions are oppositely charged, co-ions have like charge.

particle. These double layers shield the molecules or particles from one another electrically. By shielding them from each other they are unable to collect and bond together. This shielding prevents milk from coagulating and turning to lumps.

Having addressed where double layers come from, as well as their organisation, the anatomy of these layers is now introduced.

2.1.2 Physical Model

In the previous section, a brief explanation of what a double layer is and where they form was introduced. We next look at double layer anatomy and define some of its properties. Before moving on, use of the terms ‘co-ion’ and ‘counter-ion’ is defined. These terms refer to ions containing charge – like or opposite – in polarity to a second charge or body of charge. For example, if a negatively charged surface attracts positively charged ions then positive ions are the counter-ion. Likewise, if a positively charged surface

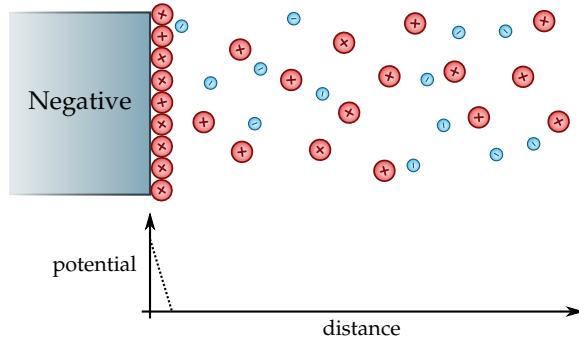


Figure 2.4: Structure of the Helmholtz layer.

was to repel a positive ion then the positive ion is the co-ion. The terms are convenient because they remove the need to identify specific polarities during discussion. This relationship is shown in fig. 2.3.

Three models of the interfacial double layer have been proposed over time. Each represents an extension or modification of the previous, beginning with the Helmholtz Model [24]. Helmholtz proposed his parallel plate capacitor based model in 1879 [19]. His model consists of two layers of surface charge, one inside the solid and one in the liquid. The counter-ions sit in a *compact layer*, meaning that they are bound to the surface and immobile. [45] Figure 2.4 represents this as a row of tightly packed positive ions along the solid surface. Past the layer of bound surface ions there is no effect from the charged surface of the solid. In essence, his model defines the interface a single layer of ions held against the edge of a solid. The problem with this model is its inability to predict the layer's capacitance. Measured capacitance of a double layer depends on the potential difference across the layer, and the concentration of ions in the solution [4]. Helmholtz's model does not account for the dependence of capacitance upon the potential difference and concentration and therefore is not an accurate representation.

Later, Goüy and Chapman independently proposed that charge in the

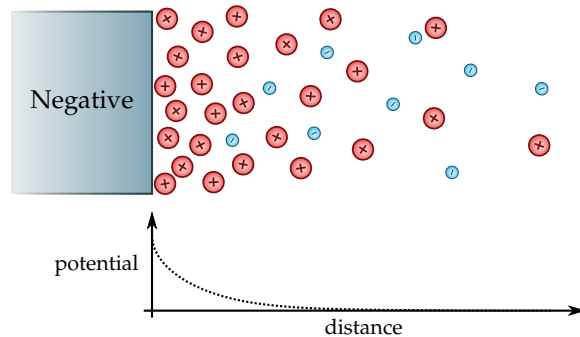


Figure 2.5: Structure of the Goüy-Chapman layer.

liquid phase may instead be held in a *diffuse layer* [11]. This meant that ions in the layer were not fixed and that the density of charge in the layer could vary. Figure 2.5 illustrates the concept by the lack of ions bound to the surface and the gradual decline in counter-ion concentration with distance from the surface. The Goüy-Chapman Model accounts for the observed variation in capacitance by distributing charge in the liquid as a gradient from the surface of the solid. The layer is free to change its concentration profile in response to applied electrostatic potential and ionic concentration. In the case of a higher electrostatic potential, the layer is pulled closer to the surface, becoming shallower. In the case of a higher electrolytic concentration, the layer is more concentrated with a higher charge density, again becoming shallower. It predicts the change in capacitance by growing or shrinking the size of the layer, but it still fails to predict the capacitance at high ionic concentrations. This is in part because it fails to account for the physical size of the ions in the electrolyte and instead models them as point charges [4]. In their model, ions can get infinitely close to the surface regardless of their size. This becomes a problem at high ionic concentration where the surface becomes crowded.

In 1924, Otto Stern published his modified version of the Goüy-Chapman

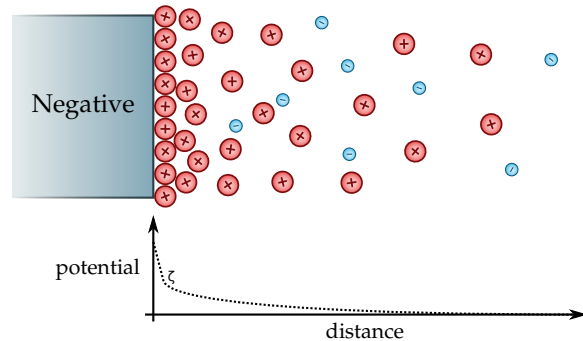


Figure 2.6: Structure of the Goüy-Chapman-Stern layer.

model [49]. This model, illustrated in figure 2.6 extends the Goüy-Chapmam model by setting the minimum distance an ion can get to the solid surface. This effectively reintroduces the compact layer as seen in Helmholtz's model but allows for a concentration gradient exterior to this layer. It resembles the Helmholtz model at high ionic concentration but accounts for spread in the layer dimensions at lower concentrations. The Stern, sometimes referred to as the Goüy-Chapmam-Stern, model is a well accepted double layer model [39].

2.1.3 Anatomy

Figure 2.7 shows the double layer organisation according to the currently accepted Goüy-Chapmam-Stern model. It shows the compact layer adsorbed to the surface of the suspended solid. In this layer the ions are immobile due to the electrical strength at the surface. Surrounding this layer is the diffuse layer. Ions here are still drawn to the solid, but not so strongly as to be immobile. The electric potential in this layer decays from that within the compact layer to the potential in the bulk of the solution. These layers are divided by the shear plane. The shear plane represents nearest distance from the surface at which the layer can move laterally. This is an important pa-

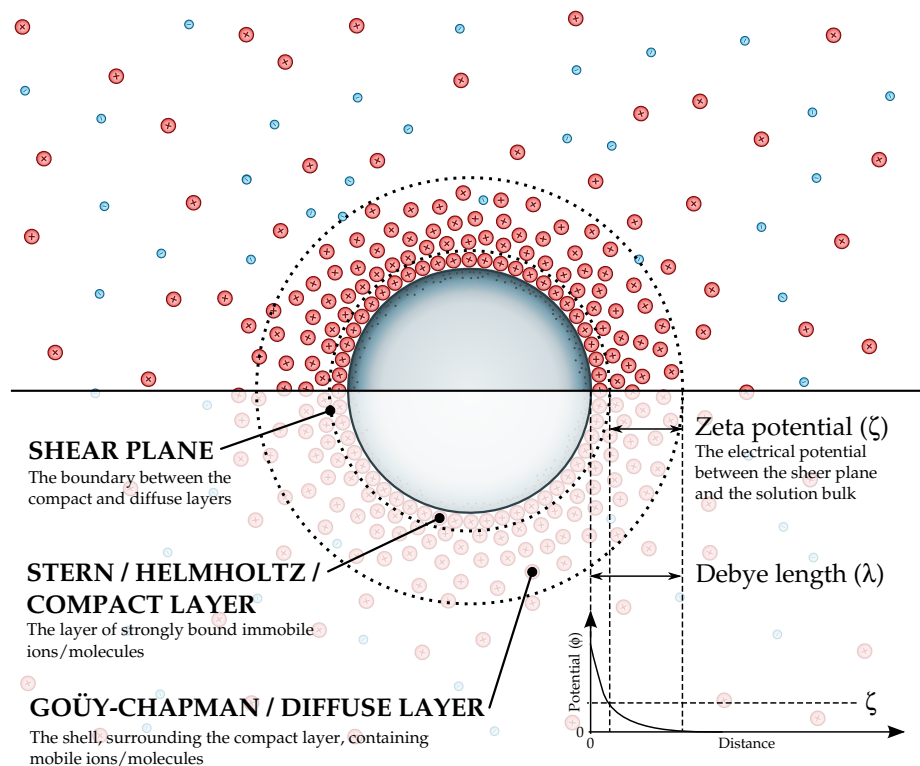


Figure 2.7: Anatomy of the double layer

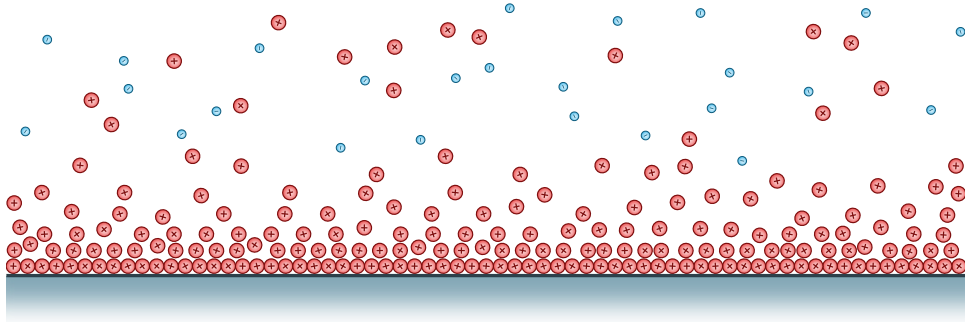


Figure 2.8: Formation of a double layer along a solid wall.

parameter with linear geometries, such as the inside of a pipe, as it represents the true no-slip boundary. The thickness of a typical double layer is between $1 - 100 \text{ nm}$ [26], as defined by its Debye length [25]. The Debye length is the distance between the interface and the point in the liquid where the electric potential is no longer affected by the charged interface. As mentioned in the previous section, this varies based on the ionic concentration of the solution and the potential at the solid surface.

2.2 Streaming Cells

Consider a double layer that has formed along a perfectly flat surface. Figure 2.8 illustrates this situation, where the walls are negatively charged and therefore the counter-ions are positively charged. Counter-ions, separated from the bulk of the liquid, line the exterior of the wall; but charge separation is not enough to generate electrical power.

Energy can not be created or destroyed, it must be converted from one form to another. In this case, counter-ions are electrostatically bound to the interface and removing them requires work. Although the counter-ion density has been increased at the boundary, the charge is not free. Migration of charge to the walls ceases once the surface potential has been neutralised.

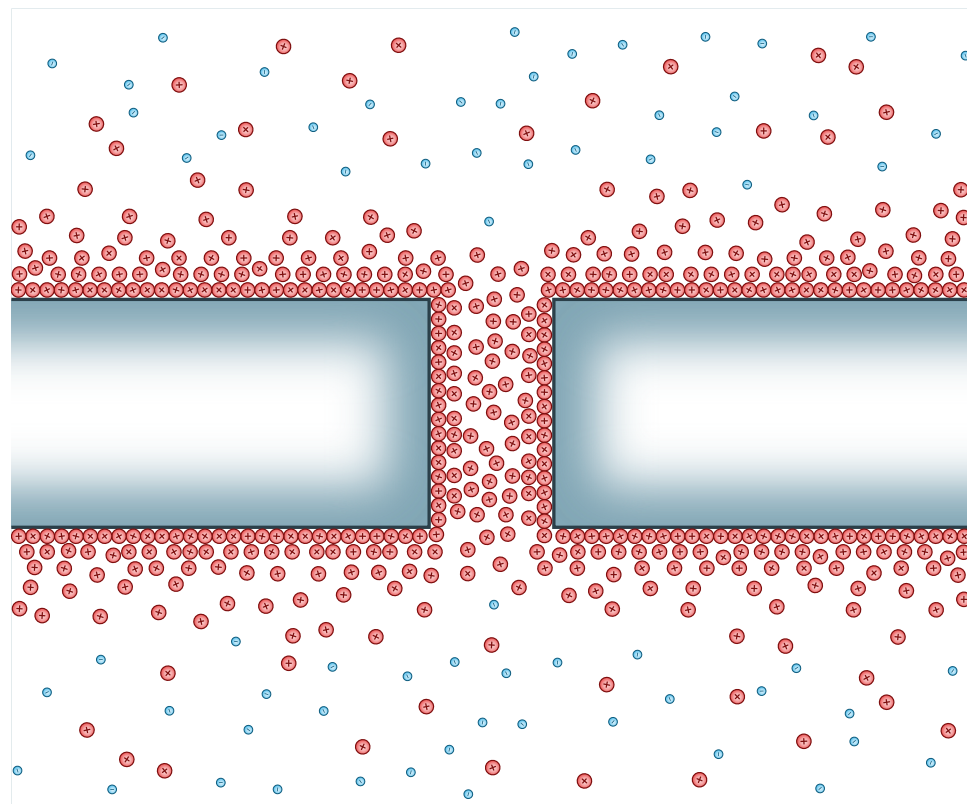


Figure 2.9: Double layer formation within a streaming cell that is in a state of equilibrium.

Double layer formation takes work to undo and the process stops once the layer is formed. Generating electrical energy requires taking some form of power from the fluid, in this case mechanical. Liquids pass mechanical power in the form combination a pressure and a flow. Harvesting power from liquid will cause a drop in pressure as liquid is pushed through the harvesting mechanism. The mechanisms presented here use mechanical power to shift the ionic balance between two bodies of liquid. This means separating and isolating negative and positive ions from each other. Figure 2.9 shows another charged wall, but with the addition of a small channel. Notice that the channel contains no co-ions, it is exclusively occupied by counter-ions. The ratio of counter-ions to co-ions within the channel is controlled by the width of the channel. The narrower the channel, the less likely it is for co-ions to get inside. This channel is small enough that the layers overlap one another, repelling co-ions. The channel and the two separated bodies of liquid now form an energy harvester. Counter-ion rich fluid is transported across the channel by applying a pressure differential. As counter-ions exit the channel on the low-pressure side, new ions move to replenish the double layer on the high-pressure side. A diagram showing the channel geometry, but with pressure applied and a voltage gradient generated is shown as figure 2.10. The two walls and channel is referred to as a streaming cell. Streaming cells are able to continuously separate ions of an electrolyte fluid. Electrical potential across a streaming cell increases as those ions are pumped through. This only works when the solid surface has charge at its surface, necessary to form the double layer.

A channel can be created individually using a range of fabrication methods, such as chemical etching or using narrowly separated parallel plates. They can also be formed en masse by using porous materials such as glass

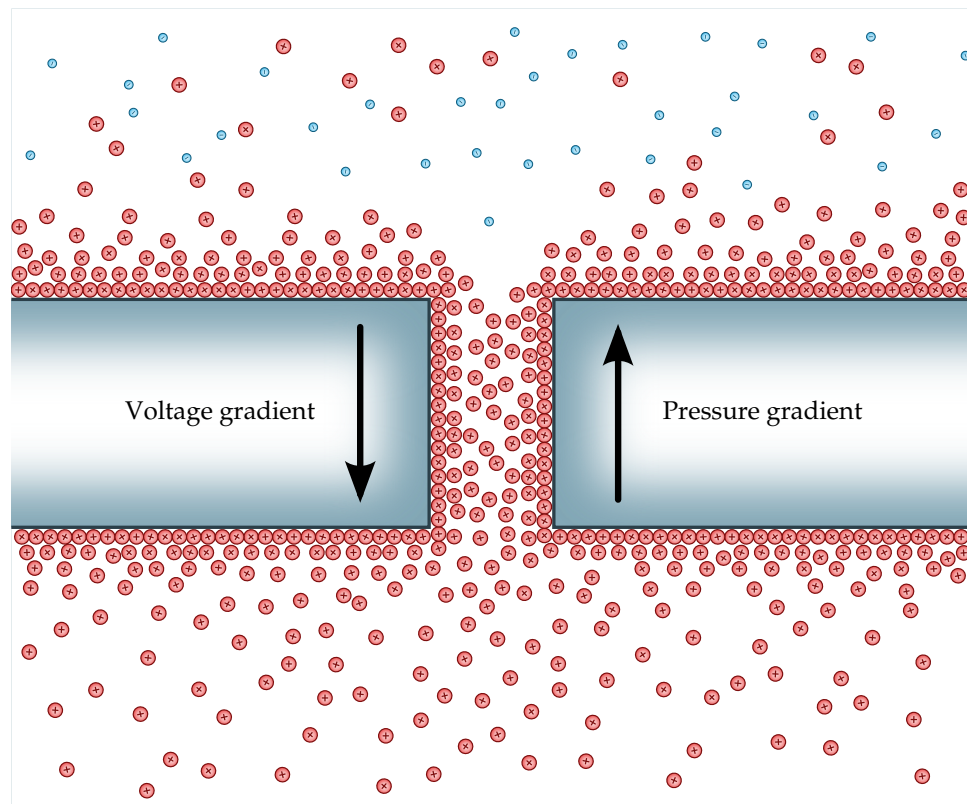


Figure 2.10: Double layer formation within a streaming cell that has a pressure differential applied.

or ceramics, where the pores themselves act as channels. Glass has the convenient property that it spontaneously obtains a negative surface charge when in contact with water, the requirement for double layer formation. This surface charge is caused by the deprotonation of surface silanol groups in glass ($\text{SiOH} \rightleftharpoons \text{SiO}^- + \text{H}^+$) [27]. By immersing a glass channel in an electrolyte solution, the glass donates protons into the solution leaving its surface negatively charged. In turn, positively charged double layers line the channel's inner walls ready to be pumped through the channel. This means that glass channels have a higher voltage on the low-pressure side and a lower voltage on the high-pressure side.

The concept behind the device is relatively straight-forward, but the physical reality is complex. The diagrams presented here are simplified, having perfectly flat walls containing single atom ions carrying a single charge. No mention of molecules has been made, which increases the complexity. Polar molecules such as water have positive and negative components offset in space. Although simplified, this material illustrates the how streaming cells work. Next, literature concerning the operation, design and improvements to streaming cell technology is presented and discussed.

2.2.1 Literature Review

In 1964, a paper by Osterle gave an analysis of energy conversion from streaming cells, both for the purpose of pumping fluid or generating electrical power was presented [40]. The cell he used consisted of fine capillary tubes stacked together to form a streaming cell. A diagram of that cell, in its pumping configuration, is reproduced here as fig. 2.11. Importantly, he shows that a streaming cell has the same conversion efficiency whether it is

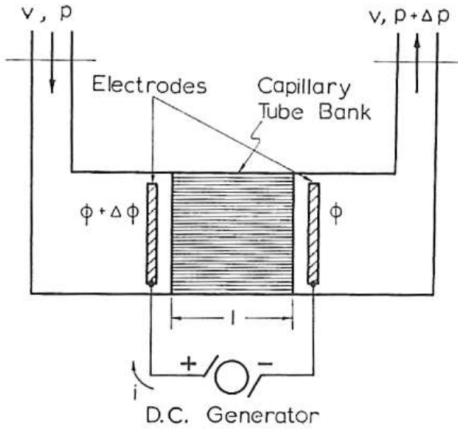


Figure 2.11: Osterle's electrokinetic pumping cell, reproduced from [40]

in a pumping mode, where electrical energy is supplied, or in a generating mode, where electrical energy is produced. Based on his analysis, Osterle gives an illustrative example of a streaming cell producing electrical energy. He states that tube bank having a volume of 100 cm^3 with 100 kPa of hydrostatic pressure applied would be capable of producing 0.49 W of electrical energy. This would require 125 W of pumping power to achieve, giving an energy conversion efficiency of 0.392% .

Within the space of a year three papers related to properties of fluid flow in fine capillaries, such as those used by Osterle are presented. Burgreen and Nakache investigate both the flow when the capillaries are rectangular [7], and the efficiency of such capillaries when used to generate electrical power or to pump [8]. Their work develops mathematics behind rectangular streaming cells and shows fine glass capillaries are equally efficient when used to generate electrical power or to induce liquid pumping. Rice and Witehead make an analysis of fluid flow profiles that consider the effect of double layer interactions [44]. They show how the double layer affects the level to which liquid can permeate a material populated with cavites.

Together these three papers mark the beginning of research into streaming cells.

There appears to be little published research into streaming cells until 2003, when a surge of papers related to optimal dimensions of streaming cells appear. An analysis relating energy conversion efficiency to the length of a streaming cell channel indicated that short cells are the most efficient [59]. However, more recent work by Chang and Yang shows a decrease in conversion efficiency at maximum power when the channel length is low [9]. This work suggests there is an optimum channel length, which is also dependent on the fluid conductivity. Investigation into the relationship between the Debye length of the double layer and streaming cell conversion efficiency found that a channel is most efficient when its height is twice that of the Debye length [13] This corresponds to the point at which double layers formed within a cell begin to overlap with one another.

In 2005 a seminal paper by van der Heyden et al. reported on streaming cell measurements made in a single micro-channel 70 μm in height [51]. Many valuable contributions were detailed in this paper, namely:

1. Confirmed that reversing the polarity of surface potential reverses the direction of the streaming current.
2. Found that the maximum conversion efficiency corresponded to channels where double layers begin to overlap. This confirms the relationship put forward the previous year by Daiguji et al.
3. Showed that boundary conditions involving constant surface potentials, used up to this point to model streaming, are inaccurate.
4. Predicted a maximum energy conversion efficiency of $\sim 6\%$ for potassium chloride solutions of 1×10^{-5} mol in silica channels of height

145 nm.

Subsequent research by the same authors show that conversion efficiency is maximised at low salt concentrations [52]. They also predict an energy conversion efficiency of 12 % for streaming cells using electrolyte solutions containing lithium. Around the same time, Daiguji et al. publish work suggesting that in order to increase cell efficiency one may either reduce the channel height or decrease the ionic concentration of the working fluid [12]. This supports the work of van der Heyden et al. with respect to efficiency gains with the working fluids having low ionic concentrations.

In 2007, van der Heyden et al. publish a measured energy conversion of 3.2 % [53]. They suggest that the conversion efficiency of a channel is limited by a property termed ‘Stern conductance’. The concept of Stern conductance is that the Stern layer (see fig. 2.7) itself provides a pathway for electrical conduction. This conduction turns the surface of the glass into an electrically conductive surface causing the cell to partially self-discharge. Stern conductance is often referred simply as ‘surface conductance’. Davidson and Xuan published a mathematical model shortly after confirming the role of Stern conductance on streaming cells, in particular those with low ionic strength [14]. They suggest that this is the reason for poor measured efficiencies in light of the much higher predicted values.

Most recently, the concept of hydrodynamic slip has been applied to streaming cells as a way of increasing conversion efficiency. Estimates using mathematical models predicted conversion efficiencies between 30 % and 70 % [15, 41, 43]. Hydrodynamic slip refers to the ability of a fluid to ‘slip’ relative to a boundary/interface. Slip is advantageous to streaming cells because it permits ions in the Stern layer to move relative to the wall. The length refers to an imaginary distance into the solid wall where the

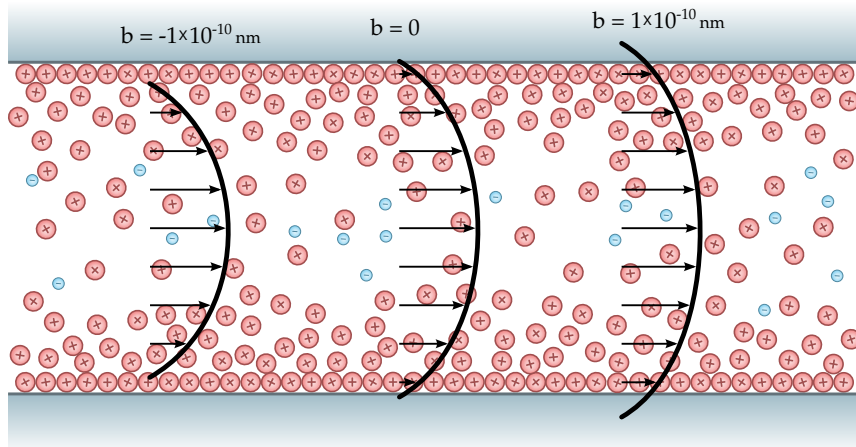


Figure 2.12: Illustration of hydrodynamic slip inside a channel cavity, where b is the slip length. Arrows indicate flow velocity in each of the three situations.

traditional ‘no-slip’ boundary condition would occur (refer to fig. 2.12). A ‘no-slip’ boundary condition dictates that fluid at the boundary of a solid must have zero velocity. This condition, along with viscosity, is responsible for the parabolic flow profile a fluid takes as it moves through pipes. An issue surrounding slip was illustrated by Eijkel who showed that a channel’s zeta potential and its slip length are linked [16]. The general problem with slip-based mechanisms is that a high zeta potential is optimal for double layer formation, however it also promotes wetting. Wetting and hydrodynamic slip are related to each other by the strength of attraction between a liquid and a solid. To explain, the terms hydrophobic and hydrophilic are used to describe surfaces that repel and attract water. A hydrophobic surface has a low tendency to support water, i.e., water will bead and roll off a hydrophobic surface. Conversely, a hydrophilic surface is one that water is attracted to, causing a droplet to spread and stick to the surface. Hydrodynamic slip occurs when a channel’s walls are hydrophobic, allowing water at the interface to slip along the boundary of the solid. High zeta potentials attract water to the solids surface due to electrostatic attraction. Eijkel’s

publication illustrates that the zeta potential and hydrodynamic slip are related to one another. In order to improve the situation in steaming cells a surface should be both non-wetting and hold a high surface charge. Conservative estimates place an efficiency of 40 % on cells having slip lengths tens of nanometres long, obtainable using carbon nanotubes, using solutions having low salt concentration.

Theoretical predictions of the efficiency of standard micro/nano-fluidic channels are 2% for pure water and 7% for sodium chloride. [52] However, measured conversion efficiencies as reported thus far are:

- “far less than 1 %” forcing potassium chloride through a porous glass plug having pores in the range 1 – 1.6 μm [39].
- 0.01% by forcing water through porous glass with pore sizes from 10 – 16 μm . [59]
- 0.8% by forcing pure water through a ceramic rod populated with 6 μm pores. [60]
- 3% by forcing a sodium chloride solution through a 75 nm by 50 μm silica channel. [53]
- 0.77% by forcing a sodium chloride solution through a 200 nm pore in an alumina membrane. [30]
- 5% by forcing a sodium chloride solution through a 0.5 nm cylindrical pore in polyethylene terephthalate foil. [57]

It is clear from the literature that there is significant progress to be made with respect to increasing the conversion efficiency of streaming cells. Techniques to induce hydrodynamic slip at the fluid-solid interface are predicted to increase this efficiency to 30-40% [15,43], but progress in this area is dictated

by advancements in materials science. Experimental results utilising slip enhanced channels have not yet been reported in the literature. Surface enhanced channels will not be investigated due to manufacturing difficulty, cost, and the level of scientific development required to make progress.

In summary, the finding that maximum conversion efficiency occurs at low ionic concentration supports the use of tap-water as a working fluid. Using glass as a substrate seems to be a suitable choice, which is both cost effective and easy to source. The dimensions of channels found in the literature suggest that fabricating trial cells is feasible with the equipment available. A conversion efficiency of 0.01 % should be achievable using a porous glass plug. This efficiency will be used a baseline to compare measured efficiency from fabricated cells.

2.3 Impedance Modelling

Electronic components have well defined electrical impedances. This provides a way to calculate the voltage over a component as a function of time by knowing the current through it, or vice versa. For linear devices, such as capacitors, inductors and resistors, this is a relatively simple matter of knowing the size of the device. For non-linear devices, such as diodes and transistors, there are models that describe the impedance relationship, which are based on the properties of the materials they are made from. But what does an electronic engineer do when there is an electrode-electrolyte-electrode system in their circuit? There is no standard model for this situation and trying to calculate the impedance is not trivial.

Circuit simulators rely on knowing the impedance of components in order to calculate the currents and voltages in circuit branches. SPICE is a commonly used circuit simulator that has models of transistors and diodes

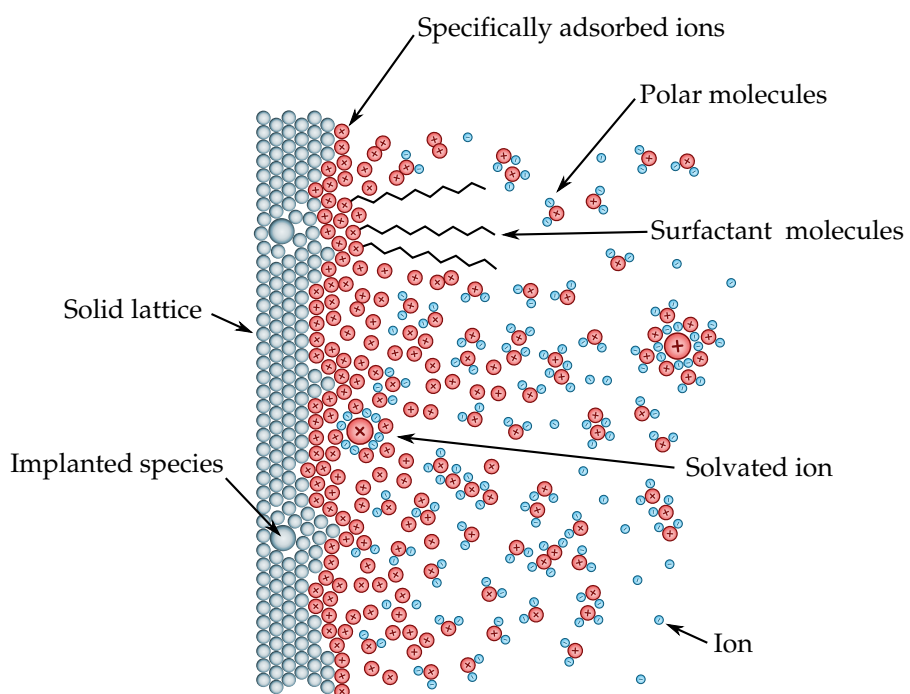


Figure 2.13: Diagram of an liquid-solid interface showing various types of molecule configurations, surface imperfections and polar molecules. This diagram is based on the work of Bard et al. [3]



Figure 2.14: Drawing of an eight electrode array used for spinal stimulation. The electrode is called an Octrode and is made by St. Jude Medical.

built in. It can easily simulate complex circuits quickly and is a valuable tool for circuit designers as a means of testing their designs before construction. However, if the software does not have a model of a component, and the user is not able to describe it, then a circuit simulator is of little use. Part II of this thesis uses a model of an electrode/electrolyte interface to solve some of these problems. That interface model can be entered into circuit simulators because it is built of standard components. This means that an electronic engineer can enter it into their design and know what sort of electrical loading to expect between a pair of electrodes in an electrolyte bath.

In section 2.1, illustrations of double layers were presented showing that the interface is comprised of layers. A more realistic illustration of a solid-liquid layer is shown in fig. 2.13. It shows interactions between polar molecules, between polar molecules and ions, surfactants at the interface, an imperfect solid/liquid boundary, and the Stern layer. The complexity of interactions that happen at the interface are what make it so difficult to model. Additional to the interface's impedance is the geometry of the electrodes and the properties of the electrolyte. These factors make calculating the impedance between electrodes of an electrode-electrolyte system complex.

To the designers of medical implant devices, estimating the impedance of electrodes in an electrolyte is critical for safe stimulator design. Saluda Med-

ical is a recently started company based in Sydney, Australia, developing implantable spinal stimulators. Their engineers have designed a stimulator fit for human implantation, but are unsure of the electrical impedance that their implant will see once implanted. Getting it wrong could mean their microchip may ‘latch up’. This occurs when one or more pins on a chip goes higher than the supply voltage. When this happens, those pins that went above the supply voltage will get stuck on and the only way to turn them off again is to power down the entire chip. In an implanted setting this is potentially lethal. Naturally, Saluda want a way to model the impedance of electrodes implanted into a human spinal cavity. This involves modelling the electrode/electrolyte interface itself, a central idea in interface science. Part II of this thesis looks at ways of doing that using a model of the interface itself. Such a model is suitable for entry into common circuit simulators, such as SPICE, that electronic engineers already use.

Part I

Double Layers on Insulators: Harvesting Energy

In section 2.1, the topic of interfacial double layers were introduced. Then, in section 2.2, a way of utilising double layers to harvest energy - in a process called streaming - was studied. The possibility of using streaming cells as a means of powering electronic water meters is now put to the test. Chapter 3 studies streaming cells, where some test cells are made and measured. With an understanding of readily available streaming cell performance, their applicability for use in water metering is discussed in chapter 4. This presents an estimation of water use in a typical New Zealand home which is used to determine the amount of energy available to a harvester. Chapter 5 measures the energy consumption of low-power, 8-bit microcontrollers and wireless transmitters. The measured data is used to estimate the energy requirements of an electronic water meter with wireless transmitter. Finally, in chapter 6, the feasibility of using streaming cells as energy harvesters for our intended application is discussed and the conclusion is made.

Chapter 3

Streaming Cell Energy Harvesting

This chapter begins with a mathematical analysis of streaming cells and their operating parameters. Following this, in section 3.2, a number of different streaming cells are built. Some of the earlier, failed attempts, at making streaming cells are shown followed by a more successful streaming cell design. Ten streaming cells are made using this design, each having different internal dimensions. The electrical output and energy conversion efficiency of these cells is measured in section 3.3. Measurement results are discussed in section 3.5, followed by concluding remarks on the material presented in this chapter.

3.1 General Analysis

A basic model of operation for a streaming cell is established. This determines what parameters are important when maximising a cell's output power.

3.1.1 Mathematics

Mathematical analysis of streaming cells provides a basic understanding of the parameters involved with their output and geometry. Rigorous

mathematical analysis of streaming cell performance is extremely involved and is well detailed in the literature [58]. As aspects of a double layer's structure are still not fully understood, the mathematics behind them is still being developed. Computer simulation and mathematical models continue to shed light on ionic organisation at liquid-solid interfaces [28]. For that reason, I have not attempted to model a streaming cell physically. Instead, I piece together a relatively simple mathematical model quantifying important operating parameters.

Streaming voltage

Gu and Li derived the following equation relating the streaming voltage to the pressure applied across a streaming cell [61].

$$\frac{V_s}{\Delta P} = \frac{\epsilon_r \epsilon_0 \zeta}{\mu(\sigma + \frac{2}{\delta} \lambda)} \quad (3.1)$$

where:

V_s is streaming voltage

ΔP_z is pressure differential (across the channel)

ϵ_r is the relative permittivity of the liquid

ϵ_0 is the absolute permittivity of free space

ζ is zeta potential

μ is the fluid's viscosity

σ is the fluid's bulk conductivity

δ is the channel's height

λ is the channel's surface conductivity

This equation is specific to parallel plate channels, of the type constructed in the following section. It requires that the width to height ratio of the channel is greater than 20, which it is for the cells constructed here. Gu and Li use this equation as a means of finding the zeta potential and surface conductance by rearranging it into the following form:

$$\frac{\varepsilon_r \varepsilon_0 \Delta P}{\mu V_s \sigma} = \frac{1}{\zeta} + \left(\frac{2 \lambda}{\zeta \sigma} \right) \frac{1}{\delta} \quad (3.2)$$

Later, the streaming voltage of ten cells with the same dimensions of those used by Gu and Li will be measured. The left hand side of this equation will be plotted against the inverse of channel height to see if their results can be replicated. If successful, this will give a way of determining the zeta potential and surface conductance of the fabricated cells.

Streaming current

Gu and Li, also also derive a similar equation for streaming current [61]. This equation, shown below, has been slightly rearranged to match the form of 3.1

$$\frac{I_s}{\Delta P} = \frac{\varepsilon_r \varepsilon_0 \zeta W \delta}{\mu L} \quad (3.3)$$

where

W is the width of the channel

L is the length of the channel

This equation is similar to that given by Olthuis et al. for a porous plug, but has been derived specifically for rectangular channels [39].

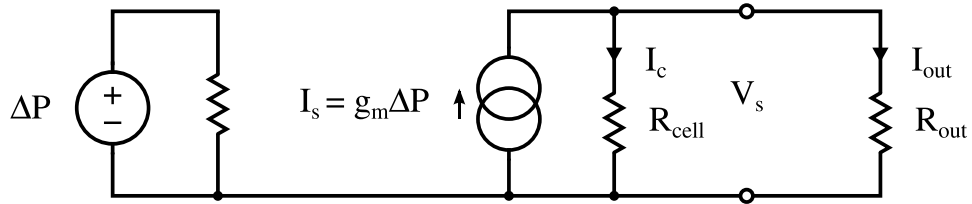


Figure 3.1: Schematic representation, commonly used in electronics, of a streaming cell with attached output resistance

3.1.2 Electrical model

Figure 3.1 depicts schematically how a streaming cell operates when connected to an external load. A model of this sort is commonly used to analyse the behaviour transistors. This particular model is based on the work of Olthuis et al. in [39], but has been modified slightly. Instead of showing ζ as the equivalent voltage source, it is shown here instead with the pressure applied (ΔP). This change was made because there is no way of controlling the zeta potential - it determined by the properties of the particular interface. However, the amount of pressure developed across the cell is controllable, and from eq. (3.3) it is shown to be directly proportional to streaming current. In fact, the transconductance (g_m) for this model is eq. (3.3). The model aids analysis in that it shows the electrical configuration of an external load resistance (R_{out}). As shown, any load resistance placed across the cell is being placed in parallel with the internal electrical resistance of the cell. This will help to determine how best to optimise the cell in order to maximise its electrical output.

3.1.3 Optimisation

Having a mathematical model of a streaming cell allows for optimisation of its operating parameters. The model shows that any load placed across a streaming cell is actually placed in parallel with that cell's internal resistance.

Therefore, choosing a suitable load is an important design consideration. It is possible to optimise the cell's output for maximum power output, or maximum efficiency. So which is best suited to harvesting applications?

Streaming cells are not batteries. The only time energy can be extracted from a streaming cell is when pressure developed across it. This only happens because of liquid flowing through it. When harvestable power is available, we need to collect as much of it as possible – *no matter how much is wasted*. Because a cell is incapable of storing energy, any energy that we could not capture will be lost.

The story is different for battery applications. In those situations it may, but not necessarily, be advantageous to optimise for maximum efficiency. Doing so will conserve the energy in a battery and ensure that as little as possible goes to waste. This might be something a cell phone designer aims to achieve, but less important for batteries accelerating an electric car.

In situations requiring maximum efficiency, the efficiency of the system approaches 100 % as the power delivered approaches 0 %. In situations requiring maximum power, the maximum achievable efficiency is 50 %. This means we can only harness half of the electrical power developed by a cell, at best.

Optimising R_{out} for maximum power

Using Ohm's Law it is possible to form an equation linking the total power (P_{cell}) to the total electrical resistance across the cell (R_{tot}).

$$\begin{aligned} P &= V \times I \\ V &= I \times R \\ P &= I^2 \times R \\ P_{cell} &= I_s^2 \times R_{tot} \end{aligned} \tag{3.4}$$

Where I_s is the streaming current created by pumping ions through the channel. As the output resistance and internal cell resistance are in parallel we can find the output current (I_{out}) by treating the cell as a resistor divider (as is shown in fig. 3.1). Using a resistor divider equation for current in parallel branches yields:

$$I_{out} = I_s \times \frac{R_{cell}}{R_{cell} + R_{out}} \tag{3.5}$$

Combining (3.4) and (3.5) we can extract the power dissipated in a load attached across the cell.

$$\begin{aligned} I_{out} &= I_s \times \frac{R_{cell}}{R_{cell} + R_{out}} \\ P_{out} &= \left[I_s \times \frac{R_{cell}}{R_{cell} + R_{out}} \right]^2 \times R_{out} \end{aligned} \tag{3.6}$$

Equation (3.6) takes into account the internal dissipation within the cell due to its own internal resistance. In order to optimise the output power it is necessary to find the value of output resistance (R_{out}) that maximises the output power.

A parallel resistance system where we try to maximise the output power suggests this is a maximum power transfer theorem problem. The maximum power transfer theorem states that in order to maximise the power delivered to an external load from a source which itself has an internal resistance, one must make the two resistance equal.

Optimising streaming cell parameters

We now use the optimised values of R_{out} and R_{cell} to calculate the maximum available power. This is done by substituting R_{out} and R_{cell} for simply R in (3.6) as follows.

$$\begin{aligned} P_{out} &= \left[I_s \times \frac{R_{cell}}{R_{cell} + R_{out}} \right]^2 \times R_{out} \\ P_{max} &= \left[I_s \times \frac{1}{2} \right]^2 \times R \\ P_{max} &= \frac{I_s^2 R}{2} \end{aligned} \quad (3.7)$$

As $P = I^2 R$ (via the power equation and Ohm's Law) this indicates at best we can capture half of the available power.

It is now possible to combine the equation for maximum power, (3.7), and that for streaming current, (3.3).

$$\begin{aligned} P_{max} &= \frac{I_s^2 R}{2} \\ P_{max} &= \left(\frac{\varepsilon \zeta W \delta \Delta P}{\mu L} \right)^2 \times \frac{R}{2} \end{aligned} \quad (3.8)$$

where $\varepsilon = \varepsilon_0 \varepsilon_r$ and $R = R_{cell} = R_{out}$.

To get a better feel for this equation, it may help to substitute in the parameters that affect R . From here we will refer to R as the internal electrical resistance of the cell. It also refers to the external resistance in the maximum

power condition, but we are free to vary that to match the internal resistance.

We begin with the understanding that:

$$R \propto \frac{L}{A\sigma} \quad (3.9)$$

$$R_h \propto \frac{L\mu}{A} \quad (3.10)$$

where σ is the conductivity of the liquid and A is the cross-sectional area of the cell. The first equation (3.9) states that the electrical resistance will increase with cell length and decrease with the cross-sectional area of the cell and the conductivity of the fluid. The second (3.10) states that the fluid mechanical resistance will increase with the length of the cell and the viscosity of the fluid, and decrease with the cross-sectional area of the cell.

We can identify an inverse relationship with hydrostatic resistance in We can identify the presence of R_h in equation (3.8). Starting with this equation we substitute equation (3.9) in and rearrange to produce an approximate relationship between pressure, cell length and area:

$$\begin{aligned} P_{max} &= \left(\frac{\varepsilon \zeta W \delta \Delta P}{\mu L} \right)^2 \times \frac{R}{2} \\ P_{max} &\propto \left(\frac{W \delta}{\mu L} \right)^2 \times (\varepsilon \zeta \Delta P)^2 \times \frac{L}{A \sigma} \times \frac{1}{2} \\ P_{max} &\propto \left(\frac{A}{\mu L} \right)^2 \times (\varepsilon \zeta \Delta P)^2 \times \frac{L}{A \sigma} \times \frac{1}{2} \\ P_{max} &\propto \frac{A^2}{L^2} \times \left(\frac{\varepsilon \zeta \Delta P}{\mu} \right)^2 \times \frac{L}{A} \times \frac{1}{2\sigma} \\ P_{max} &\propto \frac{A}{L} \times \left(\frac{\varepsilon \zeta \Delta P}{\mu} \right)^2 \times \frac{1}{2\sigma} \\ P_{max} &\propto \left(\frac{\varepsilon \zeta \Delta P}{\mu} \right)^2 \times \frac{A}{2L\sigma} \\ P_{max} &\propto \frac{\Delta P^2 A}{L} \times \frac{\varepsilon^2 \zeta^2}{2\mu^2 \sigma} \end{aligned} \quad (3.11)$$

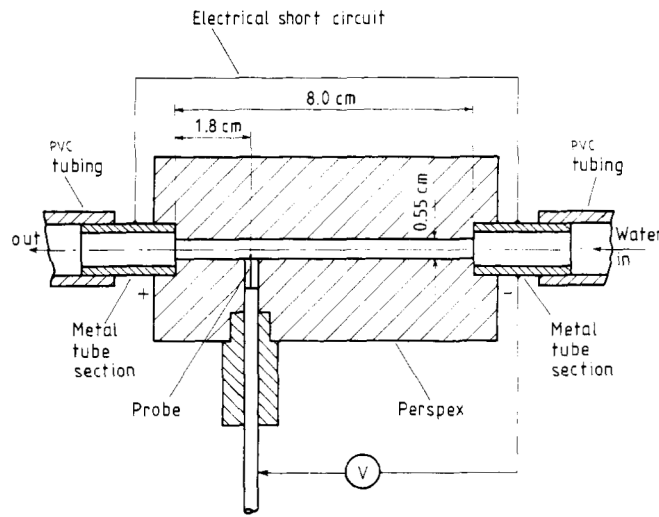


Figure 3.2: Diagram of a cavitation device, taken from [54], reported to be able to generate over 50 V across its ends by pumping water through it.

This equation (3.11) suggests that a cell with a small length, large area and high pressure is the best candidate for maximising power output. When using tap water we have no control over the remaining parameters; highlighting the importance of cell geometry and applied pressure.

3.2 Building a Streaming Cell

Building a streaming cell seemed a simple task at the outset. This section gives a brief overview of the work related to creating that first working streaming cell.

3.2.1 First streaming cells

The work that first sparked the interest of both my primary supervisor and I in streaming devices was that of Varga and Seymour [54]. In that paper it was reported that a device employing cavitation as a means of increasing the resistance between two bodies of water was capable of developing over 50 V



Figure 3.3: Photo of the first generation of streaming device built, by summer research student Jonathon McMullan, to create the streaming voltages reported by Varga and Seymour.

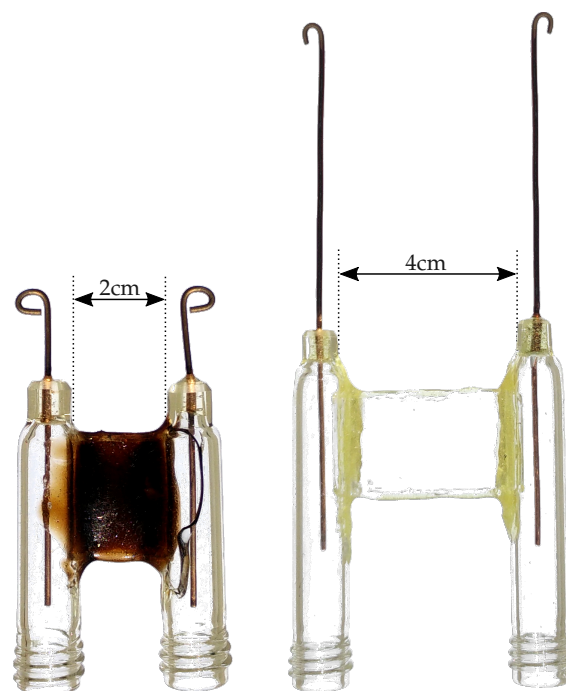


Figure 3.4: Photo showing two examples of a second design of streaming cell made entirely from glass.

across its ends. A diagram of the cavitation device is shown as fig. 3.2. An attempt to replicate the results of that paper was made by summer research student Jonathon McMullan. Jonathon built a replica of the device, shown as fig. 3.3; but was unable to reproduce streaming phenomena.

My supervisor and I became skeptical of streaming cells at this point and looked elsewhere for energy harvesting ideas. The following year, summer research student Wane Crump and I conducted experiments to determine the amount of charge that could be transported on water droplets. This work was related to the idea of an electrostatic generator. See appendix A for details of the droplet based harvesting research.

Later, other designs of streaming cells, namely those of Gu and Li [61], were found. Their design of streaming cell looked simple and easy to fabricate, so attempts were made to replicate them.

Employing Waikato University's glassblower, Steve Newcombe, two streaming cells were fabricated entirely from soda-lime glass. These streaming cells are shown in fig. 3.4. Each of the two channels were made by placing a $50\text{ }\mu\text{m}$ sheet of copper between the glass slides; then welding the glass slides together to seal the cell; and finally, etching the copper out with acid. The cells were then welded (with glass) to the two side tubes that held the copper electrodes. By varying the length of the two channels (one of 2 cm, the other 4 cm) we hoped to determine what role length played on channel output characteristics.

Both of the cells burst under the water pressure applied from lab taps. A crack along the right hand reservoir is visible on the 2 cm wide channel. Attempts were made to strengthen the channels by coating joins with industrial glues, but none were successful.

Item	Brand	Product details
Microscope slides	Sail Brand	JIA 7101WT - 26 x 76mm
Shims	Garlock	Colorplast - 50 μm , 80 μm , 120 μm and 250 μm
Epoxy	Selleys	Araldite - Ultra Clear Resin
Pressure sensor	Honeywell	24PC15SMT - 0 – ± 15 PSI

Table 3.1: Table of materials used to construct the streaming potential cells

3.2.2 Robust streaming cells

The two previous attempts to create streaming cells had failed. In the moments before failure, the all-glass streaming cells developed measurable voltage across their terminals. I knew I was close, but the all-glass design needed revising. A new design was found that solved the problem of cracking. It favoured the used of epoxy resin and acrylic to contain the channels, allowing for more flex without the risk of cracking. Aspects of the design were taken from a paper by Gu and Li [61].

Construction

Construction begins by sectioning standard microscope slides into halves. This gives glass panels of approximately 26 mm \times 38 mm \times 1 mm. A single panel is then epoxied to an acrylic base plate, as is shown in Figure 3.5. Once set, plastic shims are cut to the required size, covered with a very thin layer of epoxy, and placed along the edges of the slide. The shims line the sides of the glass panel such that they leave a 1 cm gap through the centre. A second glass slide is then placed on top of the shims and epoxy resin is used to seal the sides. Pressure was applied to the stack while the epoxy set to ensure the epoxy was distributed correctly and to control the channel height. A photo of the shims glued between the two slide halves is shown in Figure 3.6. Once set, each channel is examined under a microscope to determine the internal channel height. Each of the four corners were

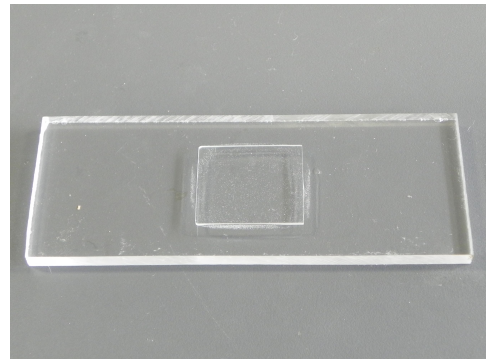


Figure 3.5: Photo showing half of a glass slide glued to acrylic base plate

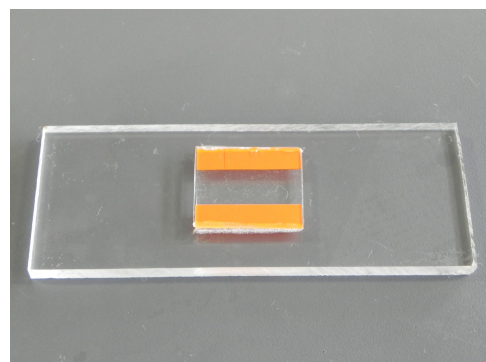


Figure 3.6: Photo showing plastic shims sandwiched between two slide halves

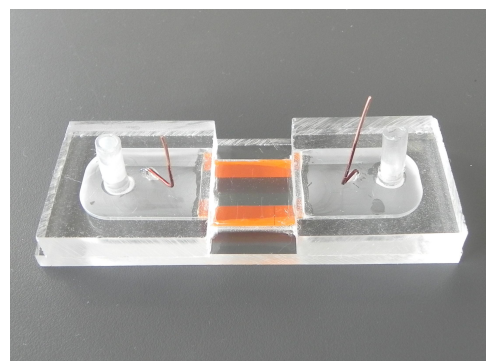


Figure 3.7: Photo showing final assembly

measured to ensure the internal dimensions remained rectangular once set. To finish, acrylic reservoirs were mounted over each end of the channel. These reservoirs facilitate the connection of fluid tubes and voltage probes to each end of the channel. The final assembly is shown in Figure 3.7. A full list of materials used to construct the channels is presented as Table 3.1. A total of ten channels were made and tested using this method.

3.3 Measurements

Of the papers describing experiments using streaming potential cells ([31, 46, 52, 61]), I chose that of Gu and Li to replicate [61]. This was because, at the time, it was the only paper I was aware of. Their method employs a simple cell design, discussed in the previous section, and a detailed description of the experimental procedure. This section details the fabrication and measurement of a number of streaming cells.

3.3.1 Experimental setup

Measurement of the harvester's output was made in a laboratory with high-sensitivity measurement apparatus and a lab tap for the application water pressure. The cells output power was measured with a precision source measurement unit (SMU) and applied pressure was monitored with a differential pressure sensor.

The Agilent E5270B is a mainframe system that holds banks of SMUs with connections to a GPIB computer interface. The Department of Engineering's E5270 contains three SMUs, each having the ability to measure currents as low as one femto-ampere. The device uses separate 'force' and 'sense' connections to ensure the voltage/current being set is accurately controlled where they meet. Additionally, it uses tri-axial cables to minimise

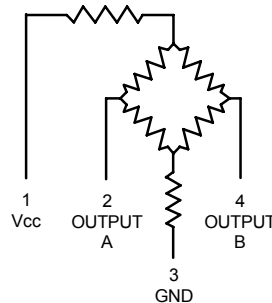


Figure 3.8: Circuit diagram of the differential pressure sensor bridge circuit (taken from [23])

any interference from outside sources; important when measuring such low currents.

The input resistance to the E5270's measurement units are specified as $13\text{ G}\Omega$. It is essential to use such a high impedance measurement due to the high internal resistance of the cell. I later show that the internal electrical resistance of the cell is in the order of $5\text{ M}\Omega$, so the E5270's input impedance is roughly two thousand times larger. If using a lab multimeter, typical internal resistance of $10\text{ M}\Omega$, its internal resistance is too close to that of the cells and will affect the measured output.

The pressure sensor used was a Honeywell 26PC SMT Series differential pressure sensor. It comes as surface mount package, making it a cost effective solution, but delicate to set up. On its exterior are two ports to which rubber tubes are attached. Between those ports, internal to the sensor, sits a diaphragm. That diaphragm controls the resistance between two nodes in the sensor's bridge circuit (shown in figure 3.8). By applying 10 V DC between the 'Vcc' and 'GND' pins, the output voltage between outputs 'A' and 'B' correspond to the applied pressure. Measurement of that output voltage was done using the precision measurement mainframe.

The mainframe was controlled from a PC running Python scripts utilising the open source Python-vxi11 library [42]. This allows sweeping the

CELL - A	Voltage/current at high-pressure side of cell
PRESS. - A	Output A of pressure sensor
PRESS. - B	Output B of pressure sensor
CELL - B	Voltage/current at low-pressure side of cell

Table 3.2: Description of labels used in the streaming cell measurement setup diagram

amount of current drawn from the harvester while recording the corresponding voltage drop. This is the equivalent of varying the load resistance, which allows us to find the point of maximum power transfer.

Figure 3.9 shows the measurement setup as a diagram. It shows connection of the measurement mainframe, bench-top power supply, streaming cell, pressure sensor, and the lab tap. Table 3.2 provides details of the abbreviated electrical connection labels used in the figure 3.9.

3.3.2 Measurement issues

There are two issues with the measurement setup that may impact the measurements. Firstly, the electrodes used were copper and are susceptible to polarisation by electrolysis. Secondly, the differential pressure sensor is only rated to 15 PSI (approximately 100 kPa), less than half the maximum pressure developed across the cell.

Electrolysis on at the electrode surface causes the electrodes to polarise. This results in a semi-permanent offset voltage appearing between the electrodes. That offset voltage is opposite in polarity to what is developed while cell is in operation. By reversing the flow of water through the cell, the polarisation can be reversed. Use of more suitable electrode materials would reduce this effect, for instance platinum black electrodes. Copper was used for the electrodes as it was cheap, easily obtainable, and easy to work with.

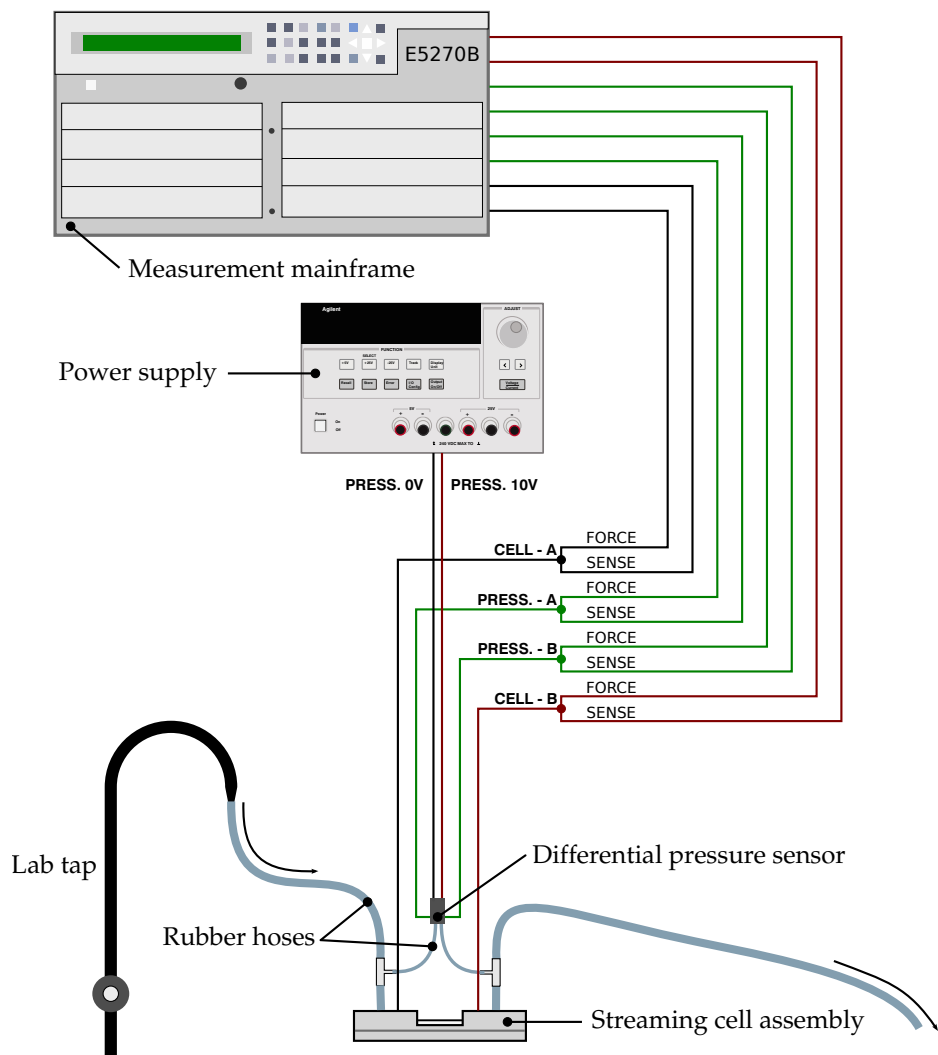


Figure 3.9: Diagram of equipment setup while measuring power output from the streaming cell harvesters

From measurement of the output *voltage* of the cells, the presented graphs and figures have been adjusted to remove the effects of electrolysis. This was done by adding an offset to the measured data to shift the y-intercept up to 0 V. This provides a more accurate representation of the situation had platinum black electrodes been used. As no absolute data is taken from these measurements, the y-intercept adjustment does not affect any subsequent predictions made about the cells. Only the gradient of the output, relative to the pressure applied is used; and even then, only to select a suitable candidate cell for power measurement. *Most importantly*, no offsets have been applied to measurements of the cell power output.

Although the maximum rated pressure of sensor was 15 PSI (approximately 100 kPa), the sensor's output remained linear up to our maximum pressure of 40 PSI (275 kPa). I expect that exceeding the sensors specified pressure will result in a lower 'mean time to failure', but its output remained true. As a precaution, a tyre pressure gauge was used to roughly confirm the output of the sensor at the end of the cell measurements. This was a crude test, however it's output matched that of the differential pressure sensor, so was taken as a good indication of its accuracy.

3.4 Results

Results from streaming cell measurement are broken into two sub-sections. The first presents the output voltage of the ten cells in response to applied water pressure. From these measurements, the cell with the highest voltage/pressure ratio is found. The second sub-section shows the maximum power that can be harvested from that cell. These are the most important measurements as they reveal the energy conversion efficiency of the cells.

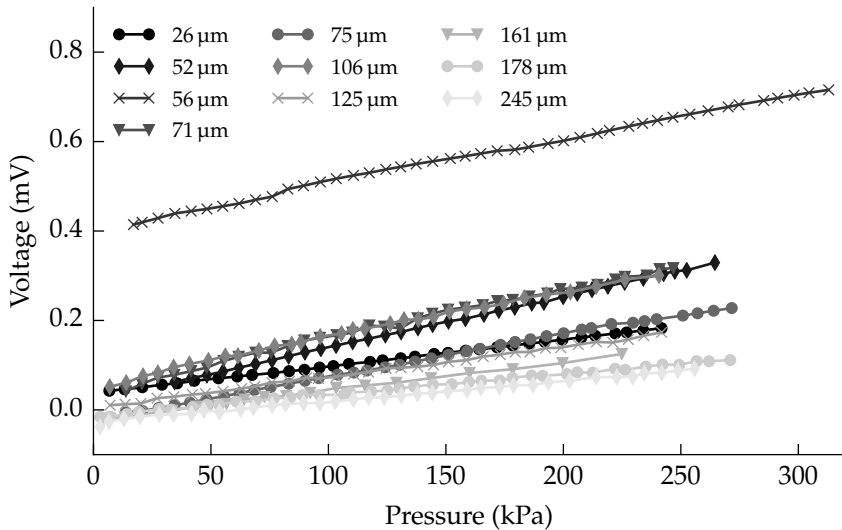


Figure 3.10: Plot showing un-adjusted streaming voltages versus applied pressure.

3.4.1 Streaming voltage versus pressure

Figures B.1 to B.10 show adjusted results of streaming voltage measurements from each of the ten cells. They represent the first successful measurements I had made of streaming cells. During these measurements three cells burst under pressure; two were dropped and subsequently shattered; and one suffered epoxy failure, loosing its acrylic base plate.

No measurements of flow rate or output current were made during these early experiments. As a result they reveal very little about the efficiency of the cells themselves. We cannot determine either the mechanical energy put into the cells, nor the output power available. However, we can relate these measurements to those made by Gu and Li; as will be shown and discussed shortly.

Figure B.3 required an offset adjustment of 405 mV before its slope gave a 0 mV intercept. This indicates that the electrodes were highly polarised by the time the measurements were made. This effect is especially evident in

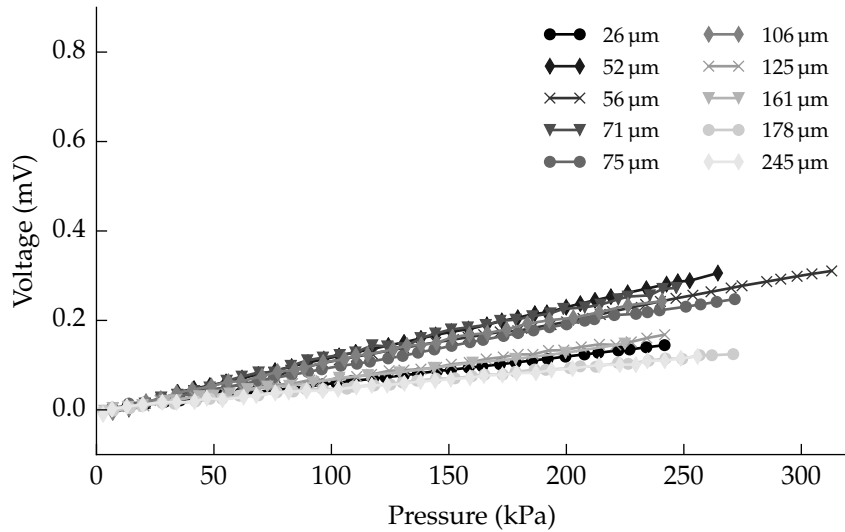


Figure 3.11: Plot showing adjusted streaming voltages versus applied pressure.

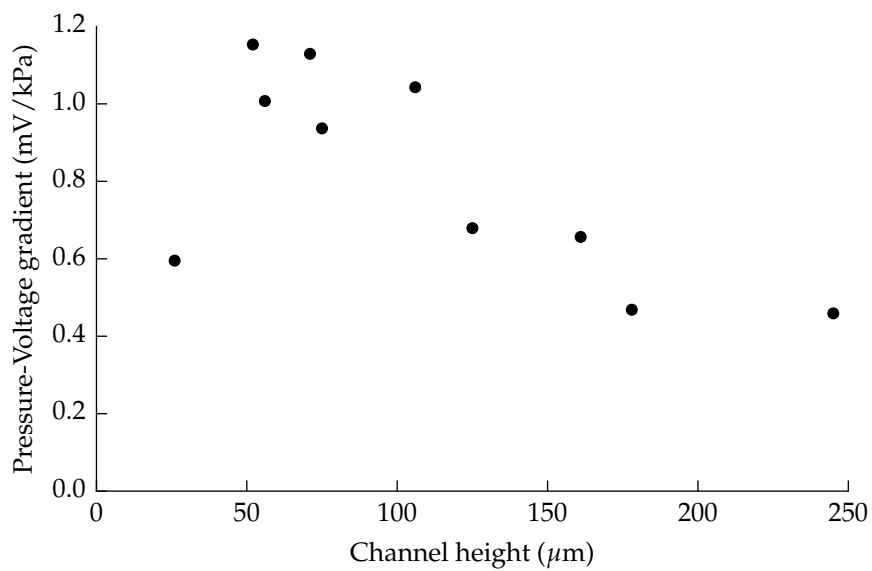


Figure 3.12: Scatter plot of voltage/pressure gradient versus channel height for each of the measured channels.

fig. 3.10, where each of the traces have been placed on a single graph.

Some of the traces exhibit a certain amount of ‘jitter’ in their pressure-to-voltage gradients. This is likely due to the time difference between adjacent measurement points. Measurement points were not taken monotonically, instead being extracted from a number of pressure cycles.

The effect of adding the offset adjustments is visible in fig. 3.11. These adjustments bring all of the slopes together so the origin sits at 0 V Pa^{-1} .

Figure 3.12 shows the streaming voltage to pressure gradients versus channel height. This data has been taken from the previous graph (fig. 3.11)) to show the response as a function of channel height.

3.4.2 Output power versus load resistance

Figure 3.13 shows the characteristic power curve of a the $71 \mu\text{m}$ high streaming cell channel. Pressure fluctuations near the end of the experiment are due to usage of the departments water system. Their effect is visible in both the streaming voltage and output power traces, highlighting the strong coupling to applied pressure.

The maximum power delivered by the cell was 1.52 nW , corresponding to a current draw of 33.5 nA with a streaming voltage of 182 mV . Generating this power required 260 kPa of pressure, resulting in a flow rate of 2.05 ml s^{-1} . This equates to 539 mW of pumping power lost to the device and therefore an energy conversion efficiency of $0.28 \mu\%$.

3.5 Discussion

Initial measurements of streaming voltage revealed that the output voltage is directly proportional to applied pressure. Containing pressures reaching 260 kPa within glass structures is difficult.

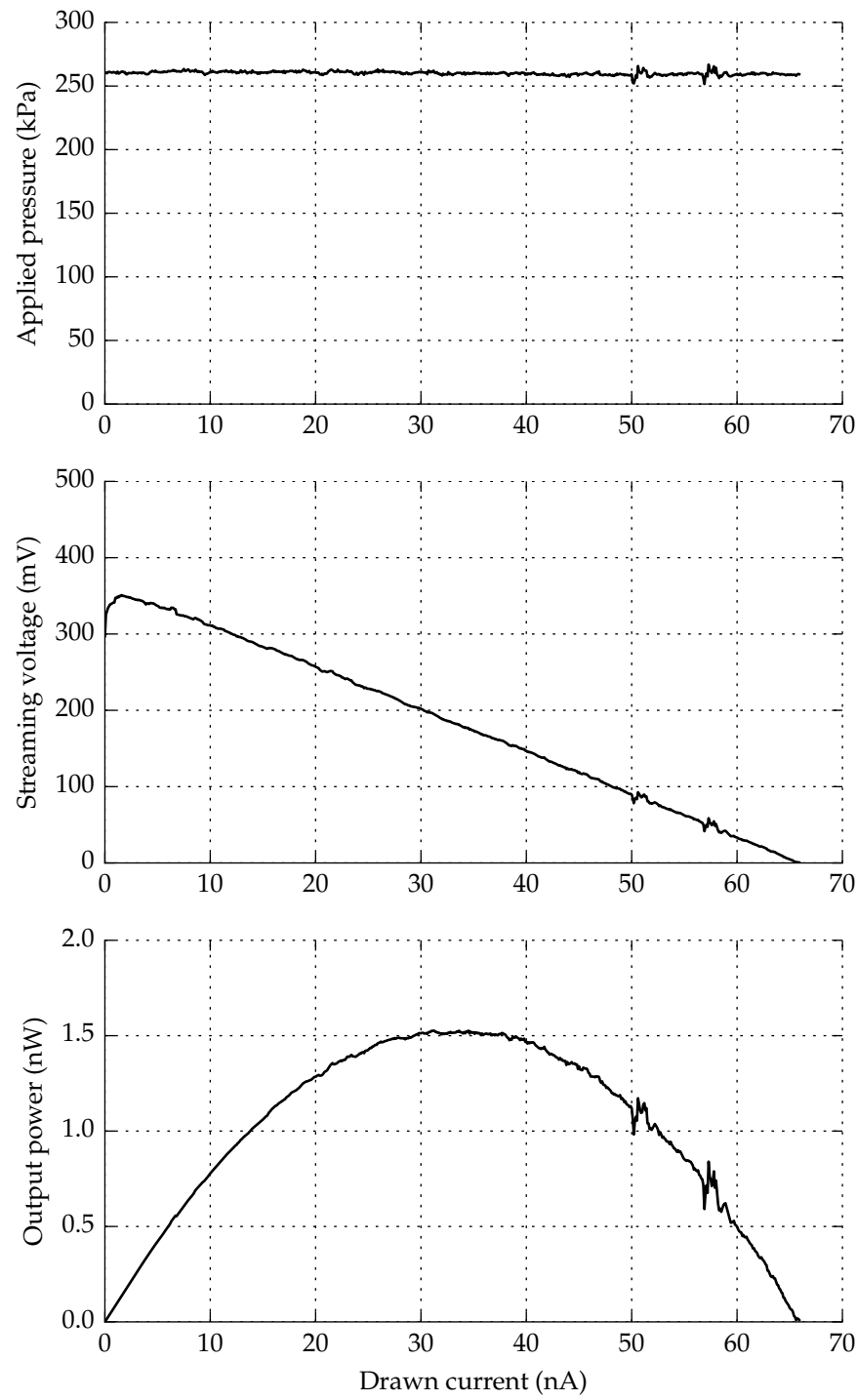


Figure 3.13: Plot of output power versus effective load resistance for a $71 \mu\text{m}$ high channel at a pressure of 260 kPa.

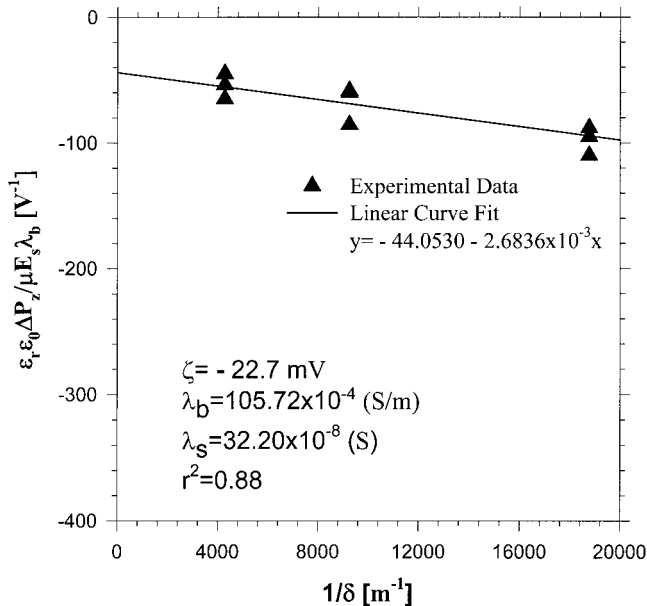


Figure 3.14: Measured data from Gu and Li’s paper on streaming cells relating the streaming voltage and pressure differential to the channel height with distilled water as the working fluid

Comparing the streaming voltage measurements taken from each of the ten cells to the measurements made by Gu and Li yielded surprising results. In their paper [61], they determined the zeta potential (ζ) and surface conductivity (λ) by plotting measurements and fitting a linear equation to their data. They used the y-intercept of the resulting line to give the inverse zeta potential and the slope of the line gave information about the surface conductivity.

Their results for three streaming cells are shown here (taken from [61]) as figs. 3.14 and 3.15. The first (fig. 3.14) shows measurements when distilled water is used as the working fluid; the second (fig. 3.15) shows the measurements for a weak saline solution. It is interesting to note that they have what looks to be fairly linear data, although it is hard to tell with only three channel sizes.

By comparison, fig. 3.16 plots the same variables from measurements

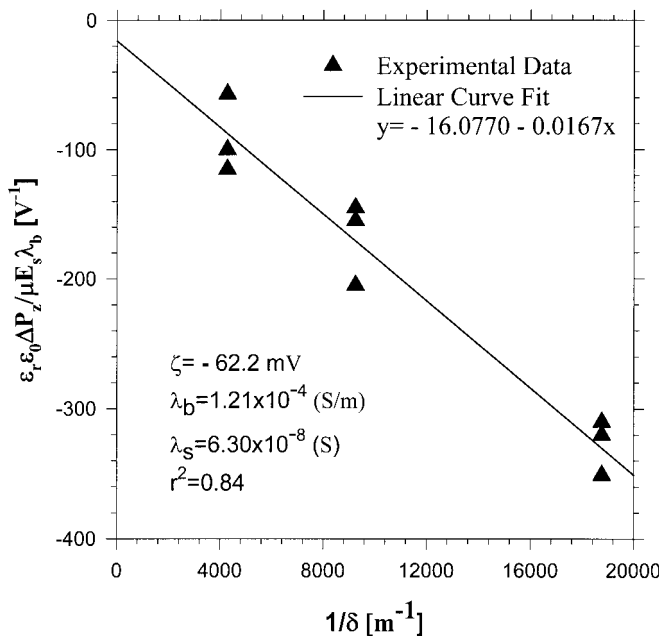


Figure 3.15: Measured data from Gu and Li's paper on streaming cells relating the streaming voltage and pressure differential to the channel height with a 1 mmol sodium chloride solution as the working fluid

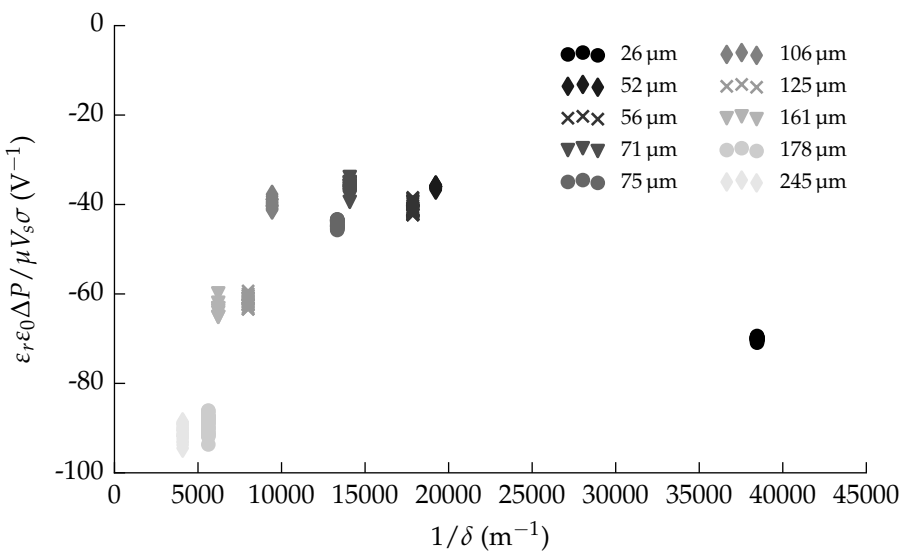


Figure 3.16: Scatter plot with results of streaming cell measurements in terms of those made by Gu and Li [61] (for comparison).

taken from the ten streaming cells fabricated here. In this graph λb has been replaced with σ , where both refer to the bulk conductivity of the solution; and E_s has been replaced with V_s , were both refer to the streaming potential. The response to variation of channel height is clearly non-linear. Their method of finding the zeta potential rests on the following rearrangement:

$$\frac{\varepsilon_r \varepsilon_0 \Delta P}{\mu V_s \sigma} = \frac{1}{\zeta} + \left(\frac{2 \lambda}{\zeta \sigma} \right) \frac{1}{\delta} \quad (3.12)$$

where λ is the surface conductivity and δ is the channel height. So as the channel height (δ) tends to infinity, the left hand side tends toward the zeta potential (ζ). This notion seems counter intuitive since the zeta potential is defined at the plane of sheer (as shown in fig. 2.7), relative to the solution bulk. The equation is stating that no-matter how far you separate the walls, the minimum voltage-pressure gradient you can get is still set by the zeta potential.

Measurement of the output power generated by the 71 μm streaming cell are promising. From this measurement the power transfer curve is evident. Referring back to the model presented as fig. 3.1, we can now calculate the channels internal electrical resistance (R_{cell}). We know from the graph that the maximum power transfer occurred at a current of 33.5 nA with a streaming voltage of 182 mV. Via Ohm's law this equates to a load resistance (R_{out}) of 5.43 M Ω , which from the maximum power theorem we know must be equal to the cells internal resistance.

3.6 Concluding remarks

Conversion of mechanical pumping into electrical energy can be done with narrowly separated plates of glass. The conversion efficiency seen here was

low, much lower than reported in the literature. A channel 1 cm by 3 cm by 71 μm produced 1.5 nW under a pressure differential of 260 kPa. That took 359 mW of pumping power to produce, yielding an efficiency in the order of 0.1 $\mu\%$. Precision engineering, with regards to cell construction, will likely lead to greater efficiency. This is based on reports from the literature, where higher efficiency channels utilised much narrower channels.

Measurements of ten streaming cells were compared to the results published by Gu and Li. The linear relationship of Gu and Li between channel height and their plotted parameter could not be reproduced. Instead, results showed a highly non-linear relationship as shown in fig. 3.16. The gradient of measurement points within the range of channel heights measured by Gu and Li is reversed. The reason for the discrepancy is not clear.

The streaming voltage was found to scale linearly with the applied pressure. This could potentially be useful as a means of sensing water flow rates. A dual purpose such as power sourcing and flow measurement lends itself well to water metering applications.

Chapter 4

Applicability to Water Metering

Water metering is becoming increasingly common throughout the world [10]. Sourcing and processing drinkable water is an expensive task. Cheap and reliable methods for reading water meters is important. As supplies of drinkable water become constrained, volumetric pricing will become increasingly common. Harvesting energy at the location of metering would eliminate the need for batteries. If energy harvesting could be done without moving parts, the lower component wear would lead to increased service life versus mechanical means. This section investigates the feasibility of using streaming cell technology as a means of powering electronic water meters.

Chapter 3 discussed electric power generation from streaming cells. A $0.2\ \mu\%$ conversion efficiency from water flow and pressure was demonstrated. Also, streaming voltage was found to be directly proportional to the pressure across a cell. Can that pressure dependence be used as a method to meter water consumption while generating power? Probably. However, questions like this are only relevant if the harvester is feasible. Its feasibility is dictated by whether or not it can provide enough energy. To find that out, the following questions must be answered:

1. What quantity of energy is there available to harvest?
2. What fraction can be harnessed?
3. How much power do we need?

The second question was answered in chapter 3, (0.0002 %); and third will be answered in the in chapter 5. This chapter addresses the amount of energy available to harvest in a typical domestic setting.

4.1 Current Trends in Water Metering

In New Zealand - Auckland City, Tauranga City, Nelson City, Whangarei District, and the Tasman District have already implemented water metering [55]. For residents of Wellington, New Zealand's capitol city, water metering is optional. In metered locations, meter readers must manually read the display of each meter; a long and laborious task.

Automatic meter reading systems (AMR) are an alternative method of collecting that data. Hamilton City Council is trialling such systems in remote areas in the hopes of adopting them for wide-spread use. There are two types of automatic meter reading systems: an external reader/transmitter that attaches to a compatible meter, or a meter built specifically for the purpose. These systems offer advantages separate from making the meter-reader redundant. Increased billing frequency helps customers reduce their consumption by giving more frequent feedback. They remove the need to access the customer's property [10]. Electronic analysis of the meters readings provides an easy way to detect water leaks.

It is estimated that 10 % of post-meter water consumption is due to leakage in the residential sector [5]. Measuring night-time water flow is a convenient way of estimating flow due to leakage. Britton et al. show



Figure 4.1: Photograph of a domestic water meter, and installation, (Kent PSMT 25mm) typical of an Auckland residential area.

that communicating with customers whose homes showed signs of leakage that a night-time flow reduction of 89 % is achievable. In contrast, a control group's night-time usage increased by over 50 % during the same time-frame. Benefits of automatic water metering are not only geared toward billing, but improving the network as a whole.

Domestic water meters are typically installed at a property's boundary, in a plastic box set into the ground. An installation typical for an Auckland residential area is presented as fig. 4.1. The meter is installed over five meters into the property from the road-side. Because of its location, it is not feasible to connect it to a source of power. No commercially available domestic energy harvesting water meters, suitable for burial, exist on the market as of 2015.

A common configuration for wireless automatic meter reading is to have



Figure 4.2: Photograph of the a wireless transmitting module from Waterware NZ. The device attaches to a compatible water meter and contains its own battery [35].

a reader/transmitter device that is separate to the meter itself. Such a device usually attaches to the meter's display or has a wire connecting it to the meter. Being detachable and tamper-proof means it must be powered by batteries. A commonly stated battery life for such units is ten years [35], close to a battery's shelf-life. We investigate the possibility of replacing these batteries with a streaming cell based energy harvester. A harvester removes the need for batteries, but needs to be plumbed into the water feed. The resulting device would most likely replace the meter, as opposed to being an attachment.

4.2 Envisioned harvester design

In chapter 3, energy was converted between fluid-mechanical to electrical using a single channel. Harvesting for electronic water meters will require more energy than that channel could produce. There are multiple ways of scaling the streaming cell design used in chapter 3. The channel can be made wider, doubling the width will double the output power; multiple channels can be stacked together, multiplying the output by the number

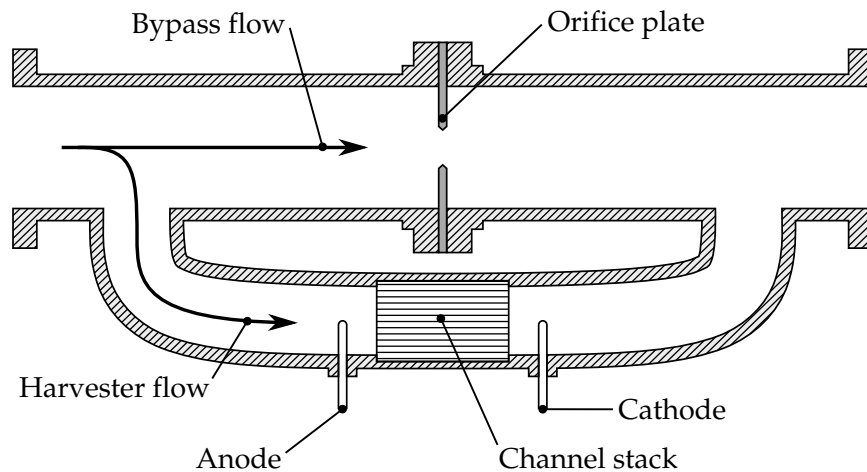


Figure 4.3: Diagram showing the intended design of streaming cell harvester suitable for domestic connection.

of channels formed. Scaling the harvester is not considered a problem, but the pressure drop it develops is. High fluid resistance is inevitable since practical efficiencies are only obtained when the internal dimensions are small.

To control the pressure drop across the harvester, the mechanical design shown in fig. 4.3 is proposed. It gives the capability of controlling the hydrodynamic resistance of the unit as a whole by means an orifice plate. The plate sits in the “main line” causing a pressure differential in proportion to the flow rate. An orifice plate with a hole equal in diameter to the main pipe causes no pressure differential as it causes no flow obstruction. Conversely, a plate without a hole forces all liquid through the harvester, causing the maximum pressure differential. Using an appropriate sized orifice plate, the customer will be unaware of the harvester’s presence and a suitable pressure differential will be developed. For the sake of analysis we assume the orifice plate will be sized to match the pressure loss of a mechanical meter. This assumption means the amount of harvestable energy is equal to the amount dissipated in a mechanical water meter. The following

Item	Measurement	Summer	Winter	Unit
Shower	Duration	6.6	7.0	minutes
	Volume	50.0	52.5	litres
	Flow	8.1	8.0	litres/minute
	Frequency	0.9	0.9	/person/day
Washing	Volume	122	123	litres
	Frequency	0.35	0.36	/person/day
Toilet	Volume	6.6	6.8	litres
	Frequency	4.9	4.5	/person/day

Table 4.1: Average usage characteristics for a shower, washing machine and toilet. Data obtained from [21].

section quantifies the amount of energy a water meter dissipates over an average week in a typical Auckland home.

4.3 Quantifying harvestable energy

This section estimates the quantity of energy available to a harvester placed in a domestic feed. Using a bypass pipe with an orifice plate the pressure drop across the harvester can be controlled. This means the pressure drop across the harvester can be set to match that of a mechanical meter. The amount of harvestable energy under this assumption is the amount of energy dissipated inside a mechanical meter.

Heinrich monitored water consumption of 51 homes throughout Auckland in 2008 [21]. His report shows the majority of domestic water is consumed by the shower (30 %), washing machine (27 %) and toilet (20 %). Together these account for over 75 % of domestic water consumption. Data from table 4.1 was used to build a typical water usage profile. Heinrich published a similar report in 2007 that contained water flow profiles, the flow profile of the toilet has been taken from that report [20].

Figure 4.4 shows the flow rates for each of the three items considered

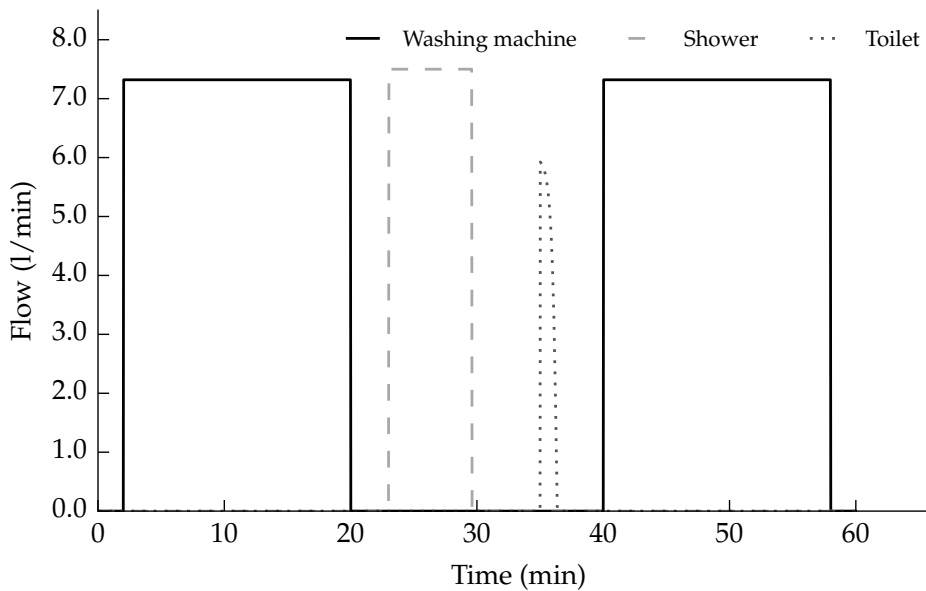


Figure 4.4: Sample profile showing constructed instances of washing machine use, a shower and a toilet flush. The washing machine's wash and rinse cycles are separated in time.

(toilet, shower and washing machine). Volumes for each of the events, and flow profile of the toilet, match the measurements reported by Heinrich. Specifically, the total volumes for each are: 1221, 49.51 and 6.221 for the washing machine, shower and toilet respectively.

The Kent 25-PSMT series mechanical water meter is the most commonly installed water meter in the Auckland district [56]. Figure 4.5 shows the head-loss, or pressure differential, versus flow rate for the Kent PSM range of meters. The following equation fits the trace representing the 25 mm PSMT meter:

$$\Delta P = e^{3.725 \log(flow) - 9.5} \quad (4.1)$$

Equation (4.1) is plotted in fig. 4.6 on linear scales.

Knowing the pressure differential as a function of flow provides a means of converting between flow and power dissipation. Like an electrical resis-

Pressure Drop Graph

Pressure Drop Graphs
 (Typical) 15, 20 & 25mm
 PSM water meters

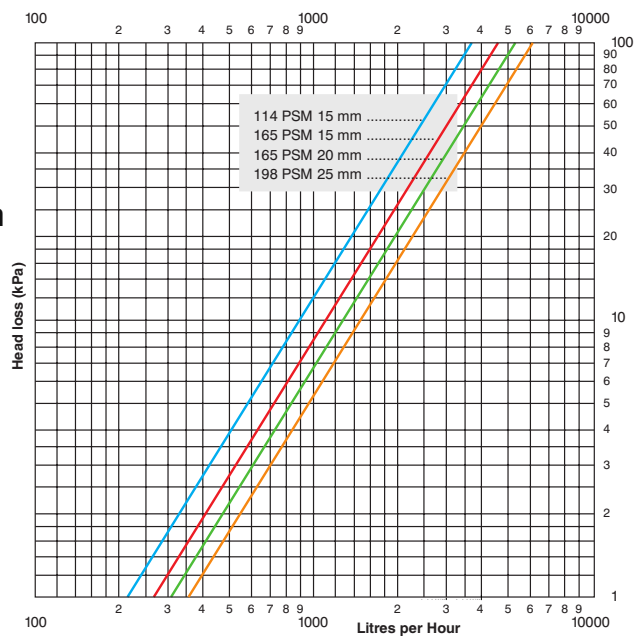


Figure 4.5: Log-log graph showing the pressure developed across the Kent PSM series mechanical water meters. Taken from [17].

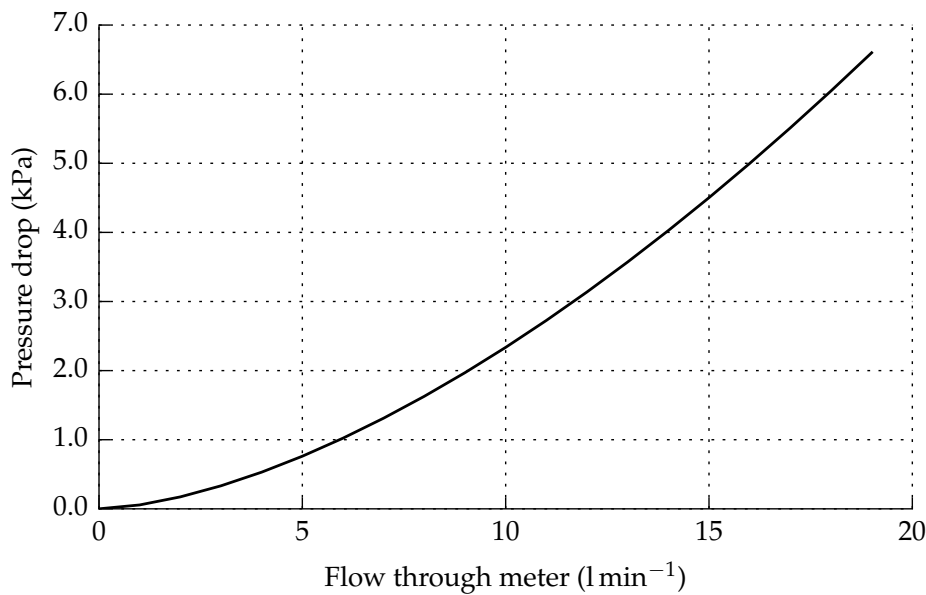


Figure 4.6: Graph showing fitted curve to the pressure loss graph presented as fig. 4.5.

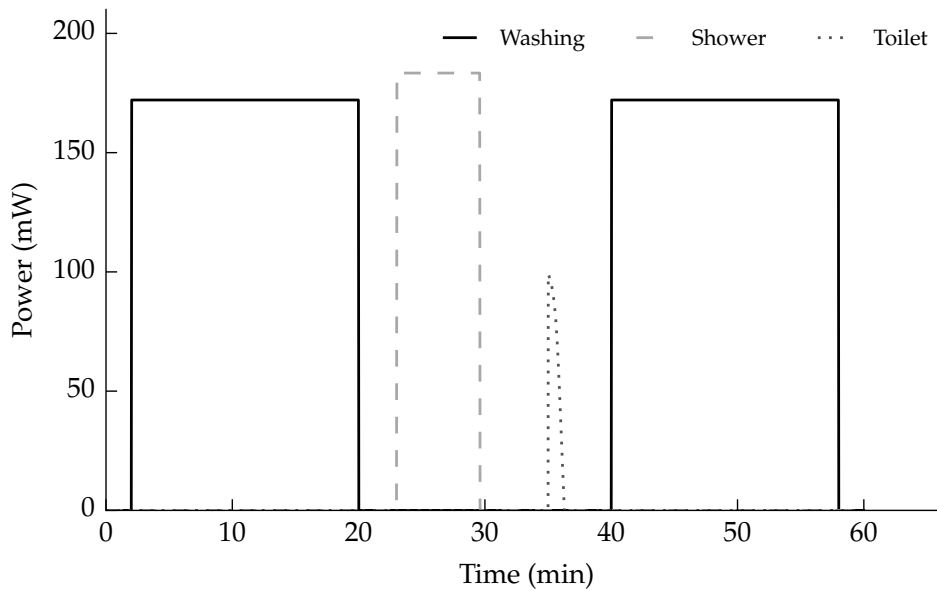


Figure 4.7: Calculated power dissipation by a typical domestic mechanical water meter for each of the sample profile events.

tance, power dissipated by a fluid-flow obstruction is the product of the difference in driving force across the resistance and the flow through it. In this case the driving force is pressure and the flow is volumetric.

$$\text{power} = \text{pressure} \cdot \text{flow}$$

$$\begin{aligned} \text{Watt} &= \text{Pascal} \cdot \frac{\text{cubicmeter}}{\text{second}} \\ \frac{\text{kg} \cdot \text{m}^2}{\text{s}^3} &= \frac{\text{kg}}{\text{m} \cdot \text{s}^2} \frac{\text{m}^3}{\text{s}} \end{aligned} \quad (4.2)$$

(4.3)

Section 4.3 shows the units that will be used to determine power dissipation and ensures they balance. Running the profiles of fig. 4.4 through eq. (4.1), with relevant unit conversions, yields fig. 4.7. It shows the power dissipated within the water during each event. Integrating each trace with respect to time gives the total energy lost over the course of each. Those energy figures

Washing	172J
Shower	72.6J
Toilet	5.07J

Table 4.2: Calculated energy dissipation within a mechanical water meter for a single washing machine cycle, shower and toilet use.

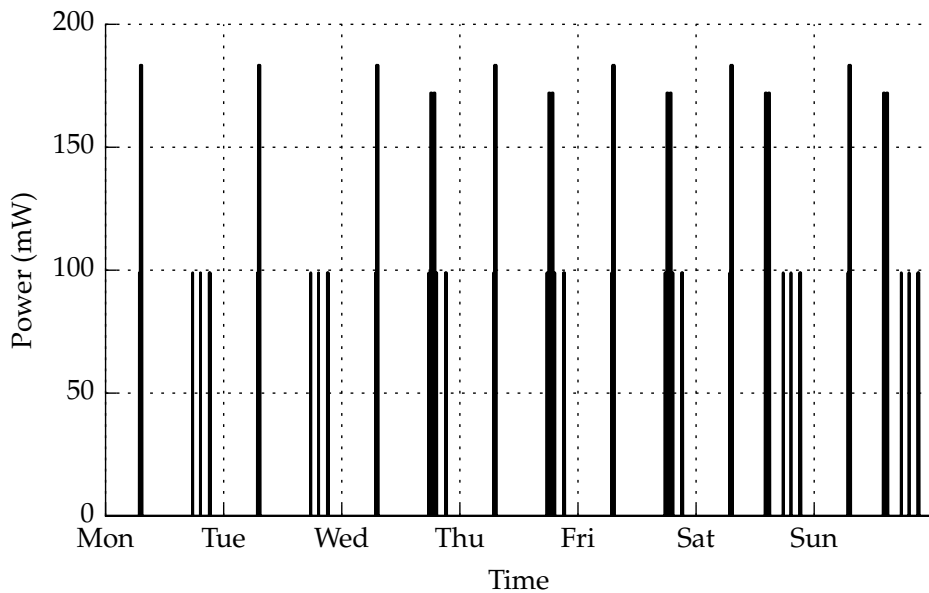


Figure 4.8: Profile of power dissipation within a mechanical water meter over a week for a two occupant dwelling.

are provided in table 4.2.

Average use frequencies for each event type were been reported by Heinrech, as shown earlier in table 4.1. Using these figures, and by selecting appropriate times of day, an energy dissipation profile representative of one week was constructed. Five uses of a washing machine, fourteen showers, and fifty six toilet flushes occur during this time. This profile is shown as fig. 4.8. The profile fits usage figures of a home having two occupants, although most homes have more than two occupants. A systematic bias toward underestimating typical water usage has been used where possible. This underestimation also occurs by not including water use by means

Washing	860J
Shower	1020J
Toilet	283.9J

Table 4.3: Calculated total energy dissipation over a period of one week within a mechanical water meter for typical use of a washing machine, shower and toilet.

other than washing machines, showers or toilets. The intention is that the feasibility of harvesting, if the results showed near a possibility, would be more robust in light of these biases. Table 4.3 combines the energy dissipation for each event type over profile duration. The total energy dissipated in the meter over the course of a week is 2.16 kJ. Daily energy available is expected to fluctuate due to sporadic use of the washing machine in most homes. Ignoring washing machine use, indicative of weekday consumption, the quantity of harvestable energy is expected to be about 280J per day.

Knowing the quantity of energy available to a harvester is a key factor determining its feasibility. The efficiency of converting energy into the electrical domain was measured in chapter 3 and was found to be $0.2\ \mu\%$. Calculation shows the measured cell would yield 560 nJ of energy per day. Energy output that low is unlikely to be sufficient for automatic meter reading. The literature indicates the efficiency measured in chapter 3 was low. It may still be possible to close the gap between what we can produce and what we need. The amount of energy required to run an electronic water meter is estimated next.

Chapter 5

A Harvester's Energy Requirements

The amount of energy lost in a mechanical water meter has been estimated, as has the fraction of that energy which can be harnessed. Now, the amount of energy required to operate an electronic water meter is estimated. This estimation will reveal how much further the cells built earlier would need to be improved.

5.1 Microcontrollers

Central to the operation of an electronics water meter is the microcontroller (MCU). The primary function of the microcontroller is to read and log the amount of water consumed by the meter. The program contained on the controller will also decide when to transmit that data and monitor energy usage. It is therefore a key component of the electronic meter and is expected to consume the majority of its energy.

In this chapter compares power consumption and operational efficiencies of six low power MCUs deemed suitable for use in a water meter. The microprocessors to be investigated are low power, general purpose, 8-bit processors from Microchip, Atmel and Freescale. Each of the microprocessors will have their energy consumption recorded while carrying out various

functions. Those measured functions are analogue-to-digital conversion, non-volatile memory writes, processing, and sleeping. These functions are believed to be important for the intended application.

5.1.1 Selection of appropriate controllers

The following processors were chosen the three chosen manufacturers.

- Microchip PIC16F1827
- Microchip PIC16F688
- Microchip PIC12F675
- Atmel ATtiny25V
- Atmel ATtiny13V
- Freescale MC9S08QG8

A basic feature comparison of the MCU selection is shown in table 5.1.

5.1.2 Power consumption benchmarks

While testing the power consumption of these microprocessors precautions were taken. The chips must be configured to ensure that do not consume more power than is necessary. Where possible, the chips were configured to have each of their pins set to outputs, which were held high while being tied to Vdd via $10\text{k}\Omega$ resistors. All chips had their peripherals disabled (where appropriate) including any watchdog timers and brownout detection circuitry. To allow more accurate sleep current measurements, the chips were placed in a chip carrier with $10\text{k}\Omega$ resistors soldered between the pins (except ground and Vdd) and Vdd. The chip and carrier was then washed in

	PIC16F1827	PIC16F887	PIC16F688	PIG12F675	ATtiny25V	ATtiny13V	MC9S08QG8
Vdd (min)	1.8	2.0	2.0V	2.0	1.8	1.8	1.8
Vdd (max)	5.5	5.5	5.5V	5.5	5.5	5.5	3.6
I(sleep)	30nA	50nA	50nA	1nA	<100nA	<100nA	450nA
CLOCK (min)	31kHz	31kHz	31kHz	31kHz	16kHz	16kHz	1MHz
CLOCK (max)	32MHz	32MHz	8MHz	4MHz	16MHz	9MHz	10MHz
EEPROM	256B	256B	256B	128B	128B	64B	+
Serial	USI	USI	USI	—	USI	—	USI
USART	UART	UART	UART	—	—	—	—
ADC	10bit	10bit	10bit	10bit	10bit	10bit	10bit

#Has 8,192 bytes of software programmable flash (16 pages of 512 bytes each).

†Has 256 bytes of software programmable flash (4 pages of 64 bytes each).

Table 5.1: Feature comparison of selected MCUs.

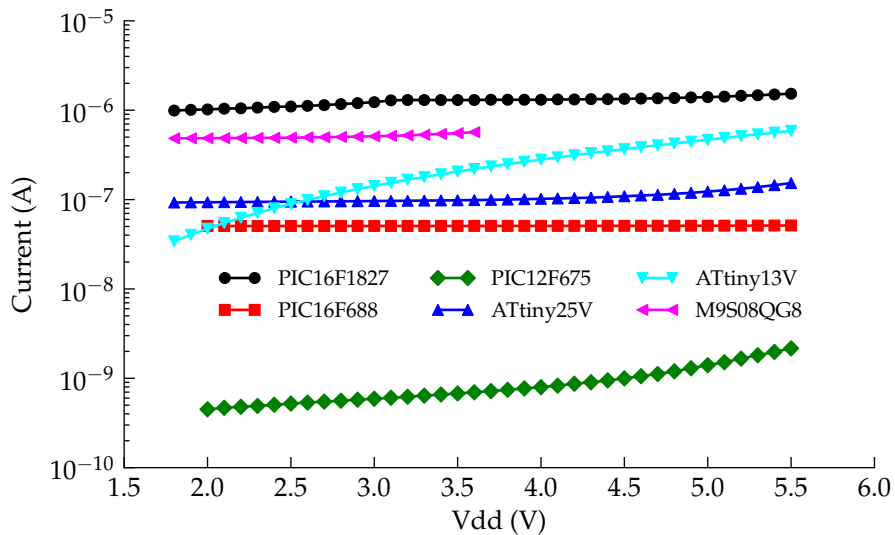


Figure 5.1: Current consumed by investigated MCUs while in sleep mode.

isopropyl alcohol and dried before being suspended by connections to the measurement device. This was done to reduce any current leakage between pins due to fingerprints or dirt. Measurements were carried out using the Agilent E5270B Precision Measurement Mainframe. This device has been used for most other measurement situations throughout this thesis for its high impedance inputs and measurement accuracy.

Sleeping

A microprocessor in sleep mode is essentially powered off, the difference being that volatile data is preserved. In order to consume as little power as possible an MCU should spend as much time in sleep mode as possible. Therefore, power consumption in sleep states will determine a large part of the chips overall power consumption.

Figure 5.1 shows the amount of current consumed by each MCUs while in their deepest sleep states. Surprisingly, the PIC16F1827 consumes the most current in this state, almost one thousand times more than the specified

	Instructions
PIC16F1827	53
PIC16F688	35
PIC12F675	35
ATtiny25V	120
ATtiny13V	120
MC9S08QG8	145

Table 5.2: Instruction set size for each tested MCU.

sleep current of 30 nA [37]. The Freescale MC9S08QG8 consumed energy at an average of 11% higher than specified [18]. Both the Atmel ATtiny13V and ATtiny25V fell within their specification, [1, 2] respectively. The Microchip PIC12F675 fell within specification [36] and was clearly ahead in terms of minimum current draw during sleep.

There appears to be a trade-off between the two Atmel processors in the way of minimum power consumption and minimum response to Vdd. The ATtiny13V required approximately 2.7 times less power than the ATtiny25V at 1.8V, but above 2.5V the ATtiny25V is more draws less current.

As the PIC16F1827 was so far off its specified value, measurements were repeated numerous times using code written in both assembler and HI-TECH C. A total of five different processors were tried, all giving the same result. All steps outlined in the PIC16F1827's datasheet to reduce power consumption had been followed.

Disclaimer on processing

Measuring the amount of power it takes to process information is not a simple task. The way each chip carries out processing operations internally can be quite different from one another, even though they all produce the same result.

To illustrate, algorithm 5.1 shows a simplified programme. To deter-

Algorithm 5.1 Simple C-code representation of a branch instruction.

```

1     if (danger >= 5) flight();
2     else flee();

```

Algorithm 5.2 Pseudo machine-code representation of a branch instruction.

```

1     load 5 into register 001
2     load danger into register 002
3     branch-if-greater-or-equal 001 002 flee_call
4     call-subroutine fight
5     jump-to continue
6     [flee_call]
7     call-subroutine flee
8     [continue]

```

mine whether the programme's outcome, the processor must first evaluate whether 'danger' is greater than or equal to five. Then it will either branch to the function 'flight' or continue on to execute the function 'flee'.

Algorithms 5.2 and 5.3 demonstrate two different ways of implementing 5.1 using pseudo machine-code. The decision of which is best is made by the compiler, which should take the instructional efficiency of the specific MCU into account. This is an overly simplistic example, but it illustrates that there are multiple paths leading to the same result. Importantly, not all of those paths require the same amount of effort on the processors behalf. This means that the compiler's ability to optimise code efficiently plays a role in determining the overall performance of the chip. This also means

Algorithm 5.3 Psudo machine-code representation of an alternative branch instruction.

```

1     load danger into register 001
2     subtract-from-register 001 5
3     branch-if-minus 001 fight_call
4     call-subroutine flee
5     jump-to continue
6     [fight_call]
7     call-subroutine fight
8     [continue]

```

that the programmer shouldn't need to worry too much about instructional efficiency as the compiler should transform C-code into machine code that best suits the target MCU.

Another factor in processing efficiency comes down to the number of different instructions it can do. This list of instructions a processor is capable of is called its instruction set. Most 8-bit MCUs are based on reduced instruction set computing (RISC) architecture, as opposed to complex instruction set computing (CISC). When compared to a CISC based CPU, a RISC based chip is simpler and therefore usually cheaper to produce and simpler to program. However, "Instruction traces from CISC machines consistently show that few of the available instructions are used in most computing environments" [22], meaning that many of the extended operations in CISC designs are underutilised. Processors with smaller instruction sets are capable of achieving the more complex operations by chaining multiple instructions together. This means that processors with smaller instruction sets will take longer to achieve certain instructions. Finally, the frequency of a microprocessor isn't necessarily the frequency at which it performs operations, although sometimes it is. For instance, the Atmel and Freescale microprocessors perform one instruction per clock cycle, whereas the Microchip processors perform one instruction every four clock cycles.

Power consumed while processing

Results in this section are expressed in terms of instructions per second (IPS). The Microchip PIC16F1827 displayed the lowest energy usage with $10\text{ }\mu\text{A}$ while clocking 7.75 kIPS (as shown in fig. 5.2). Microchip MCUs complete one instruction every four clock cycles, so the 7.75 kIPS actually corresponds to a standard clock frequency of 31 kHz.

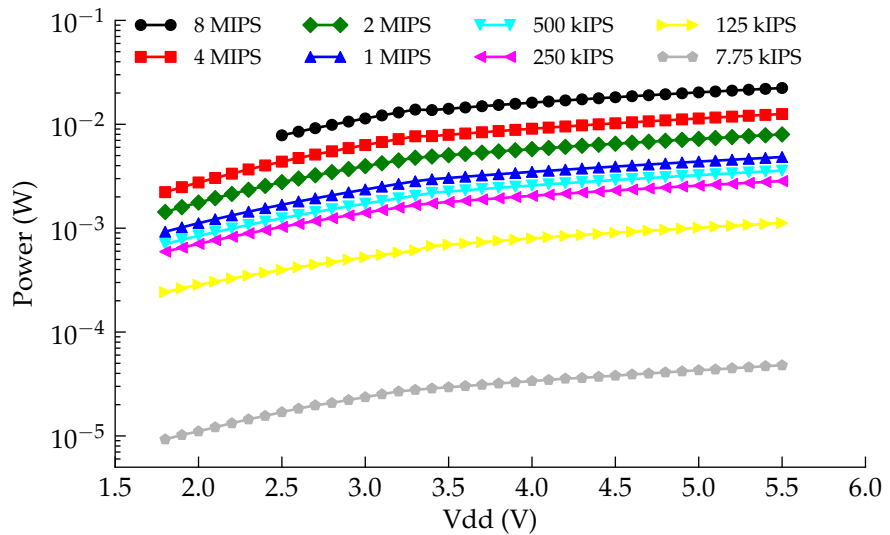


Figure 5.2: Power consumed by the PIC16F1827 while processing

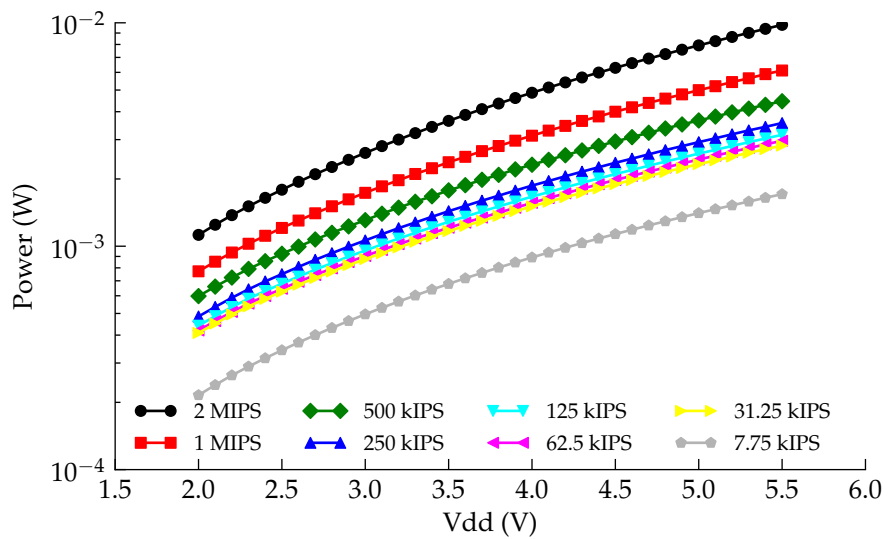


Figure 5.3: Power consumed by the PIC16F688 while processing

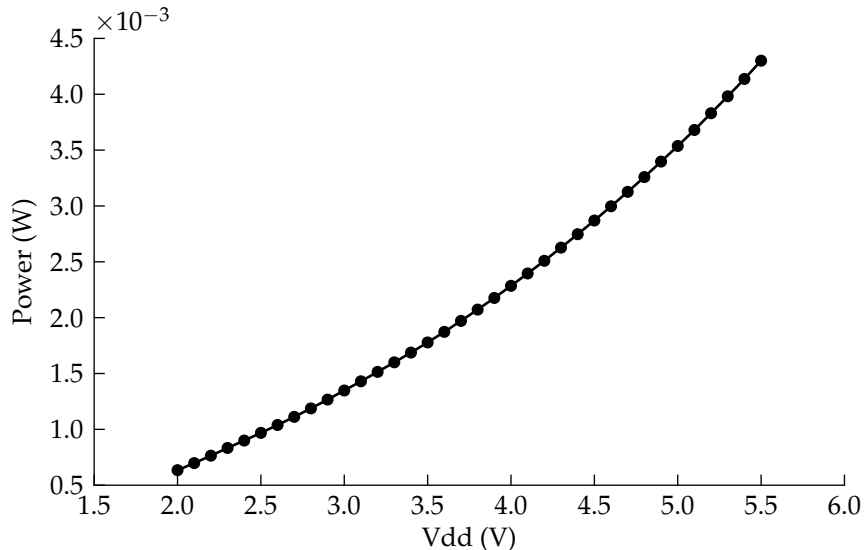


Figure 5.4: Power consumed by the PIC12F675 while processing

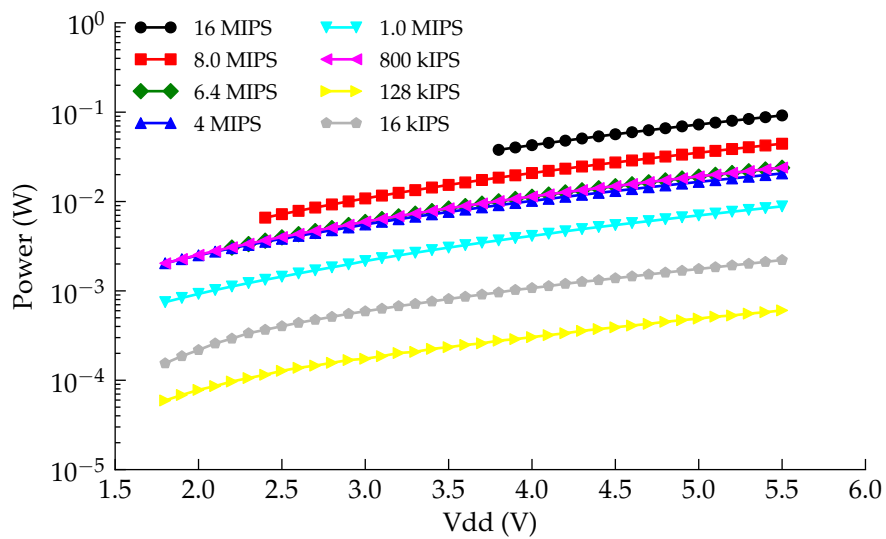


Figure 5.5: Power consumed by the ATtiny25V while processing

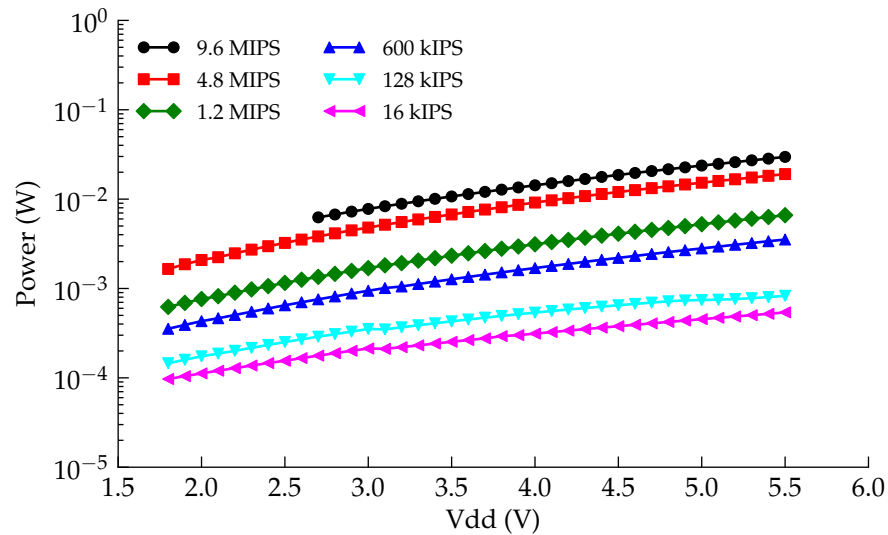


Figure 5.6: Power consumed by the ATtiny13V while processing

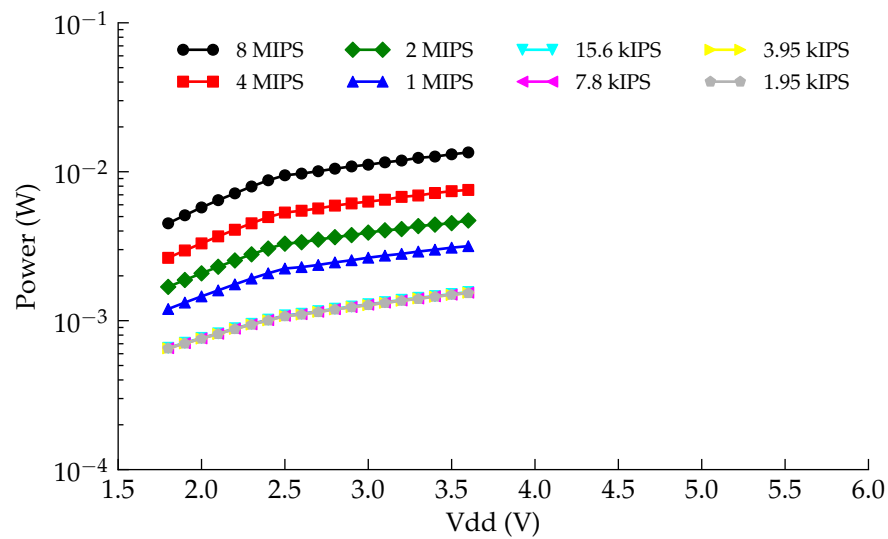


Figure 5.7: Power consumed by the MC9S08QG8 while processing

Figure 5.3 shows the PIC16F688 consumes less power than the PIC16F1827 at low voltages for the same instruction rates (except at 7.75kIPS). There appears to be a flatter response in power consumption with respect to Vdd in the PIC16F1827. Again, this appears to be a similar trade-off to that was mentioned earlier (in fig. 5.1) with the Atmel chips.

The PIC12F675 (??) used approximately the same as the PIC16F688 (fig. 5.3) for its 1 MIPS trace. Figures 5.5 and 5.6 show both Atmel MCUs having similar requirements. The MC9S08QG8, although being able to clock the slowest, performed very poorly at low frequencies. At 1.95 kIPS it consumed approximately the same amount of power as the Microchip MCUs operating at 1 MIPS.

Joules of energy consumed per instruction cycle

A convenient, and more insightful way to interpret the previous processing power consumption graphs is to calculate the energy spent per instruction performed. The energy cost of an instruction cycle can be calculated using equation 5.1.

$$E_i = \frac{I \times Vdd}{f_i} \quad (5.1)$$

where E_i is the number of joules consumed per instruction, I is the current draw, Vdd is the input voltage and f_i is the instruction frequency.

Figure 5.8 compares the most energy efficient operating conditions of each of the tested chips. What is most interesting about this graph is amount of overlap between each of the chips. Also, these greater efficiencies occur at high operating frequencies. A simple rule of thumb for selecting the most power efficient operating frequency based on these results is to choose the highest frequency where the MCU can operate over its full input voltage

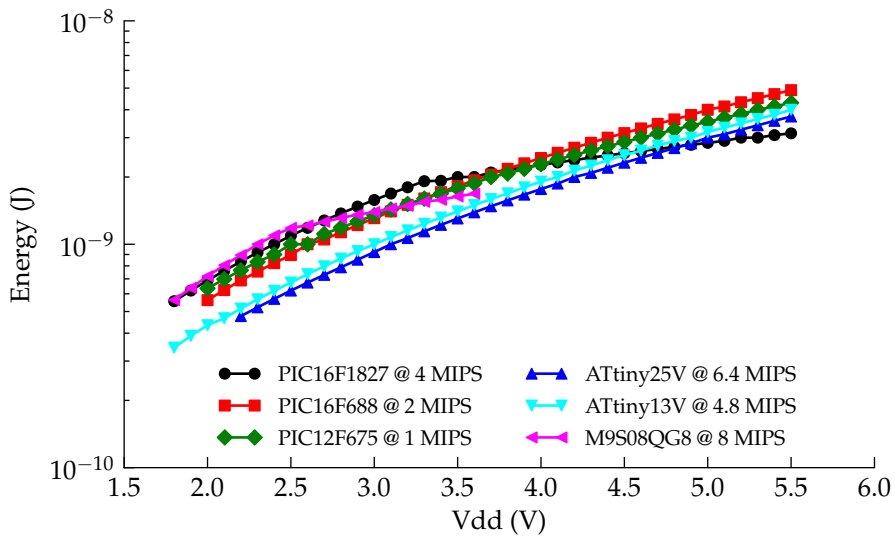


Figure 5.8: Per instruction cycle energy consumption comparison

Algorithm 5.4 Benchmarking algorithm

```

1     unsigned short lfsr = 0xACE1u;
2     unsigned period = 0;
3     do {
4         lfsr = (lfsr >> 1) ^ (- (lfsr & 1u) & 0xB400u);
5         ++period;
6     } while(lfsr != 0xACE1u);

```

(Vdd) range. For comparison, figure 5.9 shows the trade-off made when selecting a higher frequency, which is typical across the range of MCUs tested.

Performance benchmark

Calculating the amount of energy consumed per instruction only shows part of the processors efficiency. The amount of processing done per instruction is not taken into account in such measurements. Some MCUs have extra instructions that are designed to help speed-up code execution by combining commonly used sets of instructions. To shed light on instruc-

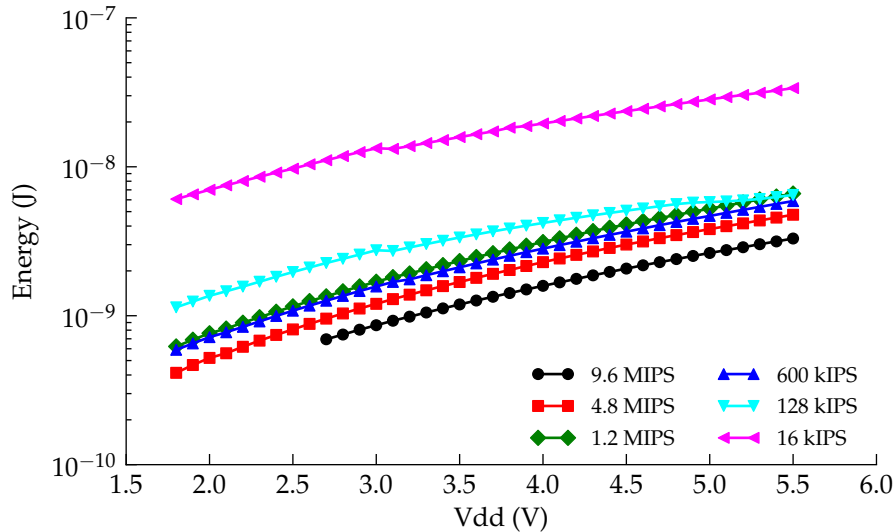


Figure 5.9: Per instruction cycle energy consumption of the ATtiny13V

tional efficiency, the number of instructions each of the processors takes to complete a benchmark function is found. This will allow for a more accurate representation of execution efficiency. The function used to benchmark each of the processors is a linear feedback shift register based pseudo-random number generator [?]. It is well suited to an 8-bit microprocessor as it requires no complex math functions, uses little memory and has a well defined end. The code for this function is shown as algorithm 5.4. It starts with a 16-bit number and runs it through the linear feedback register in a tight loop until the initial value of the 16-bit feedback register is produced again. This function steps through every possible combination of bits possible in a 16-bit number (except zero; 65535) in a pseudo-random order before exiting the loop. The function combines the exclusive-OR (XOR), bit shifting, bitwise AND, increment a value and numerical comparison operations in a tight loop. The benchmarking function was compiled and run on each of the MCUs operating at a range of supported frequencies.

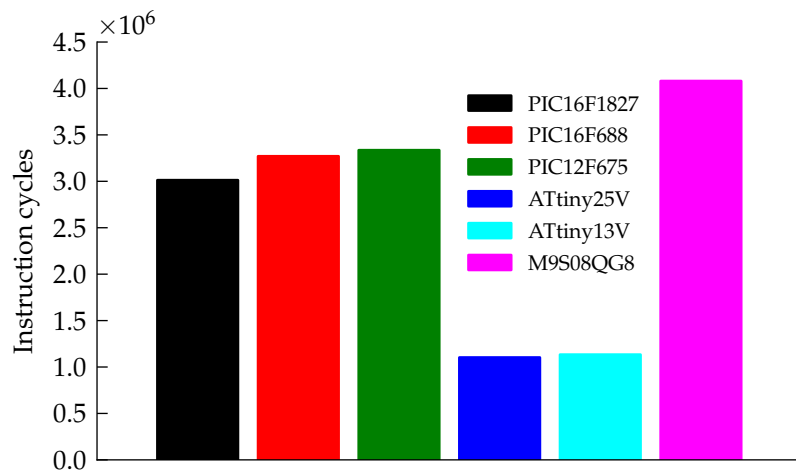


Figure 5.10: MCU comparison of instructions taken to complete a benchmark.

To determine the instructional efficiency, the code was set to toggle the state of a digital output pin. The voltage on this pin was recorded using a Tektronix MSO 4054 oscilloscope. The number of instruction cycles each chip took to complete the benchmark was deduced by multiplying the time taken to complete the benchmark by the instruction cycle frequency. The results of the benchmark are shown in fig. 5.10. To calculate the number of instruction cycles taken by the Microchip family of processors, one quarter of the chip's operation frequency was used. This meant that the number of clock cycles consumed was four times higher. It is clear from fig. 5.10 that the Atmel (ATtiny25V and ATtiny13V) microprocessors are by far the most efficient microprocessor in terms of executing code using a minimum number of instructions of the selection. The reason for this is not clear, but may be due to the larger instruction set, higher compiler optimisation or a combination of both.

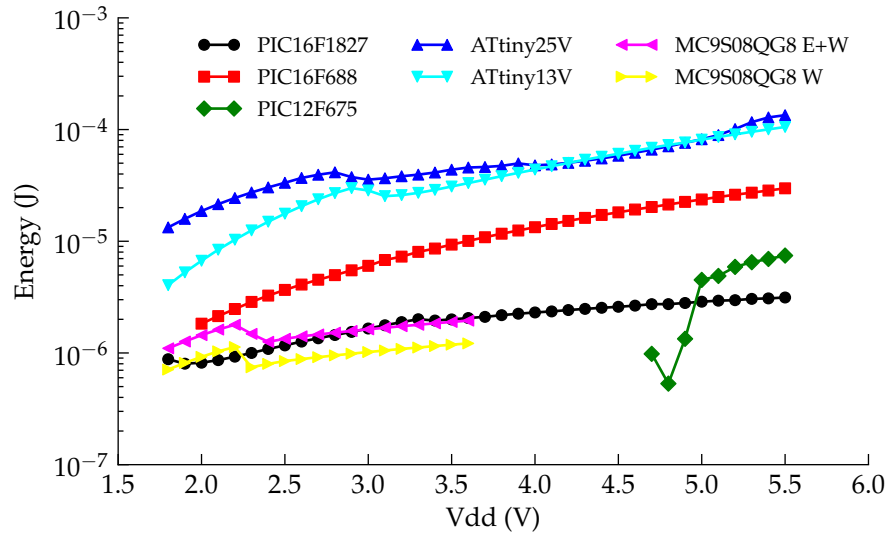


Figure 5.11: Energy consumed by each MCU per non-volatile erase/write operation.

5.1.3 Non-volatile memory

In order for a microprocessor to keep information about its current state and recorded data in the event of power loss it must write to non-volatile memory. Non-volatile memory is implemented as either electrically erasable and programmable read only memory (EEPROM) or Flash memory. Flash memory is similar to EEPROM with the exception that it must be erased in large blocks, or pages, before it can be written to. All of the tested MCUs have on-board EEPROM with the exception of the MC9S08QG8 which has flash memory instead. Table 5.1 shows the amount of non-volatile memory space available on each of the chips.

The energy consumption of each of the chips with EEPROM memory during a 1-byte write operation is shown as fig. 5.11. A particularly curious situation arose whilst testing the PIC12F675 - it's energy consumption was negative when operated below 4.7V. It consumed *less* current while per-

forming write operations than running through the same code loop without performing writes. The measurement was repeated several times and produced the same result. Those data points were excluded from the plot and no further investigation was made to find the reason behind this.

In the case of the MC9S08QG8, which has Flash memory instead of EEPROM, the power consumption in the E + W trace was calculated as $1/512^{th}$ of consumed page erase energy consumption added to the energy cost of a single write operation. The trace labelled W (magenta) shows the energy cost for a single write operation. In order for the MC9S08QG8 to perform a write operation, the destination byte must have already been pre-erased at an earlier point in time. This may be useful for power harvesting since the energy expensive page erase operation, which consumes an average of 3.02e-4 Joules, can be done performed when available energy is plentiful.

These results show that the Microchip and Freescale microprocessors are the most energy efficient when writing to non-volatile memory.

5.1.4 Analog-to-digital conversions.

The operation of an electronic water meter may require that analogue-to-digital conversions are made. Measuring the amount of energy consumed per conversion was done in much the same way as the previous tests. Each of the chips had similar converters feature-wise. Results form the measurements are presented as fig. 5.12.

5.2 Wireless Transmission

Because water meters are typically installed in remote areas where grid connection is unavailable, data must be collected via wireless interface. In Hamilton, a major utility provider has established a wireless mesh network

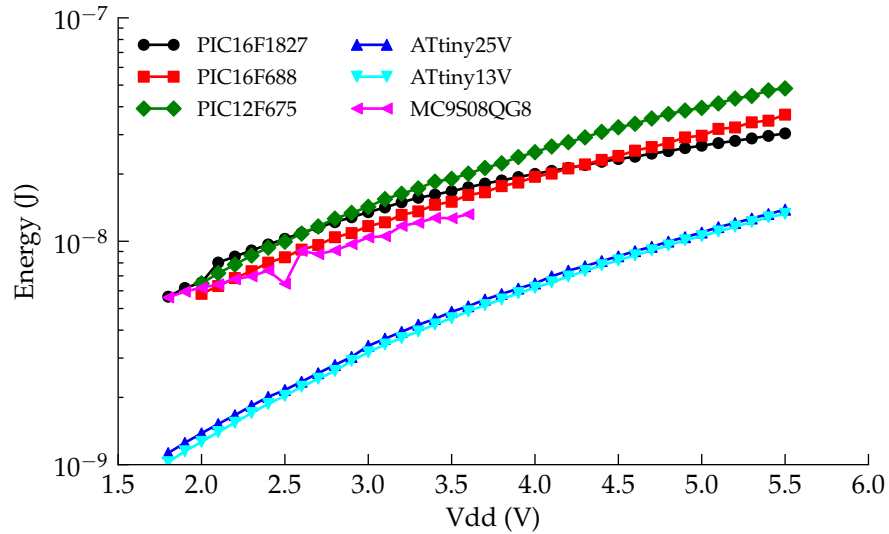


Figure 5.12: Energy consumed by each MCU per ADC measurement.

between smart electricity meters installed in residential homes. That network utilises ZigBee wireless transceivers, making ZigBee an convenient choice for transmitting water metering data [32]. Two types of wireless transmitters were chosen for energy measurement, a HOPE RF RFM12B transceiver and a Digi International Xbee Series 2 transceiver. The power consumption versus time during a wake, send one hundred and sixty bytes, and power down cycle was captured for both transceivers. By integrating the area under this curve the total energy consumed per transmission is found. The transmitters were kept 1 m from there receivers with no obstructions between them. This represents ideal transmission conditions, something that our electronic water meter is very unlikely to encounter. The actual RF reception between a base station and installed meter will vary greatly between installations and weather conditions. For example, wet ground is likely to obstruct RF transmission due to the transmitter being shielded by a more conductive medium. Instead of trying to quantify the

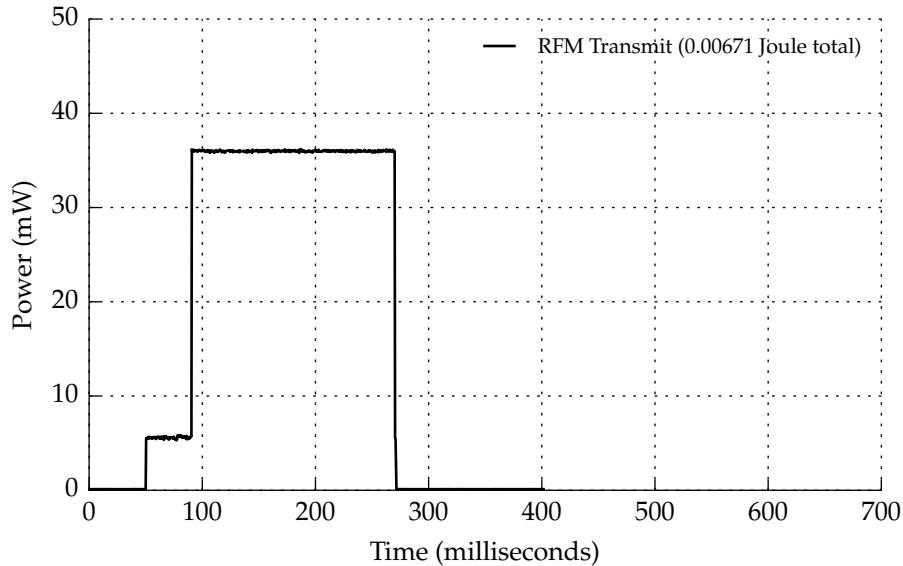


Figure 5.13: Power draw from a HopeRF RFM12B transceiver module.

energy required in those situations, the best case was measured and an estimate of the worst case is estimated to be one hundred times larger. The transmit power can increase by a factor of 320 for the RFM module, however the transmit power only represents a proportion of total power usage. The modules must power up, start their internal oscillators, receive the data to be transmitted and then transmit. I estimate that the difference between the lowest and the highest total power consumption, based on reception alone, will be a factor of 50-100.

The RFM12B was operated at 433MHz, a frequency that is expected to increase the transmission through walls and soil. It has a maximum output power of 5 dBm (3.2 mW) at this frequency. The Xbee has a maximum output power of 0 dBm (1 mW) and operates at 2.4 GHz. Figure 5.13 and ?? show the captured power consumption during the tests. The RFM12B used about half as much energy sending the same packed of data as the Xbee. Combined with its ability to operate at 433 MHz, the RFM12B is a sensible

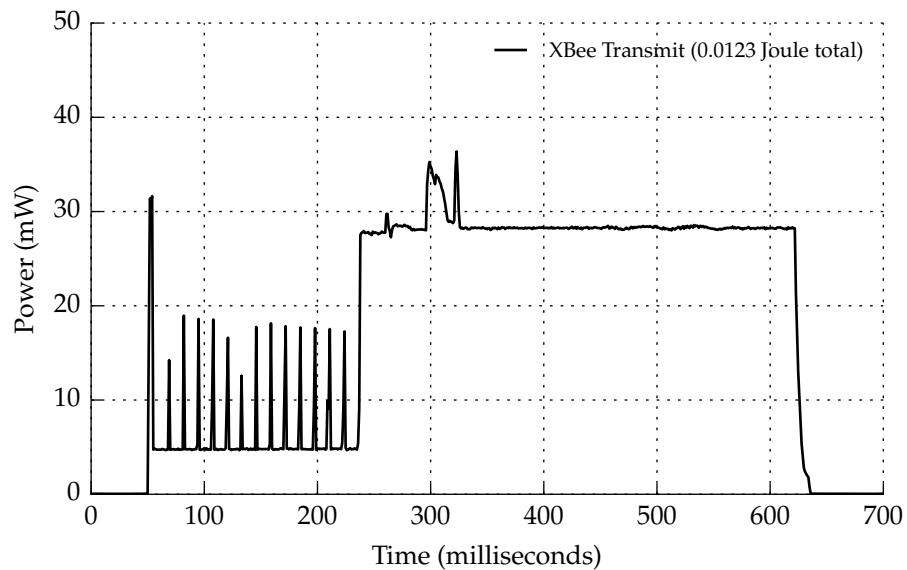


Figure 5.14: Power draw from a Digi International Xbee Series 2 transceiver module.

choice for the electronic water meter. In total the RFM consumed 6.71 mJ and the Xbee consumed 12.3 mJ. Adjusting these figures for the worst case (multiplying by one hundred) gives 671 mJ for the RFM12B and 1.23 J for the Xbee.

5.3 Total Energy Requirements

A crude estimation of an electronic water meter's microprocessor event loop is as follows.

1. Sleep for 1 second
2. Execute 1000 instructions
3. Make 2 analogue conversions
4. Write 2 bytes to non-volatile memory

Mode	Count	Unit	Energy
Sleep	1	seconds	97.4 nJ
Processing	1000	instructions	1.14 µJ
ADC	2	conversions	2.56 nJ
EEPROM	2	bytes	79.0 µJ
		Total (per day)	6.93 J

Table 5.3: Daily energy expenditure of basic processing functionality

Mode	Count	Unit	Energy
Processing	1000000	instructions	1.14 mJ
Transmit	160	bytes	1.23 J
EEPROM	10	bytes	394 µJ
		Total (per day)	4.93 J

Table 5.4: Daily energy expenditure to transmit 160 characters every six hours

This would allow the microprocessor to watch the display of a mechanical water meter and store the readings. This loop would occupy approximately one second, so it will occur 86400 times per day. Every so often the collected data would need to be transmitted, a potentially costly exercise in terms of energy usage. On top of the previously stated event loop is a data transmission loop which would execute every six hours.

1. Execute 1000000 instructions (Data compression)
2. Power up and transmit 160 bytes of using RF transceiver
3. Write 10 bytes to non-volatile memory

Tables 5.3 and 5.4 combine the measurements and estimates from the previous sections with the event loop estimation. They show that approximately 12 J would be consumed per day by an electronic water meter. It was shown in section 4.3 that 280 J of energy is already dissipated in a mechanical water meter per day. This equates to a conversion efficiency of 4.28 %, which would be the minimum efficiency required to run the meter continuously.

Chapter 6

Conclusion

Estimates of energy availability have been made by calculating the amount of energy lost in a traditional water meter. Those estimates showed that for a typical New Zealand household approximately 280J is available for capture every day. In the previous section, the amount of energy that would be needed to run an electronic water meter was estimated to be 12J per day. This means that in order to power an electronic water meter a minimum conversion efficiency of 4.28 % is required. However, calculations from cells assembled in section 3.3 showed that readily obtainable conversion efficiencies are in the order of 0.28 $\mu\%$. Conversion efficiencies over 1 % have not been reported in the literature, and one paper suggests the theoretical maximum is 2 % [52]. For these reasons, the use of streaming cells as a method of energy harvesting from water and current materials is expected to be infeasible. The literature suggests there is room for improvement, to levels which would make streaming cell harvesters practical, but these gains are reliant on new nano-materials.

During the course of this research two issues came to light with regards to streaming cell harvesting. The first issue is a susceptibility to clogging. Having such narrow openings in a domestic water feed is likely to trap

dirt and contaminants at the channel openings. This would lower the effective efficiency and require periodic cleaning, lowering the benefit to utility companies. The second issue is the manufacturing precision that would be required to create the channels. Parts manufactured with high precision are generally small, but a streaming cell would need very precise dimensions with a very large surface area. This may be partly overcome by using such materials as porous glass, but the internal channel dimensions will be less accurate.

This concludes part I. The following section looks at the electrical impedance of medical implant electrodes, which double layers play a large role in. The research here into double layers and the role they play in energy harvesting applications is directly applicable there.

Part III

Double Layers on Conductors: Electrical Impedance

For the engineers of medical implant devices, knowing the electrical impedance between electrodes is important. Having a tool to simulate such impedances allows those designers to ensure fault free operation of potentially lethal devices. A model of the interface impedance between electrode and electrolyte is presented in the proceeding chapter. That model was created by my chief supervisor Jonathan Scott and Peter Single of Saluda Medical Sydney. Validation of the model was made in a standard solution of saline, but details of how saline concentration affected the parameters were unknown. In part II of thesis thesis I take that model and extend its predictive capability to a range of salinities. Having such a model allows for easy comparison between different electrolytes and electrode geometries. Using that ability, I characterise the interface in an anaesthetised sheep's spinal cavity and compare the results to the various saline solutions measured in the lab. That comparison showed that the situation in live sheep is relatively different to that of standard saline solutions. Using the measurement methods developed, I then find a mixture that closely matches the electrical impedance seen in sheep. This mixture now serves as an improved test solution for the engineers of medical implant devices.

Chapter 7

An Interfacial Model In The Electrical Domain

The work throughout the remainder of this thesis is based upon an interface model put forward by my supervisor and a colleague of his, Peter Single. The model was verified in a single, known concentration of phosphate buffered saline (PBS) at the point I began using it. Working through the processes taken by my supervisor to create his model, I re-created the model from my own measurements. By creating a range of solutions of PBS to test against, I fitted parameters of the initial model to the concentration of PBS. This put me in a good position to compare those solutions to live biological solutions. That comparison is the main scientific contribution resulting from this work.

7.1 The Scott-Single Interface Model

Jonathan Scott and Peter Single recently published an electrical model of an implantable electrode array in saline in 2013 [47]. The intention of that model was to simulate the electrical impedance that a medical implant device would see once implanted into a human spinal cavity. It is also

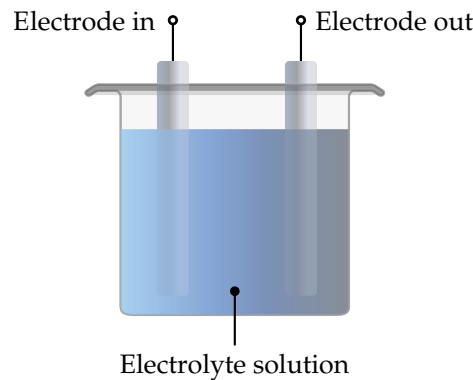


Figure 7.1: Electrodes submerged in an electrolyte solution, such a system can be described by the Scott-Single Interface Model.

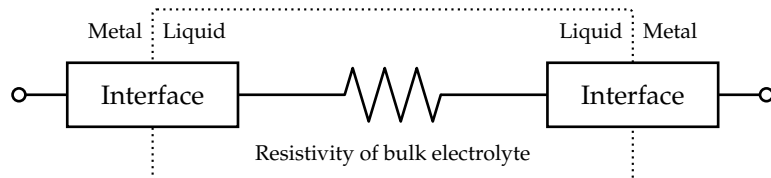


Figure 7.2: Connection diagram of two electrodes (with their interface models) connected together by the resistivity of an electrolyte solution.

general enough to use in any situation where electrodes are placed in an electrolyte solution, such as depicted in fig. 7.1.

The model comes in two parts, the electrode interface, and the resistivity of the electrolyte's bulk. Figure 7.2 shows the general electrical configuration of such an electrode-electrolyte system. It shows that there are two interfaces per system, and that the liquid side of those two interfaces are joined electrically by the resistance of the electrolyte's bulk resistivity. The metal side of the interfaces is what the rest of the circuit would connect to. First, the interface model will be explained.

7.1.1 The interface model

The full interface model is represented schematically by fig. 7.3. It represents the transition between the metal of the electrode and the liquid of the

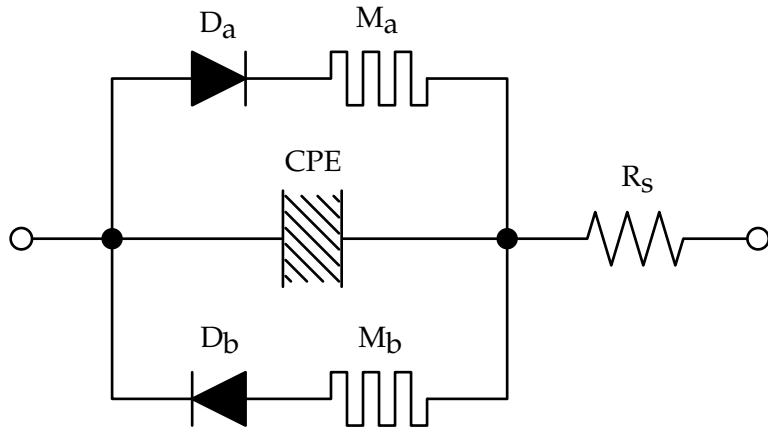


Figure 7.3: Electrical schematic of the electrode-electrolyte interface

electrolyte. The model used throughout this thesis is a slightly simplified version of fig. 7.3 in that the memristors have been removed.

7.1.1.1 Interface series resistance: Resistor

The series resistor at the right hand side of the model schematic (labelled R_S) represents the purely resistive component of the interface's impedance. As it is series with all other components in the interface model, there is no way for charge to cross the interface without encountering this resistance. The parameter used to denote the interface's series resistance is:

- R_S – The series resistance of the interface

7.1.1.2 Polar effects: Constant phase element

At the centre of the model is the constant phase element, or CPE. A CPE, or fractional pole capacitor, is a device that behaves like a cross between a capacitor and a resistor. They are primarily used to describe the capacitance of double layer interfaces, the function it serves in this model. It is capacitive in the sense that voltage leads current, but by an amount less than 90° . Mathematically, the 90° angle between sinusoidal voltages and currents in a

capacitor is a result of the capacitors current being $I(t) = C \times \frac{dV(t)}{dt}$. When $V(t)$ is a sine wave, this becomes $I(t) = C \times \frac{d\sin(t)}{dt}$, which is the same as $I(t) = C \times \cos(t)$. The angle between Sine and Cosine is always 90, and this is why a capacitors impedance is -90° out of phase. A CPE, on the other hand, has a phase angle somewhere *between* 0 and -90° . This requires a fractional differentiation of $I(t) = C \times \frac{dV(t)}{dt}$, something uncommon outside of pure mathematics. A consequence of having a current/voltage relationship of less than 90° , a CPE'S impedance magnitude decays at a rate lower than $20 \frac{dB}{decade}$.

SPICE, or any other commonly used circuit simulators, does not support fractional pole capacitors so entering one into the model will require building it up from discrete components. In 1959, Morrison demonstrated a

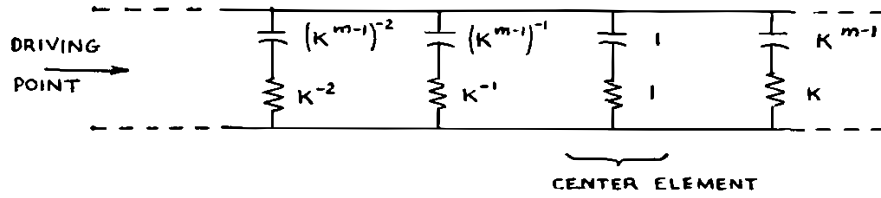


Figure 7.4: Ralph Morrison's implementation of a constant phase element using an infinite array of resistor-capacitor pairs (taken from Morrison's paper – [38]).

way of creating constant phase elements from an infinite array of resistor-capacitor (RC) pairs [38]. One of Morrison's implementations of a constant phase element is presented as fig. 7.4. Each parallel branch has precisely chosen resistor and capacitor values such that when summed together the impedance magnitude versus frequency is a constant slope, i.e., the impedance does not flatten at a particular frequency as it would with a single RC pair. Creating any element comprised of an infinite number of sub-elements is not possible, but by selecting only those elements that contribute to the bandwidth of interest the result is the same within the selected

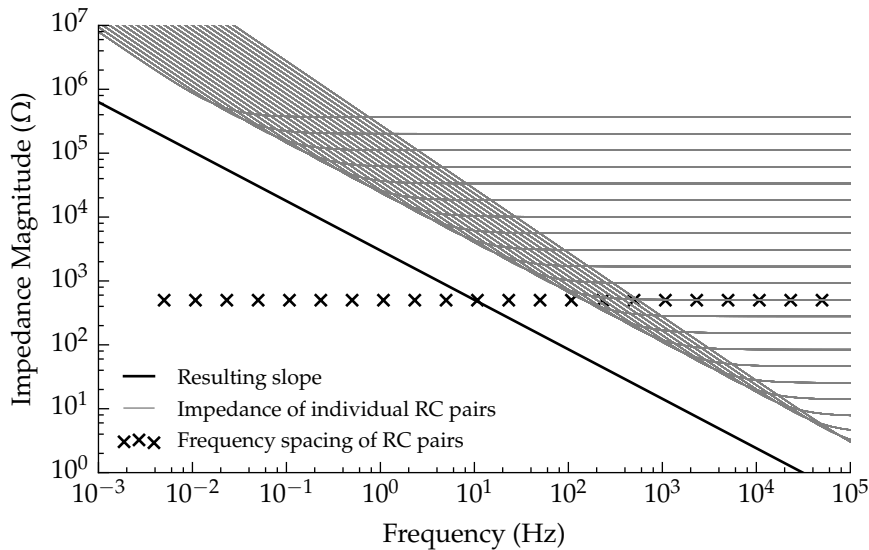


Figure 7.5: Graph showing how a non 20 dB per frequency decade

frequency window. Using that method and selecting only RC pairs with a cut-off frequency in the range of 1 mHz to 1 MHz, a practical CPE element is created.

Figure 7.5 shows the individual contributions from each RC branch in an implementation of a CPE. Each of grey trace represents a single RC branch in the CPE element, each displaying a high-pass filter slope. The value of the resistor in each branch is evident by the vertical spacing of the traces, clearly visible to the right of the graph. The branches in this particular example have been spaced in the frequency domain at a density of three per decade, as shown by the black crosses. This means that per decade of frequency, there are three corner frequencies, each relating to an RC pair. Because each of these branches are in parallel the total response of the CPE is the sum of each branch, that response is shown as the black trace on the graph. The critical observation is that the slope of the resulting trace is not the same as each of the individual branches. This allows the CPE to behave

fractionally as a capacitor, being anywhere between resistive (flat response) and capacitive (20 dB/decade slope).

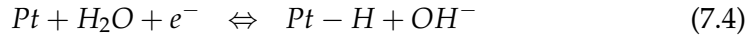
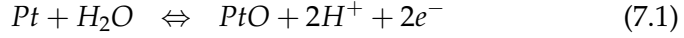
The CPE is represents readily reversible reactions, polar reorientation, and ionic repulsion and attraction between the electrode surface and electrolyte. It is capacitive in nature because each of these mechanisms store charge, which can be drawn back by reversing the applied electromotive force. Parameters used to describe the behaviour of the CPE are:

- m – Slope of the CPE's frequency response
- k – Spacing, or density, of R-C branches with frequency
- $|Z| @ 1 \text{ kHz}$ – Sets the vertical position of the magnitude of CPE's frequency response at a known frequency

7.1.1.3 Faradaic reactions: diodes

If the voltage placed across the interface is kept within certain limits, the CPE and series resistance (R_S) would be all that is necessary to accurately mimic a single electrode-electrolyte interface. But once the electric potential across the interface becomes high enough, Faradaic reactions will occur at the electrode's surface. Faradaic reactions are reactions involving charge transfer, adding ionised species to the electrolyte and often producing gas. Gas, or any new species, is bad news in an implanted setting as this causes damage to the patient. Possible faradaic reactions between saline and plat-

inum electrodes are:



The electrical current density through an electrode as a function of electrode overpotential and the cathodic and anodic reactions occurring at each electrode is given by:

$$i_{net} = i_0 \left\{ \frac{[O]_{(0,t)}}{[O]_\infty} e^{-\alpha_c n f \eta} - \frac{[R]_{(0,t)}}{[R]_\infty} e^{(1-\alpha_c) n f \eta} \right\} \quad (7.5)$$

This is the current-overpotential equation and is derived from the more general Butler-Volmer equation [34, 47]. In eq. (7.5), i_{net} is the net Faradaic current across the electrode/electrolyte interface, i_0 is the exchange current density, $[O]_{(0,t)}$ and $[R]_{(0,t)}$ are the concentrations at the electrode surface as a function of time, $[O]_\infty$ and $[R]_\infty$ are concentrations of reactant in the bulk electrolyte, α_c is the cathodic transfer coefficient (approximately 0.5), n is the number of moles of electrons per mole of reactant oxidised, f is Faraday's constant divided by the product of the gas constant and the absolute temperature (F/RT), and η is the electrode overpotential. This equation describes the forward and reverse electrical current through an electrode by separating the forward and reverse reactions; oxidisation and reduction.

$$I = i_0 e^{V_D/nV_T} \quad (7.6)$$

Taking a single half of the equation, either the reduction or oxidisation,

yields an equation that is similar to that of a diode; an observation made by McAdams and utilised in the Scott-Single model [33]. The standard diode equation is shown as eq. (7.6), where I is the current through the diode, i_0 is the diode saturation current, V_D is the potential across the diode, n is the diode's ideality factor, V_T is the thermal voltage (defined as the product of Boltzmann's constant and temperature divided by the charge on an electron). The parameters used to describe the behaviour of the diode are:

- i_0 – the diode's saturation current
- n – the diode's ideality factor

The diodes themselves can not account for the relative abundance of reactants for the redox reactions, this must be taken care of separately.

7.1.1.4 Species depletion: memristors

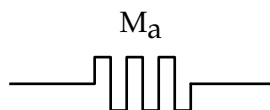


Figure 7.6: Electrical symbol of a memristor, as is used in the original electrode-electrolyte interface model

A memristor is a two port device that sets its resistance based on its own history. Its resistance can either depend on the integral over time of the voltage placed across it or the total charge passed through the device [29]. Its name is a portmanteau of the word 'memory' and 'resistor' owing to its use of memory to set its resistance.

The memristive device models species depletion in the electrolyte by pinching off a diode branch with the amount of current passed through the diode. As the specific Faradaic reaction proceeds, it consumes the reactants from the electrolyte bulk until eventually there is none left. Increasing the

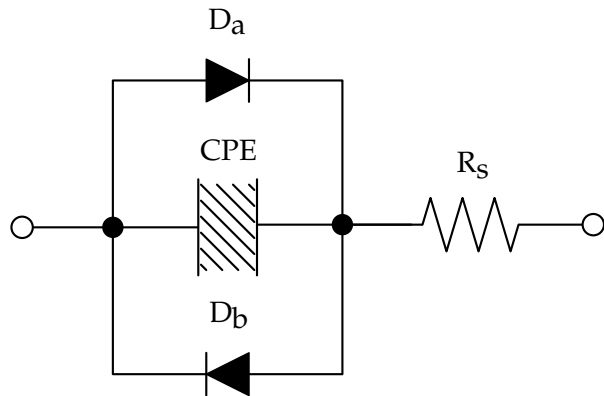


Figure 7.7: Electrical schematic of the electrode-electrolyte interface without memristors (as used throughout this thesis)

resistance in series with a conducting diode has the effect of removing that diodes current path from the circuit, simulating the depletion of reactants for the modelled reaction.

Memristors were removed from the model used in this thesis as they added complexity that would yield very little value. The diodes are only used to model the *onset* of Faradaic conduction, which is the most relevant parameter of the Faradaic modelling. Once these reactions begin, the electrode overpotential has been pushed too far and there is little to be gained from knowing how far the reaction can be run until the reactants have been depleted. In an implanted setting it is likely that the electrolyte will circulate throughout the body, bringing new reactants to the electrode's surface over time. Species depletion is likely to be a slow process, dependant on the electrolyte volume and species concentration.

Figure 7.7 shows the actual interface model used throughout the remainder of this thesis. Although it is slightly different to the Scott-Single interface model, the other parameters are unaffected by the removal of these elements. Each of the components of the interface model have now been described. A model of the interface on its own is of little value as there will always be two

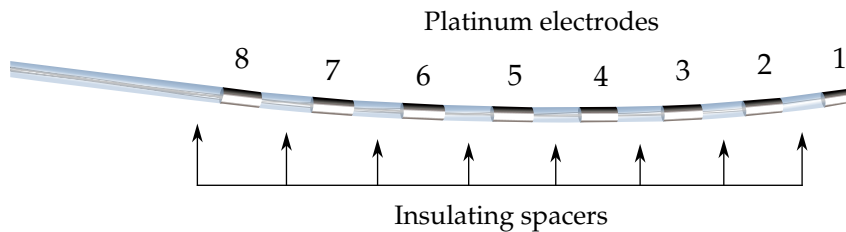


Figure 7.8: St. Jude Medical Octrode. An eight electrode array commonly used in spinal stimulation implants. The electrode numbering shown here will be used throughout this work.

interface models and those models will be separated by the electrolyte itself.

7.1.2 Inter-electrode resistivity

Modelling the resistance between two electrodes in a fixed geometry situation is simply a matter of inserting an appropriately sized resistor between the two interfaces. The resistance is dependant on the electrolyte's conductivity, the combined surface area of the two electrodes and the distance between them. Modelling an electrode array, such as the St. Jude Medical - Octrode, is more complex as it requires a resistor network to describe the inter-electrode resistances. An illustration of an Octrode is presented as fig. 7.8.

Scott and Single create resistor network for modelling the electrolyte conductivity based on the geometry of the electrodes and the resistivity of the electrolyte. By sectioning the surrounding liquid into cylindrical volumes they calculate the equivalent resistance between those volumes both radial and longitudinal directions. The radii of the volumes double at each layer which correspond to a fixed radial resistance between each layer. There are two different radial resistances, one for the rings expanding from the insulating spacers, and one for those expanding from the electrode cylinders. The two alternate due to each electrode being separated by an

insulating spacer. The longitudinal resistances quarter in size with each ring layer and after the last radial resistor each node is shorted together. The full mesh for the eight electrode array is five layers deep with three rows of padding at each terminating end, totalling two hundred and five resistors in total. Figure 7.9 shows the resistor network schematic. Further details of how the mesh geometry and resistor values were calculated can be found in [48].

The parameters that describe the resistor mesh are:

- R_{eri} - The initial resistance placed radially from an electrode.
- R_{sri} - The initial resistance placed radially from a spacer.
- R_{li} - The longitudinal resistance.
- Depth - Number of layers between the electrode/spacer and the common end node in the ladder
- Padding - Number of spacer layers to be added to the before the first electrode and after the last electrode in the network.

7.2 Electrolyte: Phosphate Buffered Saline

The model has been fitted to phosphate buffered saline (PBS) because it is was closest representation of human spinal fluid known at the time. Engineers at Saluda used a concentration one-tenth that of a standard solution of PBS as a test solution for their spinal implants as they believed it to be a good match. I was not understood how well the one-tenth concentration matched spinal fluid electrically, which is one of the first research questions I set out to answer. The ingredients used to make the stock standard PBS

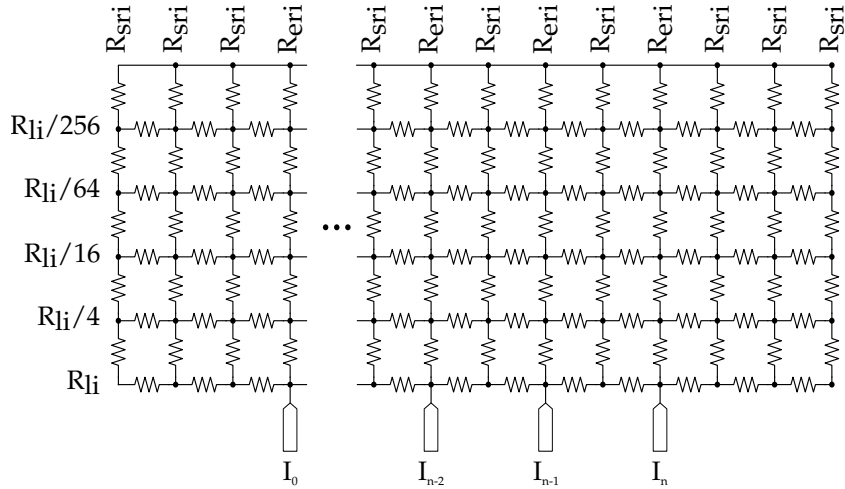


Figure 7.9: Resistor mesh used to model the electrical resistance between interface pairs. R_{li} is longitudinal resistance, R_{srri} and R_{eri} is the radial resistance for the spacers and electrodes respectively, and I is an interface.

Ingredient	Quantity	Unit
H_2O	1000	ml
NaCl	8.00	g
KCl	0.20	g
Na_2HPO_4	1.44	g
KH_2PO_4	0.24	g

Table 7.1: Ingredients used to produce one litre of stock solution of phosphate buffered saline.

concentration solution are given in table 7.1 and the procedure for creating the full strength stock are as follows.

1. Weigh out day ingredients and combine in stock bottle.
2. 800 ml of distilled water is added to bottle and solution is stirred until all solids have dissolved.
3. pH is measured and adjusted to 7.4 by addition of HCL.
4. The stock solution was mixed up to the target volume of 1000 ml.

Six bottles of ranging in concentration from full strength (1.0X) to one-fortieth (0.025X) were then made from the stock solution. Table 7.2 shows

Stock (ml)	Water (ml)	Final Concentration
700.0	0.0	1.00X
350.0	350.0	0.50X
175.0	525.0	0.25X
70.0	630.0	0.10X
35.0	665.0	0.05X
17.5	682.5	0.025X

Table 7.2: Final dilutions of stock to create six 700 ml solutions ranging from 0.025X to 1X standard PBS concentration.

the volumetric dilution used to create the six concentrations of PBS that are then used to fit the model parameters to.

7.3 Methods Of Parameter Extraction

The model has a number of parameters that are used to set the behaviour of each of the components. Finding suitable values for each of the parameters is critical in ensuring that the final model offers a good representation of the electrode-electrolyte system. The trick to finding suitable parameter values lies in selecting useful measurements of each part of the model, usually by isolating the measurement as much as possible from other model elements. The following sections describe the measurements used to determine parameters used in the final model. Ideally each element in the model would be measured separately, but in some cases it is not possible to totally isolate two areas. Scott and Single found a set of parameters that described the Octrode in a one-tenth concentration solution of phosphate buffered saline (PBS). In this section I create six different solutions of PBS ranging in concentration from 1.0x to 0.025x the concentration of a standard PBS solution. I extend the Scott-Single model to work over a range of concentrations of PBS by adding another parameter to the model - PBS concentration.

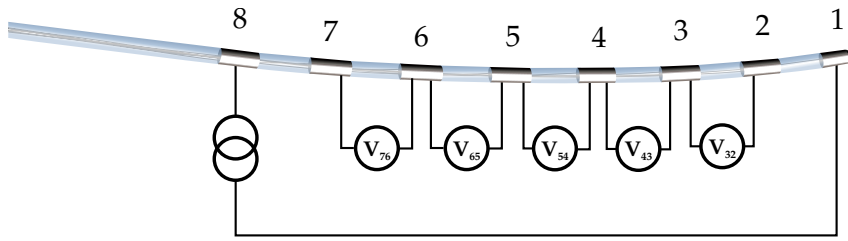


Figure 7.10: Measurement schematic of trans-impedance measurements where electrodes eight and one are driven and the remainder are used in voltage differential measurements.

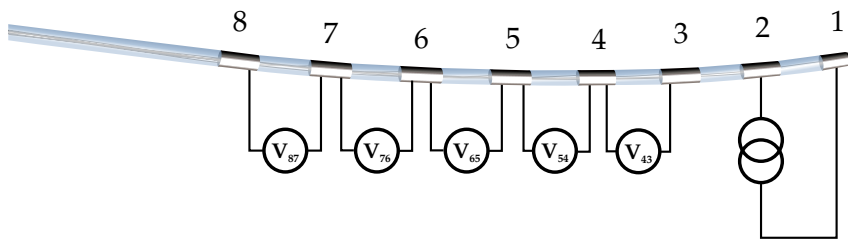


Figure 7.11: Measurement schematic of trans-impedance measurements where electrodes two and one are driven and the remainder are used in voltage differential measurements.

7.3.1 Resistivity

In order to find the parameters of any elements within the electrode-electrolyte interface it is first necessary to find the inter-electrode resistances. This is because elements of the model can not be measured in isolation since the resistivity of the electrolyte solution will always present itself between a measurement apparatus and the element of interest. I start by determining the resistances used in the resistor mesh using the same method as was used by Scott and Single [48]. Once those resistances are accounted for, the behaviour of components in the interface can be calculated from measurements that included those inter-electrode resistances by subtraction.

Scott and Single measure trans-impedance between pairs of electrodes in two different configurations where a defined AC current is driven between a pair of electrodes. Data from these measurements is tabulated so each

Parameter	Determined from:
R_{eri}	optimised fit via SPICE simulation
R_{sri}	optimised fit via SPICE simulation
R_{li}	optimised fit via SPICE simulation
Padding	previous value of 3 rows used (from Scott & Single)
Depth	previous value of 5 layers used (from Scott & Single)

Table 7.3: Parameters determined by an optimised fit between a simulated mesh and transimpedance measurements.

row contains the AC current forced between the two stimulus electrodes and a voltage measured between a pair of non-driven electrodes. By measuring the voltage across pairs of non-driven electrodes using a suitably high impedance measurement, those measurements will correspond to the voltage difference in the electrolyte. For this method to work it is assumed that the current passing through each non-driven interface is zero, and therefore no voltage is dropped between the electrode's metal and the electrolyte solution at the electrode's surface. This means that voltage differentials can only be measured on the non-driven electrodes. Figures 7.10 and 7.11 show the two measurement configurations used to collect transimpedance data. Those transimpedance results are recreated using a simulated mesh of resistors with fitted values to the three resistor parameters. An optimisation routine can be used to find the three values that create a mesh that matches the measured values as close as possible, as summarised in table 7.3.

7.3.2 Constant phase element and series resistance

By accounting for the value of resistance seen between electrodes it is now possible to probe deeper into the interface model. Calculation of both the CPE and the series resistance (R_S) is made via impedance spectroscopy. It is possible to use the applied frequency to separate the response of the CPE

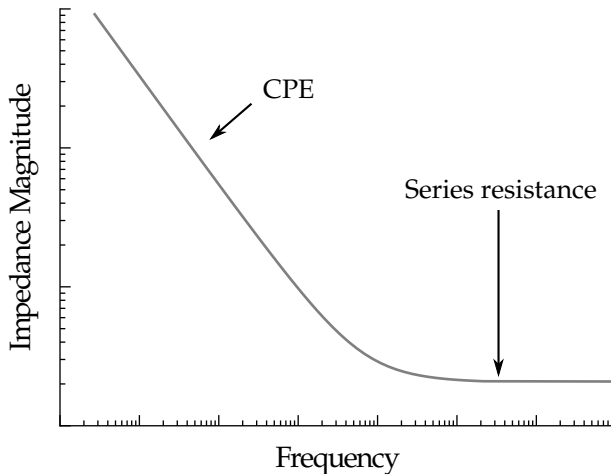


Figure 7.12: Log-log plot of frequency vs impedance magnitude of a single interface and inter-electrode impedance. The response of the CPE and that of the total series resistance is separated in the frequency domain.

from that of the series resistance of a single interface and inter-electrode resistance. The impedance of the CPE dominates below 10 Hz, where its slope and magnitude can be determined. At higher frequencies, greater than 1 kHz, the series resistance of both the interface (R_S) and the previously determined inter-electrode resistance is evident. This separation of responses is illustrated in fig. 7.12. Subtracting the inter-electrode resistance (determined previously) from the resistive element yields just the interface's series resistance (R_S). Parameters for the CPE, such as slope and vertical position, are then read off the low frequency part of the trace where the slope is not disturbed by the resistive part. These parameters are summarised in table 7.4.

7.3.3 Faradaic currents

Measurement of Faradaic current requires pushing the electrode overpotential until reactions at the electrode's surface begin. Electrical currents involved with Faradaic conduction increase exponentially with increasing

Parameter	Determined from:
k	previous value of 3 branches used (from Scott & Single)
m	slope of $ Z $ vs. frequency response
$ Z @ 1 \text{ Hz}$	impedance magnitude at 1 Hz
R_s	impedance at high frequency (10 kHz) end of the trace

Table 7.4: Parameters determined from impedance spectroscopy measurements of electrode-electrolyte interface.

electrode overpotential. Scott and Single used a triangular voltage stimulus to identify the onset of Faradaic conduction at the interface. The triangular wave is equivalent to a constant ramp-up and ramp-down of voltage placed across the interface. It was mentioned earlier that current flowing into a capacitor is given by: $I(t) = C \times \frac{dV(t)}{dt}$. When $\frac{dV(t)}{dt}$ is a constant, as is the case for any constant ramp-up or ramp-down voltage stimulus, the current becomes a constant. It is assumed that the fractional differentiation of the current equation will still yield a relatively constant current in light of the capacitor being a CPE. By slowly ramping the electrode overpotential up the current should be constant up to a point where it becomes exponential. The voltage corresponding to the point at which the current draw becomes exponential will be used to determine the onset of Faradaic conduction. That point, together with the rate of growth, would then be used to fit values for i_0 and n , the diode's saturation current and ideality factor respectively, as summarised in table 7.5. Problems arose with those measurements, which will be discussed in the following section, that show the behaviour of the CPE was less predictable than expected.

Parameter	Description
i_0	optimised fit of threshold voltage to measured curve
n	optimised fit of growth rate to measured curve

Table 7.5: Parameters determined from fitting diode parameters to measured response of Faradaic current.

Chapter 8

Interface Parameters

Details of components in the electrode-electrolyte interface model and methods of determining its parameters have been discussed. Research effort will now move to measuring and fitting suitable parameter values to the model. Model parameters are determined for various concentrations of phosphate buffered saline (PBS), and then for comparison – in a living sheep's spinal cavity. The comparison will show whether a one-tenth concentration of PBS is in-fact a good substitute for cerebrospinal fluid (CSF), which it is assumed to be by medical implant engineers.

8.1 Phosphate Buffered Saline

Scott & Single fitted parameters of their model to a one-tenth concentration (0.1X) of a standard solution of PBS; a buffered saline solution [48]. I measure and fit parameters not only to the one-tenth concentration, but to six concentrations spanning 0.025X to 1X the concentration of a standard buffered saline solution. For the model parameters that change with salinity, a fit is made using regression analysis to PBS concentration. Doing this gives a model that can be used to predict the impedance response of an electrode array submerged in a wider range of concentrations of saline solutions.

Concentration
1.00X
0.5X
0.25X
0.1X
0.05X
0.025X

Table 8.1: Six PBS concentrations used to fit model parameters to.

Each of the PBS measurements were made in 1000 ml glass bottles containing 700 ml of the PBS solution to be measured. Measurements were made in a temperature controlled environment set at 21° Celsius. All measurements were automated by the use of Python scripts running on a GNU/Linux based workstation. The scripts communicate with the instruments both to configure measurements and collect data. Each measurement set was repeated for each of the six solutions used. The six concentration of PBS that were measured are shown in table 8.1.

8.1.1 Resistor Mesh

With the electrode array immersed in a saline solution, a 10 kHz sinusoidal current having a peak amplitude of 500 μ A was passed through the stimulus electrodes using an Agilent 33220A function generator. A shunt resistor inserted in series with the function generator allows measurement of current between electrodes. The differential voltage across a pair of non-stimulating electrodes and the voltage across the shunt resistor was measured using a Tektronix TPS 2024 oscilloscope. Figure 8.1 shows the measurement configuration used when electrodes one and eight are used as the stimulus electrodes. The second configuration has electrodes eight and seven as stimulus electrodes and the remaining electrode pairs are used to measure transimpedance voltage differentials.

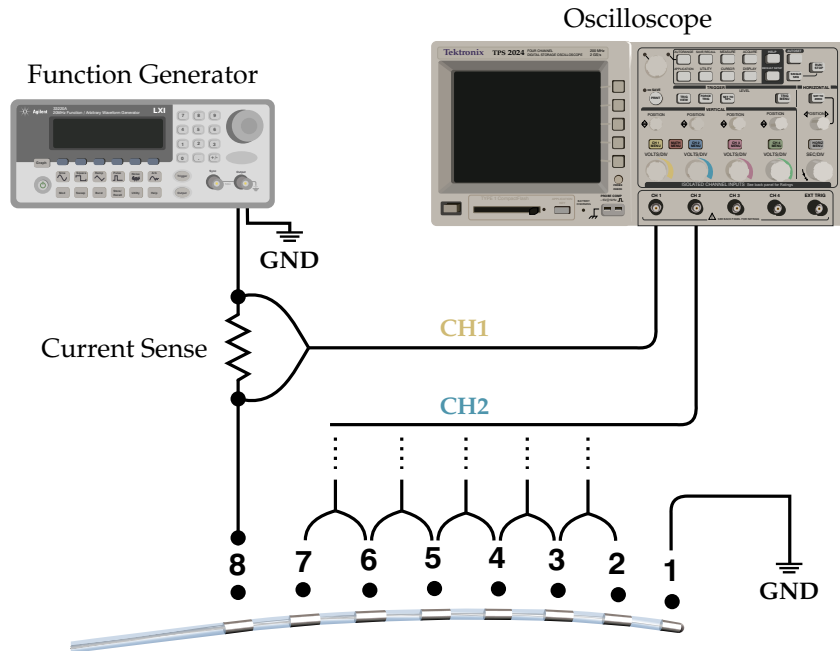


Figure 8.1: Illustration of one of two measurement configurations used to measure the electrode transimpedances. Each of the electrode pairs were measured one-after-the-other using the shown equipment.

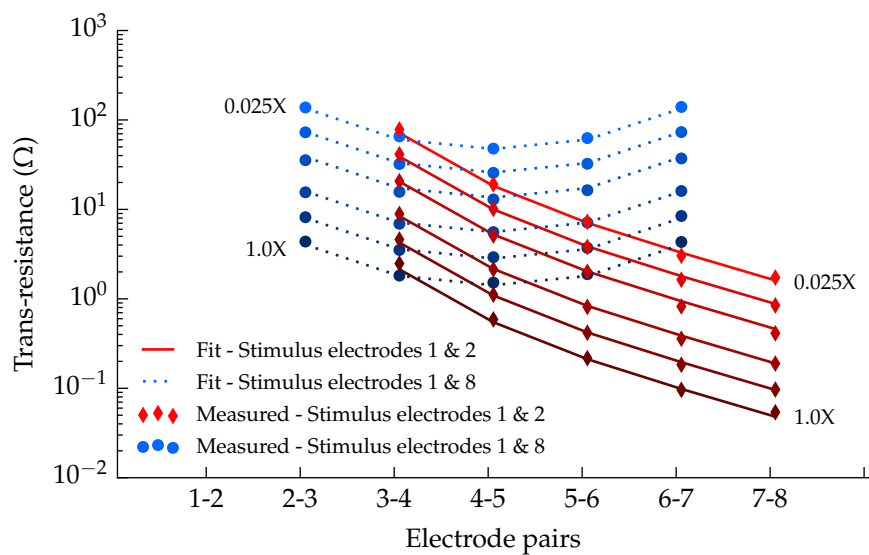


Figure 8.2: Measured and fitted values of trans-impedance for both measurement configurations. Voltage measurements are made between adjacent pairs of electrodes as current is pushed through the stimulus electrodes.

Parameter	Value
R_{eri} (Ω)	$0.407 / \sigma$
R_{sri} (Ω)	$R_{eri} \cdot 3/4$
R_{li} (Ω)	$3.71 / \sigma$
Depth (layers)	5
Padding (layers)	3

Table 8.2: Resistor mesh parameters for the electrode array in various concentrations of PBS. Electrolyte conductivity (σ) is expressed in units of S/cm .

The results of those measurements, in both configurations, are represented as markers in fig. 8.2. Each point is calculated by taking the voltage differential across a pair of electrodes (V_{diff}) and dividing by the stimulus current. Remember, the stimulus current was set to be around $500\ \mu A$ peak.

Values for R_{eri} and R_{li} were determined using a Python optimisation script for each concentration of PBS. The optimisation script selects candidate values for R_{eri} and R_{li} , simulates the mesh using those values, and then calculates the equivalent trans-impedance values. The error between simulated trans-impedance values and measured values is calculated and the process repeats, selecting different values of R_{eri} and R_{li} to improve the fit. The final values of R_{eri} and R_{li} are those that minimise the error, they are shown in table 8.2. R_{sri} is a dependent variable, so is expressed in terms of R_{eri} , and the remaining parameters have been re-used from the work of Scott & Single. Figure 8.2 shows measurement results for each pair of non-stimulated pair of electrodes along with simulated results using the fitted parameters.

8.1.2 Series Resistance And Constant Phase Element

Measurement of both the CPE and the interface's series resistance is made using an impedance spectroscopy method. These measurements are made by passing a sinusoidal current between electrodes two and seven of the

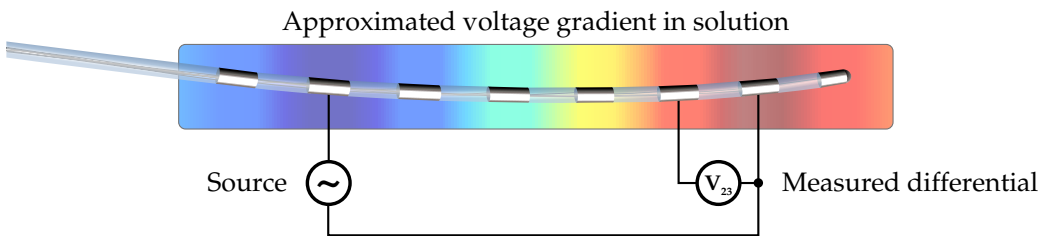


Figure 8.3: Illustrated voltage gradient in electrolyte solution at each electrode's surface when potential is applied across electrodes two and seven. Measurement of electrolyte voltage taken between electrodes 2 and 3.

electrode array. Use of the end electrodes (one and eight) was avoided as a precaution to reduce end effects resulting from the electrode's geometry. The sinusoidal voltage at the liquid side of the interface is taken as the the voltage that appears at an adjacent electrode (electrode three) when a suitably high impedance measurement is made, this is illustrated in fig. 8.3. This measurement relies on the ability to make high impedance voltage measurements to minimise voltage drop across the electrode interface, for which the Tektronix TPS 2024 four channel oscilloscope was used again. This oscilloscope has floating channels, each having an input resistance of $10\text{ M}\Omega$ when using $10X$ probes. The Agilent 33220A function generator was used again to generate the stimulus waveforms applied between electrodes two and eight. A current sense resistor of $10\text{ k}\Omega$ was inserted in series with the waveform generator's output and was measured by the oscilloscope. By measuring the current through electrode two and the voltage across the interface (measured between electrode two and three), the impedance of the interface is calculated. A diagram of the measurement setup is shown as fig. 8.4. For each of the six solutions, twenty frequencies (log-spaced) were sampled between 50 mHz and 10 kHz for the impedance measurements. At each frequency the stimulus waveform amplitude was re-adjusted to be 300 mV-peak as the interface's impedance changed. Figures 8.5 and 8.6

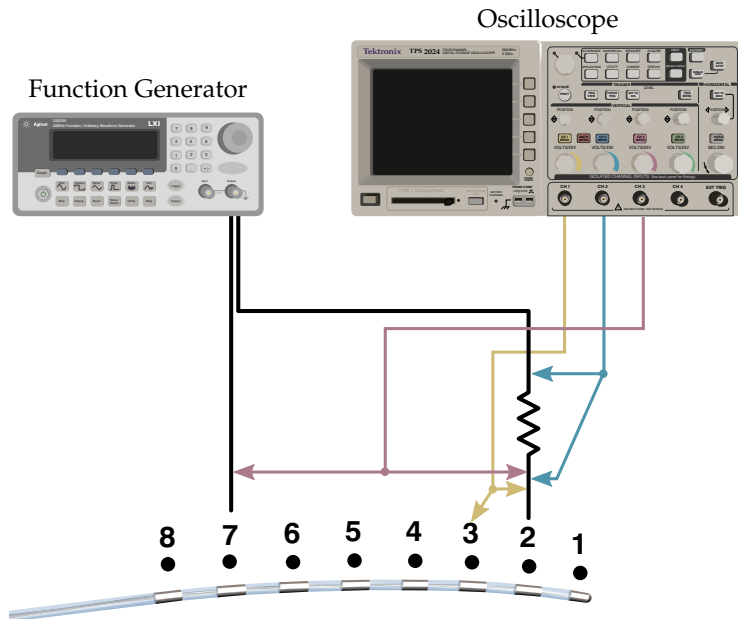


Figure 8.4: Diagram showing the measurement configuration used to measure the CPE response and interface series resistance.

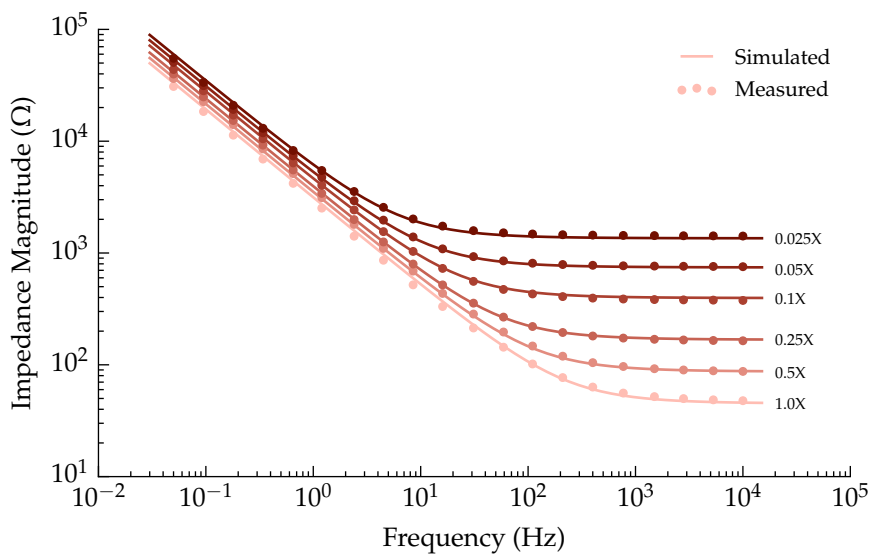


Figure 8.5: Impedance magnitude of both the measured interface response and the fitted response at each of the six concentrations of PBS.

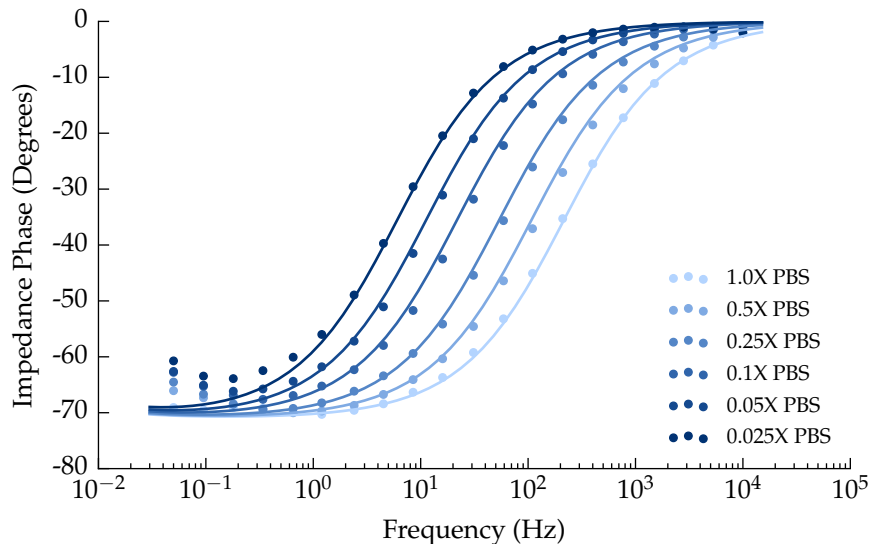


Figure 8.6: Impedance phase of both the measured interface response and the fitted response at each of the six concentrations of PBS.

show the calculated impedance magnitude and phase from measurements as markers and simulation results of the fitted parameters as traces. Figure 8.7 shows the SPICE model used to simulate parameter values for the CPE and R_s . Final values were found by minimising the difference between the simulated response and the measured response using a Python script. For each set of parameter values in the optimisation the script builds a SPICE circuit using those parameter values, simulates the circuit, calculates the interface impedance and compares the values to the measured results. The process is automated and runs until a minimum error between simulated and measured results is found. Once found, the script exists and displays the final values of each parameter. After parameter values are found for each concentration of PBS, another optimisation is made to scale relevant parameters by the concentration. The parameters that are scaled with concentration are the series resistance (R_s) and the CPE's impedance magnitude at 50 mHz. The final fit expresses these parameters as functions dependent

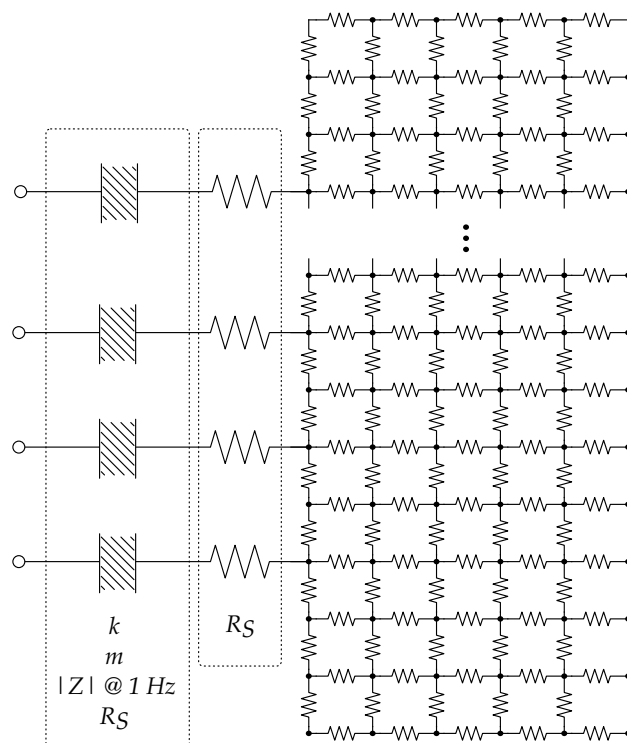


Figure 8.7: The SPICE model schematic used to find optimum values for parameters of the CPE and interface series resistance. Parameters for the resistor mesh are those determined previously.

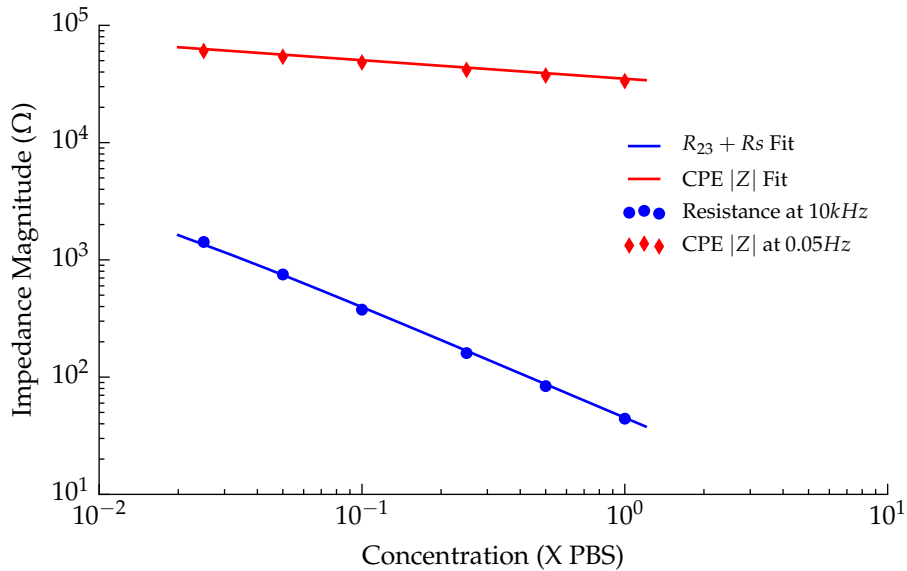


Figure 8.8: Plot showing fitted parameter values for the CPE impedance magnitude at 50 mHz and series resistance at each of the six concentrations of PBS (shown as markers). The solid trace shows the resulting fit between those values as a function of concentration.

on PBS concentration (salinity). Individual parameter values for each concentration, along with the resulting fit, is shown in fig. 8.8. Measurements of the CPE's vertical position were made at 50 mHz, as opposed to the parameters defined value at 1 Hz, to avoid any effect from the series resistance interfering with the measured value. As the slope of the CPE is always the same, the value can be easily converted back to the equivalent value at 1 Hz. Measured resistance at high frequency includes the inter-electrode resistance (R_{23}) which has been included in the plot, but will be subtracted to leave only R_S . The final parameters for the CPE and R_S are given in table 8.3.

Parameter	Value
m	1.34
k	1.773
$ Z @ 1 \text{ Hz} (\Omega)$	$3284 \times \text{concentration}^{-0.158}$
$R_s (\Omega)$	$13.38 \times \text{concentration}^{-0.8397}$

Table 8.3: CPE and R_s parameters. Concentration is relative to the stock solution of phosphate buffered saline.

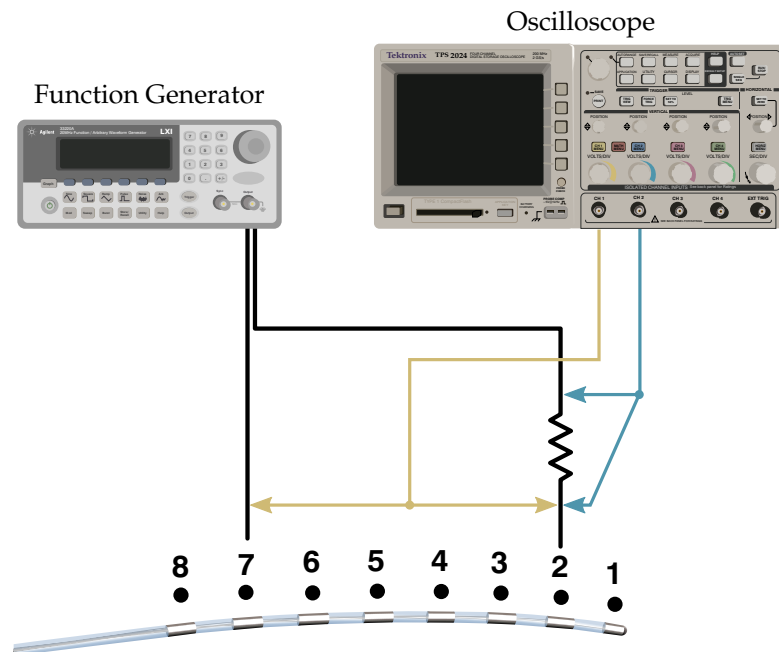


Figure 8.9: Illustration of the cyclic voltammetry measurement configuration used to measure the response of the interface when driven into Faradaic conduction mode.

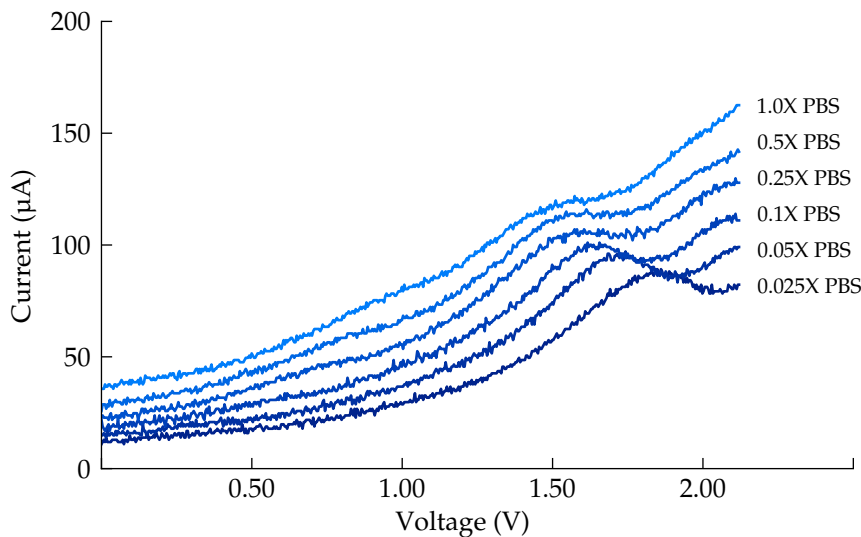


Figure 8.10: Graph showing measured Faradaic response of each concentration of PBS to a linearly increasing voltage between electrodes two and seven.

8.1.3 Faradaic Current

Using the same oscilloscope and function generator as the previous measurement, the oscilloscope is set to measure voltage between electrodes two and seven and the current through the current sense resistor. The function generator is set to produce a triangle wave stimulus, or linear ramp, also between electrodes two and seven. Electrical current associated with Faradaic reactions rises exponentially after a threshold electrode overpotential. The point at which the electrical current draw begins to move exponentially with increasing voltage represents the onset of the associated reaction.

Figure 8.10 shows measured data where the Faradaic response is evident for each concentration. The repeatability of these measurements was low although care was taken to recreate the same conditions for each run. To try and improve the repeatability the following was tried:

- Maintaining a constant ambient temperature

- Cleaning the electrodes between each measurement using isopropyl alcohol
- Keeping the electrolyte moving at a constant velocity using a motorised stirrer
- Letting the system to settle for periods up to two hours between measurements

These steps reduced variation between measurements, but by no means removed the variation. Sweeping the voltage at 0.12 V s^{-1} was slow enough that results did not appear to be too distorted but fast enough that a measurement run could be completed quickly. Completing measurements quickly seemed important at the time as it was often the case that an artifact would show up during a measurement run, for what seemed like no apparent reason, and affect the remainder of the experiments. Artifacts were sometimes a peak at a certain voltage, otherwise they would manifest themselves as distortions to the current/voltage trace. A key insight was realising that after the voltage across a pair of electrodes had been pushed into Faradaic region they then began to behave differently, even after being returned to lower stimulus voltages. In fig. 8.10 it is clear that each concentration has a different Faradaic response. This means that when the maximum voltage is applied to each of the solutions that the highest concentration is driven further into its Faradaic region than the rest. That in turn would create an artifact that would appear on the remaining traces (those of lower concentration), that would not have otherwise been there. The issue of artifact and dependence on sweep rate led me to find other ways of measuring Faradaic currents.

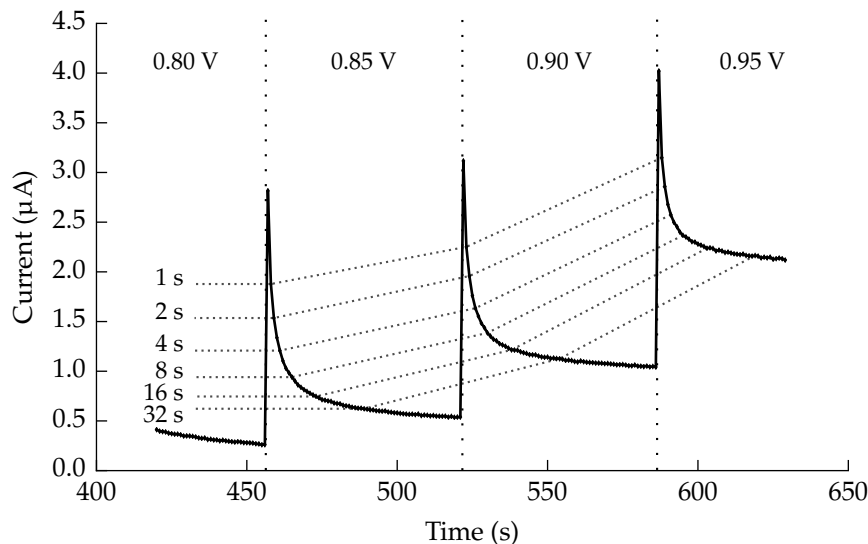


Figure 8.11: Graph showing measured response of two interfaces to a multiple step responses. Vertical dotted lines indicate when in time the step occurred. Dotted traces show points in time after each response. Measurements are between electrodes two and seven on the Octrode submerged in 1X PBS.

8.1.3.1 Step based Faradaic measurements

A revealing measurement came from the use of the Agilent E5270B precision measurement mainframe, the same instrument that was used to measure the streaming potential cells of part I. By increasing the voltage between the electrodes in discrete steps and recording the current over time it became clear that the CPE was having a large effect on the Faradaic measurements. Figure 8.11 shows three transitions in steps of 50 mV occurring 64 s apart. The dotted traces show what the result would be if the measurement were taken at that time, i.e. the trace would take the shape of the dotted line of the corresponding delay time. This graph shows the effect the CPE is having on measurement results, as well as the duration of time necessary for the transient response to settle in most instances.

Subsequent measurements of CPE settling time show that a delay of

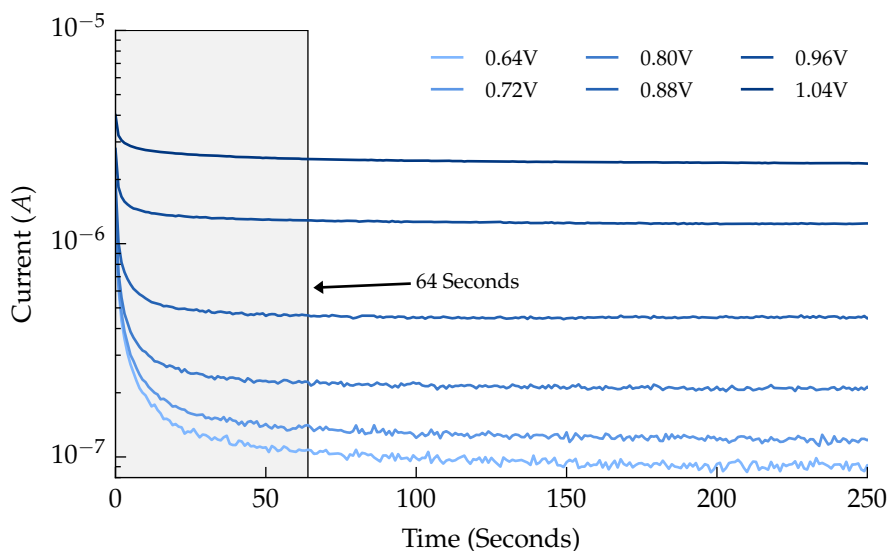


Figure 8.12: Graph showing CPE discharge curve after a step transition between each of voltage trace in increasing order. Measurements are between electrodes two and seven on the Octrode submerged in 1X PBS. A delay of 10 000 seconds elapsed between each step.

64 s between steps is adequate to allow the CPE voltage to settle. These measurements are shown as fig. 8.12, with the 64 s window highlighted in grey. It is interesting to note from these measurements that the capacitance appears to be a function of the applied overpotential, with lower potentials resulting in larger capacitance.

Figure 8.13 shows measurements of four concentrations of PBS overlaid on top of one another. This graph reveals that not only does the capacitance vary with applied voltage, as was shown in fig. 8.12, but also with concentration of PBS. A consequence of this is that not waiting long enough to sample the current gives the impression that a higher concentration of PBS results in larger Faradaic currents. This is shown by the dotted trace that is sampled 10 s after each step, which I believe is representative of results obtained using cyclic voltammetry methods. Importantly – the settled current draw for each concentration is the same. Any separation between concentrations

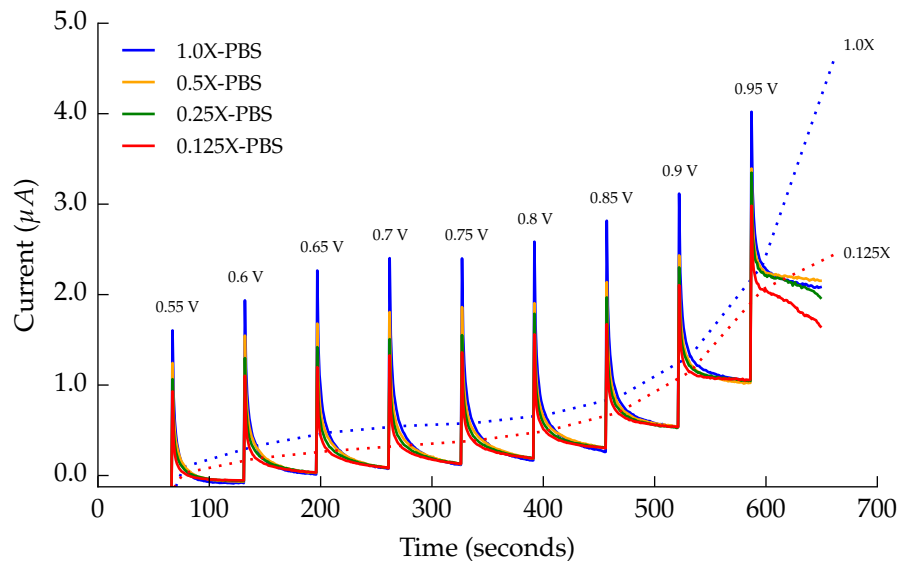


Figure 8.13: Graph showing measurements of four concentrations of PBS as each is stepped from 0.55 V to 0.95 V. Measurements are between electrodes two and seven on the Octrode. A delay of 64 seconds elapsed between each step. Dotted traces connect current measurements taken 10 s after each step.

at the sixty-four second mark for each step appear to be completely random.

8.1.3.2 Successful measurement of the Faradaic currents

Figure 8.14 shows the collected measurements of the electrical current due to Faradaic reactions using the stepped measurement method. Spread in the measurements at low voltages is due to noise in the measurement samples. There are three important observations that can be made from this graph:

1. The effect saline concentration below 0.9 V has little to no significance on the Faradaic current draw.
2. Saline concentration is directly related to Faradaic current draw above 1.05 V.
3. Between 0.9 V and 1.05 V each trace transitions to a mode of saline concentration dependence in reverse order of saline concentration.

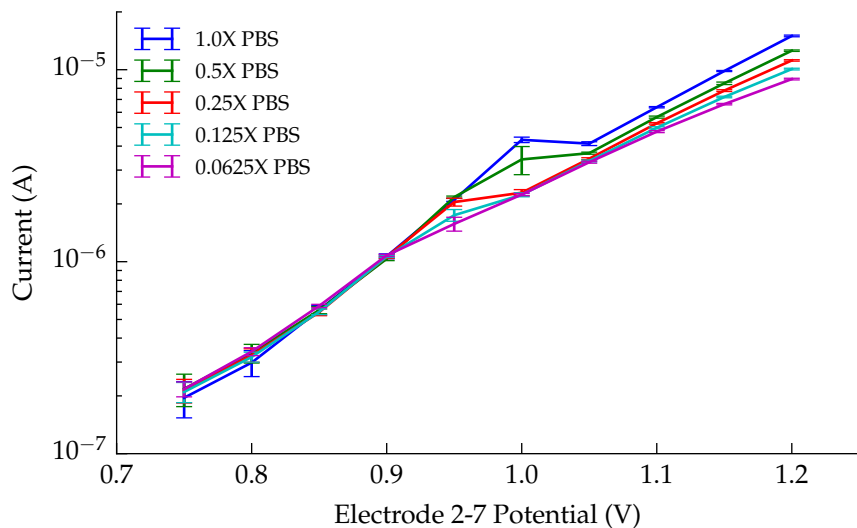


Figure 8.14: Graph showing the electrical current draw associated with Faradaic reactions versus applied electrode overpotential. Measurements used the stepped method with a wait time of 64 s between transitions. Vertical bars mark the standard deviation of the final fourty measurements before the following step.

It appears that the change in behavior between 0.9 V and 1.05 V is due to a transition to diffusion-controlled conduction between electrodes. I hypothesise that below 0.9 V the charging of the CPE draws available ions to the electrode, creating a layer of high ionic concentration at the surface irrespective of that of the solution bulk. It is this layer that is consumed by the Faradaic reactions at a rate that increases exponentially with electrode overpotential. The effect of the bulk solution concentration while this layer exists is negligible until the point at which the layer is consumed faster than it can be replenished. At this point, and with increasing overpotential, Faradaic conduction is governed by diffusion of ions from the solution bulk into that layer. The rate at which those new ions diffuse into the layer is a function of the concentration, or abundance of ions available in the bulk. I believe this explains the divergence of conduction with concentration between 0.9 V and 1.05 V and why there is no observable dependence on

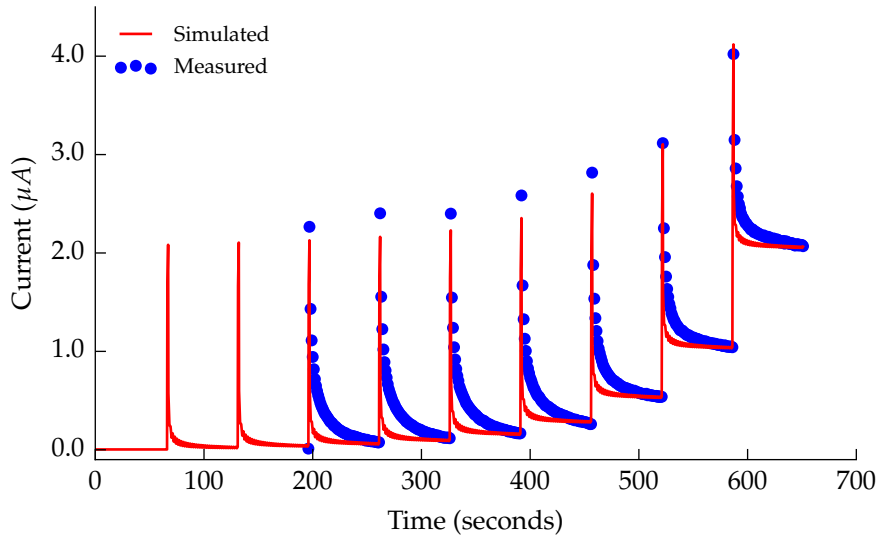


Figure 8.15: Graph comparing measured Faradaic response of a pair of interfaces (1.0X PBS) to the simulated response using fitted parameter values for i_0 and n . Each spike is a step in electrode overpotential, with the steps shown in the following graph.

the bulk ion concentration beforehand. As Faradaic reactions are dangerous in an implanted setting, and therefore to be avoided, interest in Faradaic reactions lies in determining their onset. For the purpose of model it is sufficient to place a 0.9 V limit across a pair of electrodes and proceed on the basis that Faradaic conduction is not affected by the saline concentration.

Using the “step and wait” method to measure electrical currents associated with Faradaic conduction gave improved results, both in repeatability and expected response. Figures 8.15 and 8.16 show results using the 1.0X PBS solution; the other concentrations followed the same pattern. In fig. 8.15 it can be seen that the simulated CPE does not follow the decay curve of the interface after each transition. Notice again how the rate of decay appears to be dependent on the electrode overpotential, with higher voltages resulting in lower apparent capacitance. This suggests that in order for the simulated

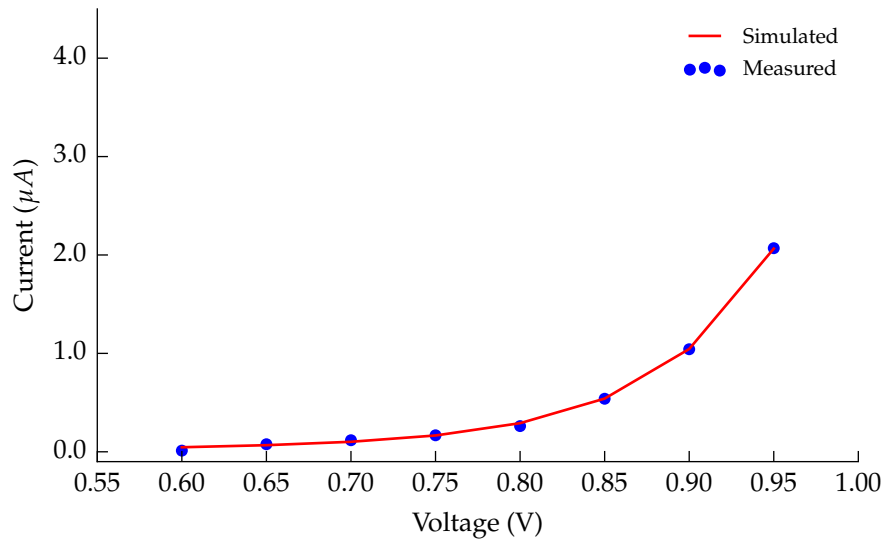


Figure 8.16: Graph comparing the measured settled electrical currents of Faradaic reactions (in 1.0X PBS) for a pair of interfaces to simulated final values using the fitted parameter values for i_0 and n .

Table 8.4: Faradaic parameters

Parameter	Value
i_0	2.757 pA
n	1.36

CPE to better represent the interface's displacement characteristics it should also take the electrode overpotential as a parameter to modify its behavior. No effort was made to incorporate the scaling of capacitance into the CPE of the model, but doing so would be a valuable improvement on the current model. Final parameter values for the Faradaic currents (the diodes of the model) are given in table 8.4.

Table 8.5: Table of determined interface parameters for the St. Jude Medical Octrode in PBS.

Parameter	Value
$R_s (\Omega)$	$13.38 \times \text{concentration}^{-0.8397}$
m	1.34
k	1.773
$ Z @ 1 \text{ Hz} (\Omega)$	$3284 \times \text{concentration}^{-0.158}$
i_0	2.757 pA
n	1.36

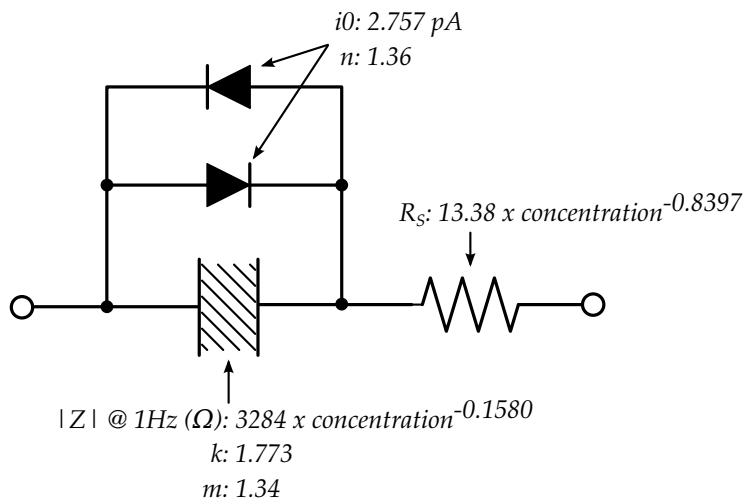


Figure 8.17: Schematic of the electrode-electrolyte interface including parameter values for platinum and buffered saline.

8.1.4 Final Model

Parameter values for each of the model's components have been found. Collecting the parameters that describe the interface's impedance results in table 8.5. This table excludes the parameters of the resistor network as they do not describe the interface itself.

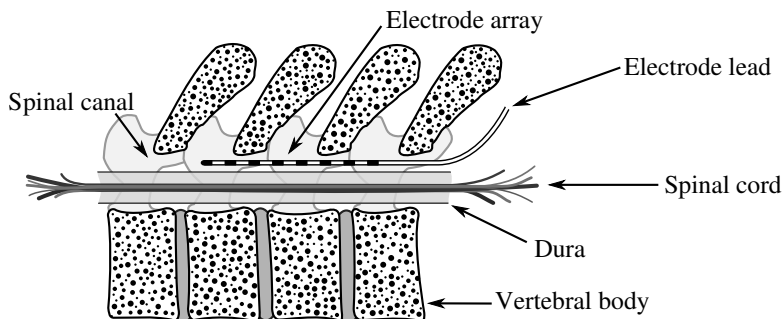


Figure 8.18: Diagram showing the positioning of the St. Jude Medical Octrode electrode array inside the sheep spinal cavity.

8.2 Biological parameter measurements

The previous section dealt with measuring and fitting numerical values to the electrode-interface parameters in various solutions of buffered saline, or PBS. Buffered saline, specifically a 0.1X concentration of a standard saline solution, was used for electrode characterisation as it was believed to be a good substitute for cerebrospinal fluid. Electronic engineers at Saluda Medical used these 0.1X PBS solutions to test their implant devices to make sure they were capable of driving and handling the impedance presented by the electrode-electrolyte interface and spinal cavity. Not knowing how closely the saline solutions resembled live biological spinal fluid they also tested their implants and electrodes in living sheep. A sheep's spinal canal is smaller than a human's, but large enough to insert an epidural electrode array, making them a relatively accessible means of in-vivo testing for medical applications. Measurement in a live sheep's spinal canal still requires a lot of resources such as a surgeon, access to an operating theater, equipment suitable for use in an operating theater, ethical approval, and time. In each case the test sheep would be anaesthetised and kept alive for the duration of the experiments, which often lasted over twelve hours. A veterinary

surgeon would prepare and monitor the sheep constantly during the experiments to ensure that it was fully anethetised and then euthenise the sheep at the end of testing.

These tests offered an opportunity for me to characterise the electrode-electrolyte interface inside a living mammal. This section repeats the measurements and parameter value determination of the previous section but this time inside a living sheep's spinal cavity. The same electrode as was used in the previous measurements (St. Jude Medical Octrode) was inserted into the spinal cavity of the sheep (just outside the dura) for each experiment, as shown in fig. 8.18.

The two sheep used to gather experimental data used here were provided by the Keams Facility at the Royal North Shore Hospital of Sydney under the Animal Care and Ethics Committee approval. These experiments complied with the Australian Code of Practice for the Care and Use of Animals for Scientific Purposes. In each case the sheep were injected with alfaxalone to induce anesthesia and were then intubated and ventilated with an oxygen-air mixture containing isoflurane. During the course of experimentation the animals were monitored using electrocardiogram, arterial blood pressure, arterial saturation, and end-tidal (exhaled) carbon dioxide levels. In short, they were completely unaware of the experiments being carried out and being terminated on completion meant they never became aware. All ethical considerations and procedures around animal testing were handled by Saluda Medical. Unless otherwise stated, measurement procedures and the equipment used in the hospital are the same as those used to measure the response in PBS.

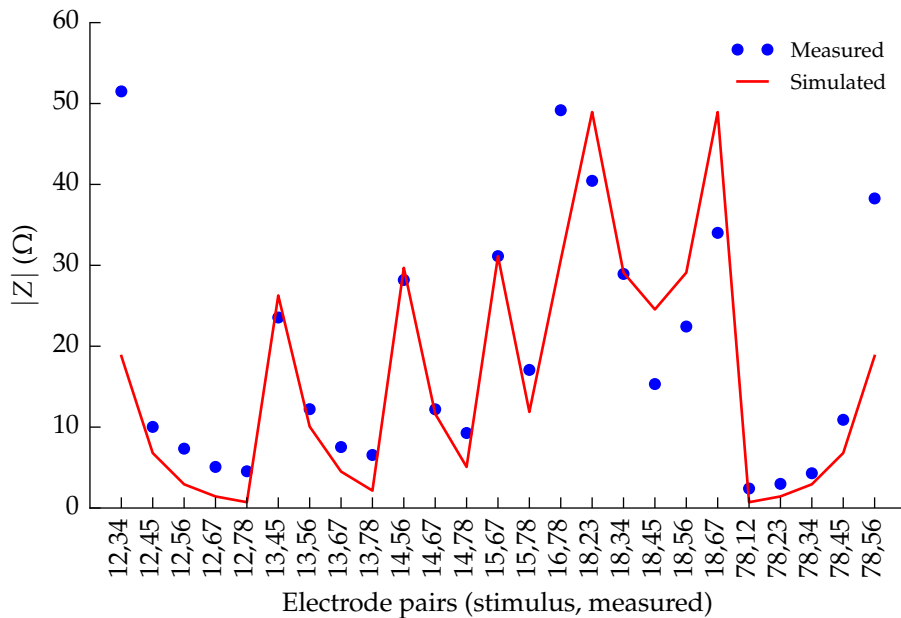


Figure 8.19: Graph showing measured and simulated impedance magnitude for twenty five combinations of stimulus-measure pairs of electrodes.

8.2.1 Resistor Mesh

Transimpedance measurements were made first once the electrode array was inserted into the spinal canal. These measurements were more extensive than those made in saline as additional stimulus electrode pairs were used. The extra measurements were made with the hope that they may capture more information regarding the impedance structure of the surrounding spine geometry, namely bone.

Figures 8.19 and 8.20 show both the measured and simulated results for the impedance magnitude and phase response respectively. The magnitude measurements show that when stimulating between electrodes one and eight and measuring on electrodes two and three that the impedance is approximately that of the one-tenth concentration of PBS (compared with results from fig. 8.2). This result adds validation to the notion that the

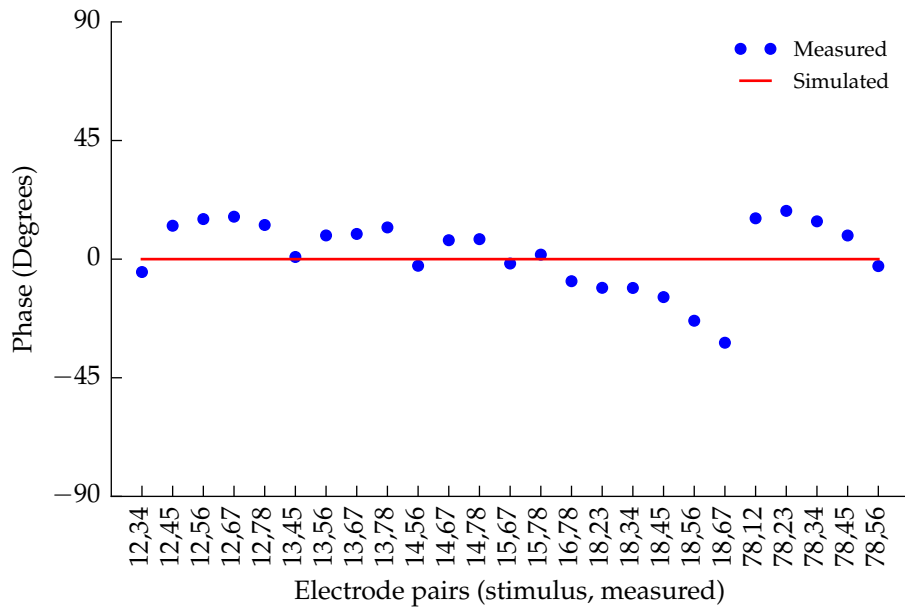


Figure 8.20: Graph showing measured and simulated impedance phase for twenty five combinations of stimulus-measure pairs of electrodes.

one-tenth concentration of a standard buffered saline solution is a good substitute for a spinal cavity. For the case where the stimulus is placed between electrode one and two and the impedance is measured between electrodes seven and eight, comparison points toward a lower concentration of PBS. Swapping the stimulus and measure electrodes around gave different trans-impedance values, i.e., the point at 12,78 does not equal that of 78,12. It is most probably a result of the electrode array shifting whilst inside the sheep, for which nothing could have been done to prevent.

One important insight from these measurements is the phase response, as is shown in fig. 8.20. As much as 30 degrees of phase angle between the stimulus current and electrode voltage was observed when separation between the stimulus and measure pairs is at its maximum. This shows that the spinal cavity itself is a significantly reactive component. For comparison, the PBS solutions displayed no measurable reactance for all of the

Parameter	Value
R_{eri} (Ω)	500
R_{sri} (Ω)	375
R_{li} (Ω)	176
Depth (layers)	5
Padding (layers)	3

Table 8.6: Table of determined resistor mesh parameters for an electrode array in a live sheep's spinal cavity.

equivalent trans-impedance measurements. The decreasing phase angle of measurements using one and eight as stimulus electrodes is a result of the measured pair of electrodes being between the stimulus, i.e., it is a result of our electrode choices. There are other instances where the phase angle appears to drop below zero, but these are likely an artifact of the measurements themselves. Those situations only occur when the stimulus and measured electrodes are adjacent to one another and therefore the impedance, and therefore signal-to-noise ratio, was at its lowest. Stimulus current was reduced for the in-vivo measurements to prevent triggering of any muscles.

The simulated results shown in figs. 8.19 and 8.20 (shown as the red trace) were calculated using the resistor mesh parameter values shown in table 8.6. Those values were determined using the same SciPy optimisation library for Python as was used to fit the values in PBS.

8.2.2 Series Resistance And Constant Phase Element

?? and fig. 8.22 shows the impedance magnitude and phase response of the CPE at the interface between the electrode and the sheep's spinal cavity. Reliability issues on day one meant that no useful data was captured from the first sheep, hence these figures show data only from the second sheep. Measurements on the second day were made over a thirty minute period

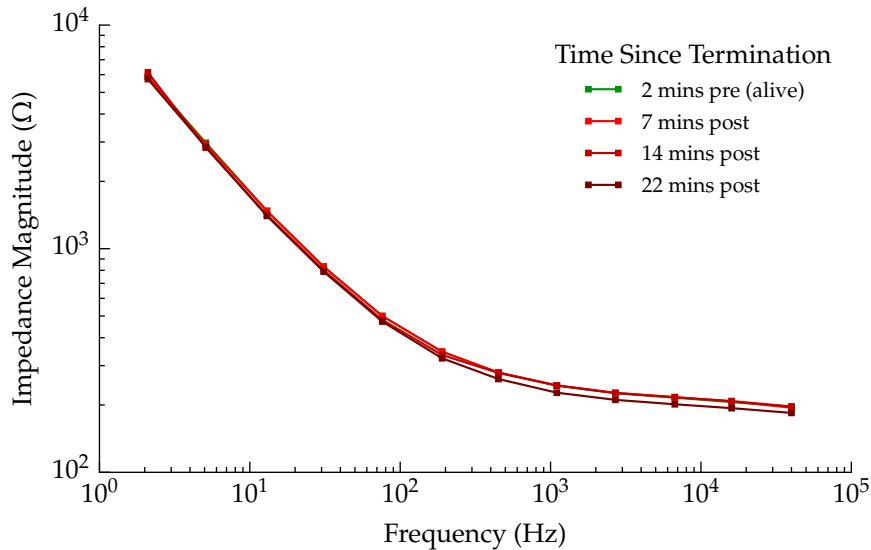


Figure 8.21: Graph showing measured CPE impedance magnitude response before and after termination.

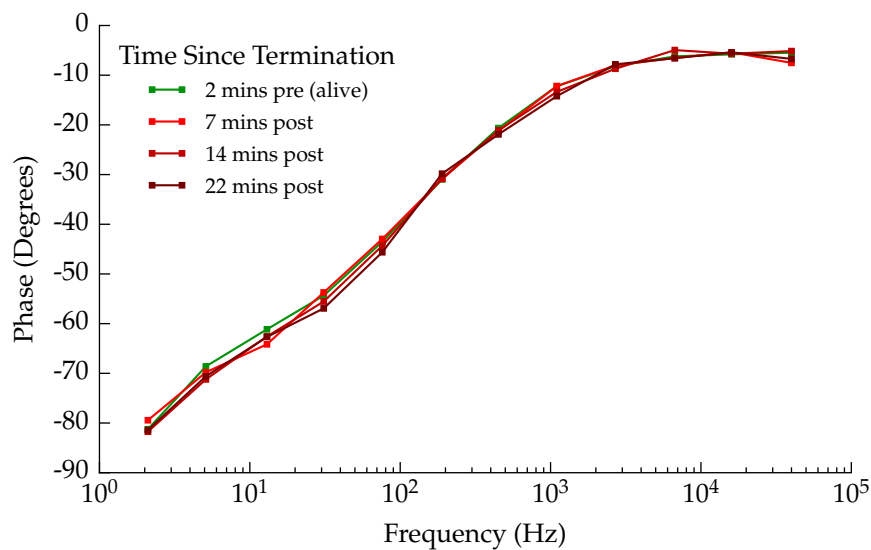


Figure 8.22: Graph showing measured CPE impedance phase response before and after termination.

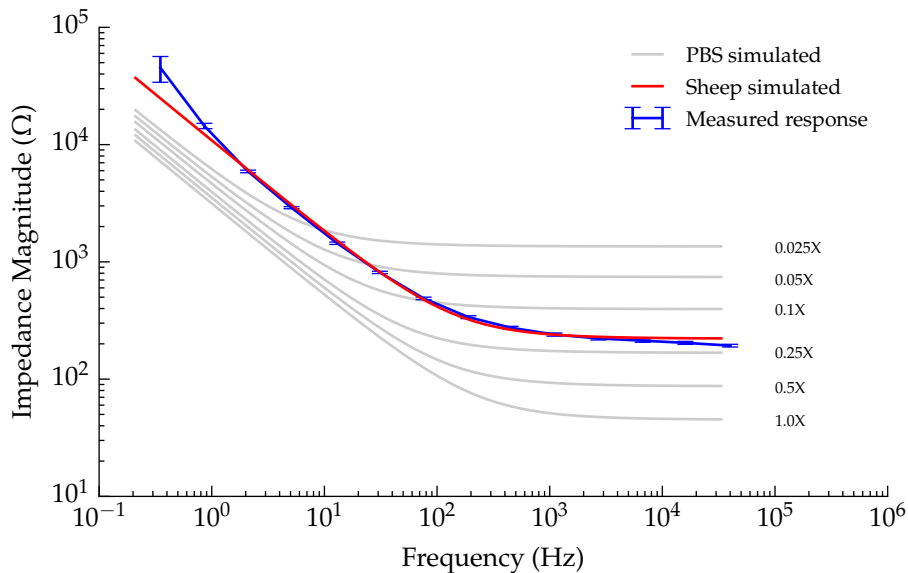


Figure 8.23: Graph showing average CPE response in live sheep compared to the six solutions of PBS, visible as the grey traces, and simulated response based on fitted parameters.

starting two minutes before termination.

An important question that we wished to answer was whether the impedance response in live sheep would be any different to that of a dead sheep. Results indicate that there is practically no difference for at least thirty minutes after termination. However, measurements should have been carried out over a longer time-frame after termination as it would likely take longer for the fluid composition to change. As the measurements required termination of the sheep, they had to be done after all other experiments had been completed. Since each sheep was shared between other research groups, this meant that termination happened late (early the following morning) due to accumulated delays in previous experiments. Measuring the CPE response in the spinal cavity of a butchered sheep would offer a useful reference point for those measurements.

Figures 8.23 and 8.24 compares the average impedance (both magnitude

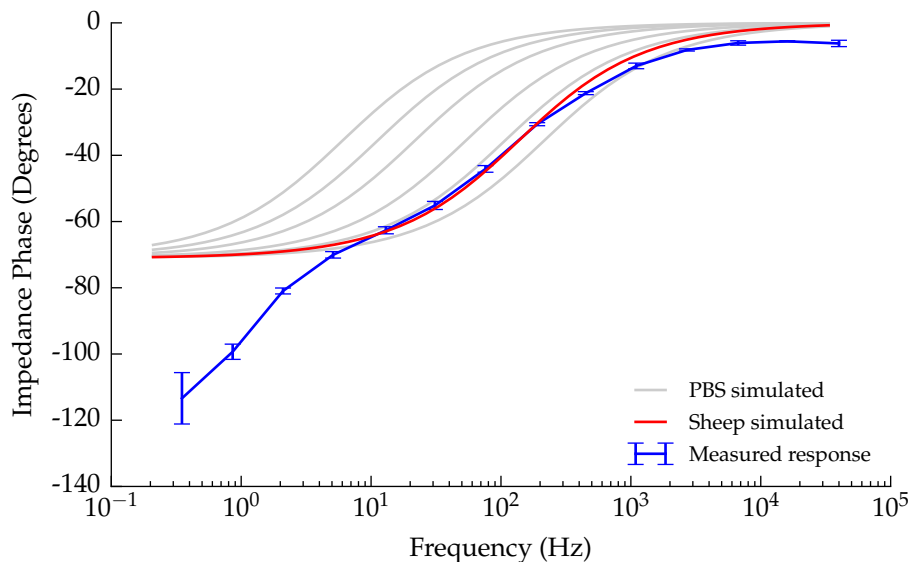


Figure 8.24: Graph showing average CPE response in a live sheep's spinal cavity compared to six concentrations of PBS, visible as grey traces, and simulated response based on fitted parameters.

and phase) of the previous graphs with the six concentrations of PBS used in the previous section. Simulated results from a numerical fit to the measured data appear as the red trace. At low frequencies, below 1 Hz, the simulated data deviates substantially from measured results. The cause for this is unclear, but in chapter 9 the opposite response appears when using unbuffered saline solutions - which may provide a clue. What is interesting is the series resistance in sheep spine is similar to that of a 0.25X PBS solution, whereas the CPE behaves more like that of a concentration much lower than 0.025X. Based on this data, a one-tenth concentration of PBS does appear to be a reasonable approximation to the electrolyte found in a mammalian spinal column, although the match is poor. In the following section the possibility of creating a solution that better matches these results will be explored.

Table 8.7: Table of determined interface parameters for an electrode array in a live sheep's spinal cavity.

Parameter	Value
R_S	126Ω
m	1.34
k	1.77
$ Z @ 1\text{ Hz} (\Omega)$	$11.3\text{ k}\Omega$
i_0	Undetermined
n	Undetermined

8.2.3 Faradaic Current

Faradaic measurements on the live animal were abandoned as they were deemed likely to cause muscle contractions. Attempts were made to measure Faradaic response using a much lower stimulus current but this only resulted in noise and were discarded. These measurements may be possible if done after a long enough duration post-termination, to prevent muscle movement.

8.2.4 Final Model

Parameter values for the final sheep model are presented in table 8.7. Unfortunately, the diode/Faradaic parameters were not obtained on live sheep due to safety concerns. Those measurements are likely to be of value to implant designers as they provide a reference for the beginnings of Faradaic conduction. Access to a recently terminated sheep's spine, and a surgeon, would provide a way of collecting those Faradaic measurements and additional post-termination samples.

Parameters for the interface model in sheep have been fitted. It appears as though buffered saline, of any concentration, is not an ideal representation of a live sheep's spinal cavity. The next research question is to determine

if it is possible to create a solution that better matches those impedance characteristics.

Chapter 9

Recipes For Fluid Mimicry

Utilising the measurement methods used previously, a liquid that better replicates a biological impedance is sought. This work is of benefit to engineers of medical implant devices. Having the ability to formulate a solution that mimics the electrical conditions inside a living mammal reduces the resources required to test electronic implants.

It was previous mentioned that the developers of spinal cord stimulator implants used solutions of PBS having a one-tenth concentration as a test fluid for their implants. This solution was the best substitute for an actual live spine that these engineers had. Solutions of the $0.1 \times$ PBS were held in drums within the electronics laboratories for use whenever a quick tests needed to be carried out. Electrodes were submerged into these buckets in order to recreate the electrical conditions inside a human spine.

This was not the only way to simulate the impedance conditions inside a person. As presented in section 8.2, the use of anaesthetised sheep were also used. A sheep's spine is smaller than a human's but is a good approximation in term of geometry. However, the resources involved with conducting a live sheep trial are high; requiring use of a hospital operating theatre, surgeon veterinarian, and equipment.

Engineers had no way of knowing how well those baths of saline represented a sheep's spine. It was shown in section 8.2 that the match between the two was weak. With that knowledge, and the measurement techniques developed thus far, research into creating a solution that better matches sheep spine is carried out. Such a match would reduce the number of surgical operations the test engineers might need to conduct, saving resources and reducing time.

9.1 Measurements

The measurement equipment used to conduct the measurements were the same as those used in the lab.

9.1.1 Configuration

The function generator, Agilent 33220A, and oscilloscope, Tektronix TPS 2024, are connected to the electrode array, St. Jude Medical - Octrode, as is shown in fig. 9.1. A $10\text{ k}\Omega$ resistor was used to measure the current driven between electrodes eight and three. It had a measured resistance of $9.990\text{ k}\Omega$, as measured with a Fluke Digital Multimeter.

9.1.2 Procedure

Each measurement run begin at the upper end of the frequency spectrum and proceeded towards the low frequency endpoint. Starting with the higher frequencies offers a chance to confirm correct measurement set-up early in the measurement. A sample at the lowest frequency can take over a minute to acquire, where the higher frequencies drop to under a second. The same frequencies were chosen that were used to measure the situation

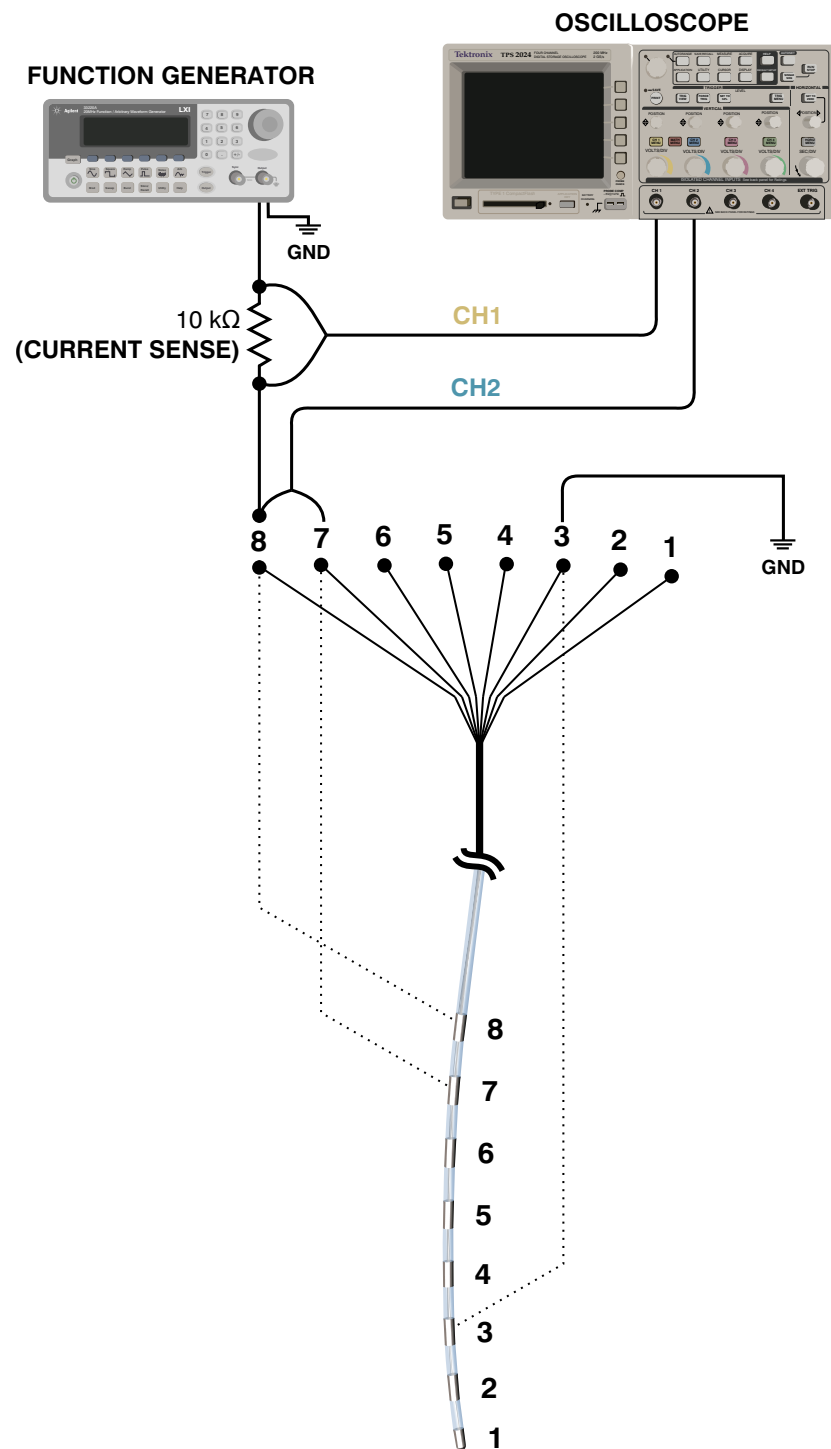


Figure 9.1: Diagram showing the measurement configuration used to measure the CPE response and resistivity of mixed solutions

in live sheep. This allows easy comparison between the sheep data and the impedance of mixed solutions.

Measurements were completely automated via a Linux based computer running Python scripts. These scripts controlled the output settings of the waveform generator and acquired the resulting waveforms from the oscilloscope. The scripts had the ability to set the horizontal and vertical scales on the oscilloscope channels in order to ensure appropriate scales were used.

The measurement procedure followed by the script is shown as a simplified flowchart in fig. 9.2. The programme steps through each of the required frequencies, making sure the target voltage is developed across electrodes seven and eight, calculating the interface impedance.

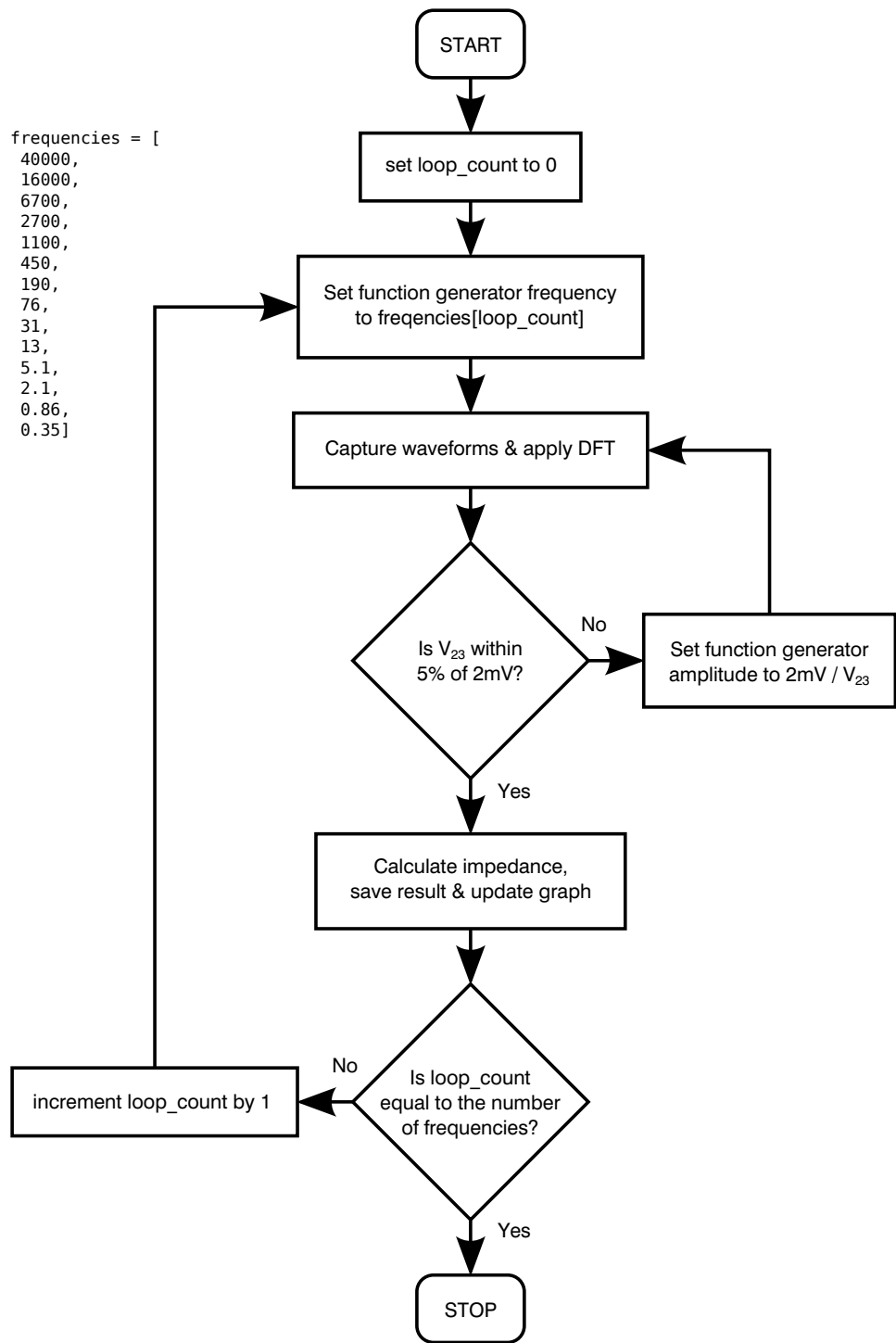
The target voltage across the interface is 20 mV. This voltage was previously determined as a safe stimulus voltage in that it does not trigger Faradaic reactions at the electrode's surface. Because the impedance of the interface changes with frequency, it is necessary to alter the output amplitude to keep the voltage across electrode seven and eight consistent.

This measurement configuration differs from the three channel method used in earlier measurements. Those used channel three of the oscilloscope to watch the voltage developed between electrodes three and eight.

9.1.3 Ingredients Tried

To determine how certain additives affect the impedance of the interface, a range of ingredients were mixed and tested. Various mixtures were created in a trial-and-error fashion until trends emerged which eliminated many of the ingredients. The following ingredients were tried for mixture creation:

- Glycerol

**Figure 9.2:** Diagram showing the execution of the measurement script

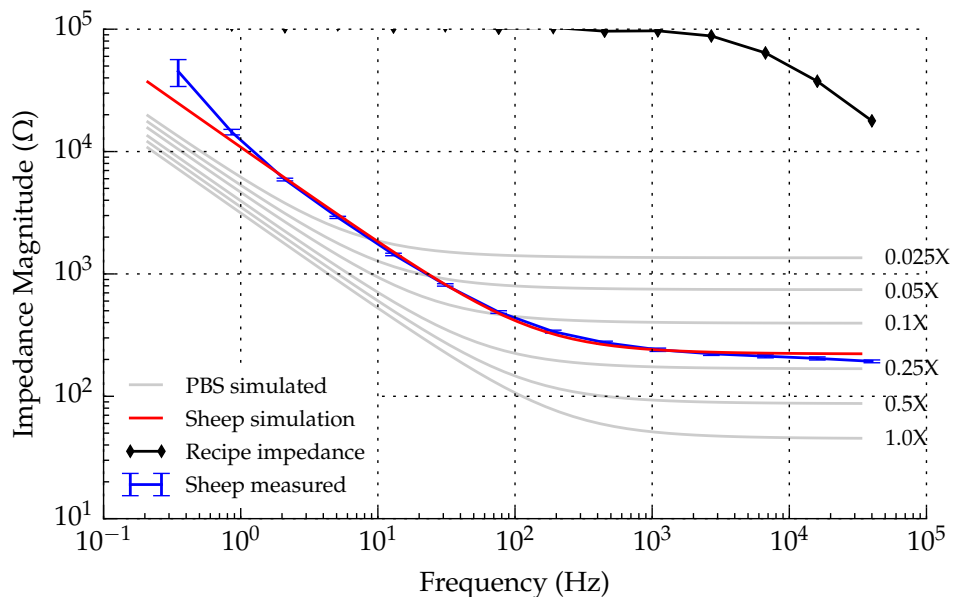


Figure 9.3: Plot of impedance magnitude versus frequency (log-log) for distilled water.

- Methylated Spirits
- Sodium Carbonate
- Sodium Bicarbonate
- Table-salt (non-iodised)
- Gelatine
- Citric Acid
- Corn-flour

9.1.4 Results

Water, Corn-flour and Salt

Figures 9.3 to 9.10 show a progression of measurements beginning with distilled water, then adding cornflour, then adding salt, and finally adding a

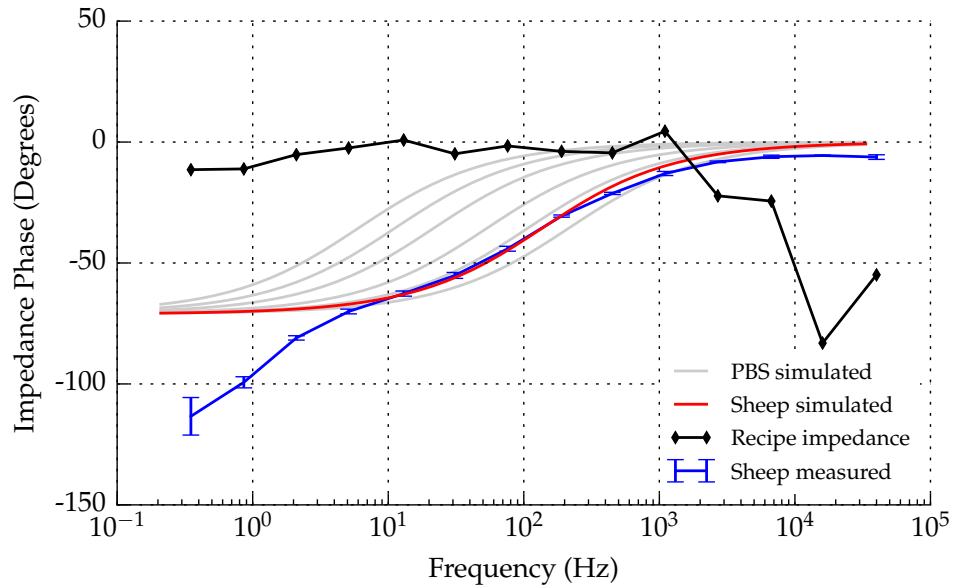


Figure 9.4: Plot of impedance phase versus frequency (log-log) for distilled water.

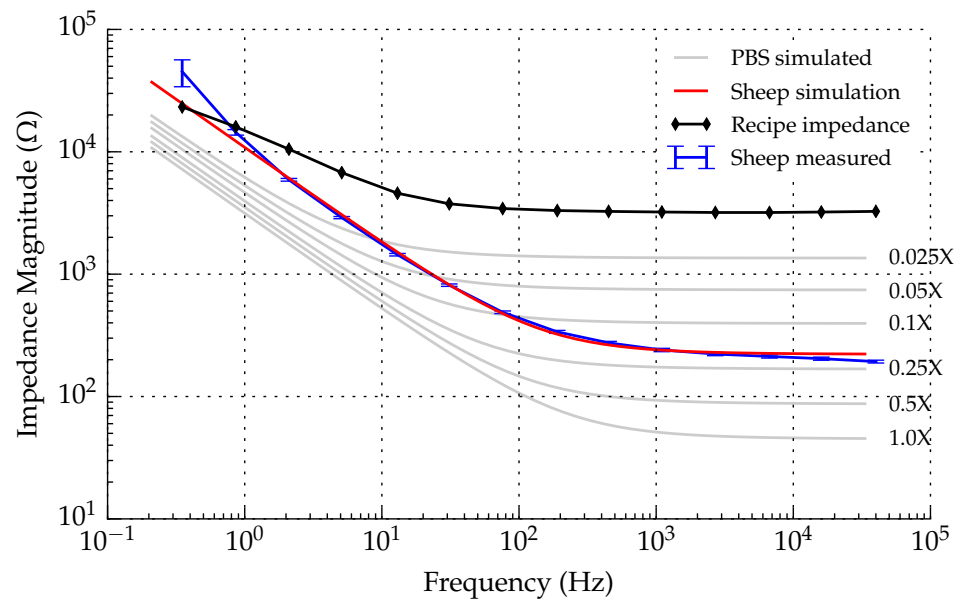


Figure 9.5: Plot of impedance magnitude versus frequency (log-log) for 250 g cornflour mixed with 175 ml distilled water.

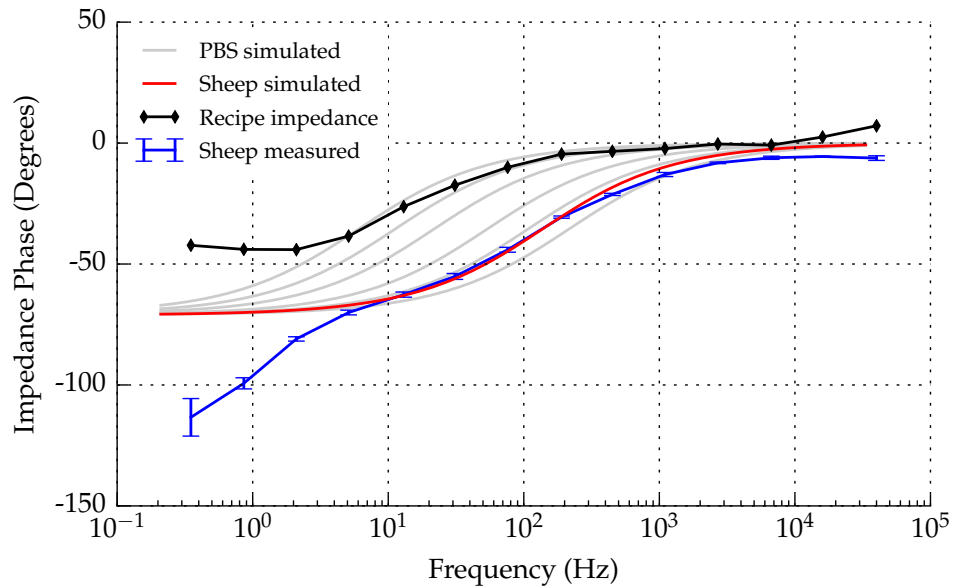


Figure 9.6: Plot of impedance phase versus frequency (log-log) for 250 g cornflour mixed with 175 ml distilled water.

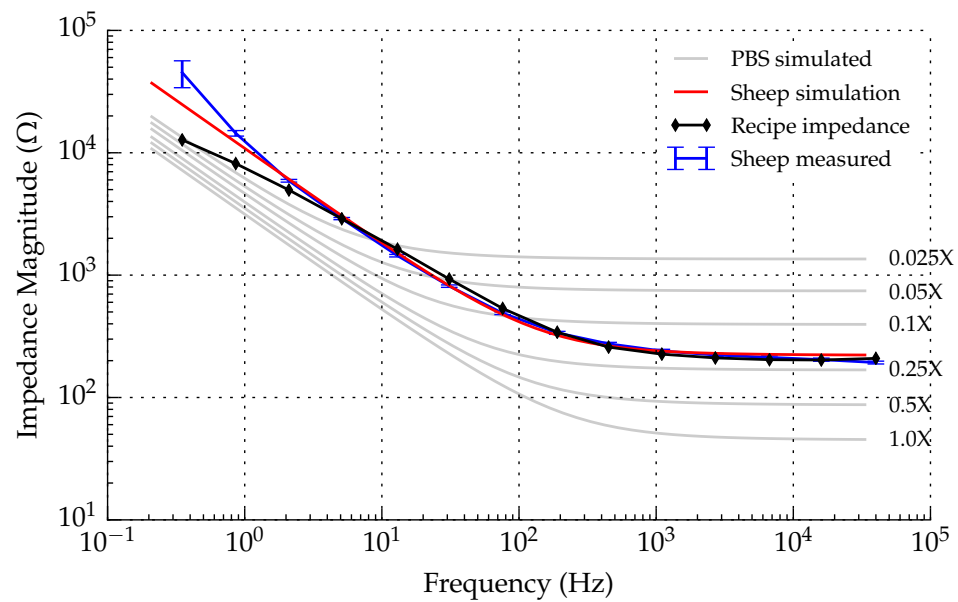


Figure 9.7: Plot of impedance magnitude versus frequency (log-log) for 250 g cornflour mixed with 175 ml distilled water and 1.9 g table-salt.

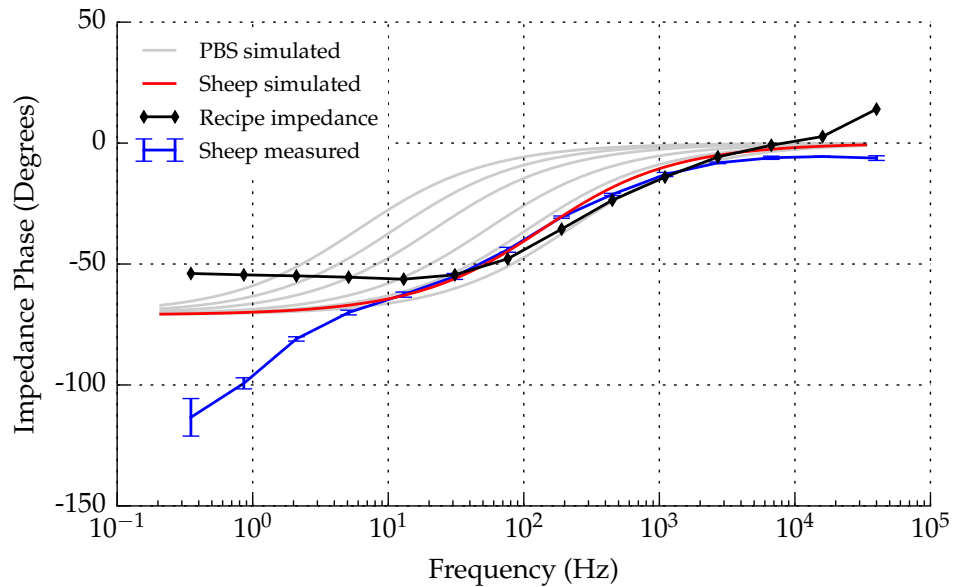


Figure 9.8: Plot of impedance phase versus frequency (log-log) for 250 g cornflour mixed with 175 ml distilled water and 1.9 g table-salt.

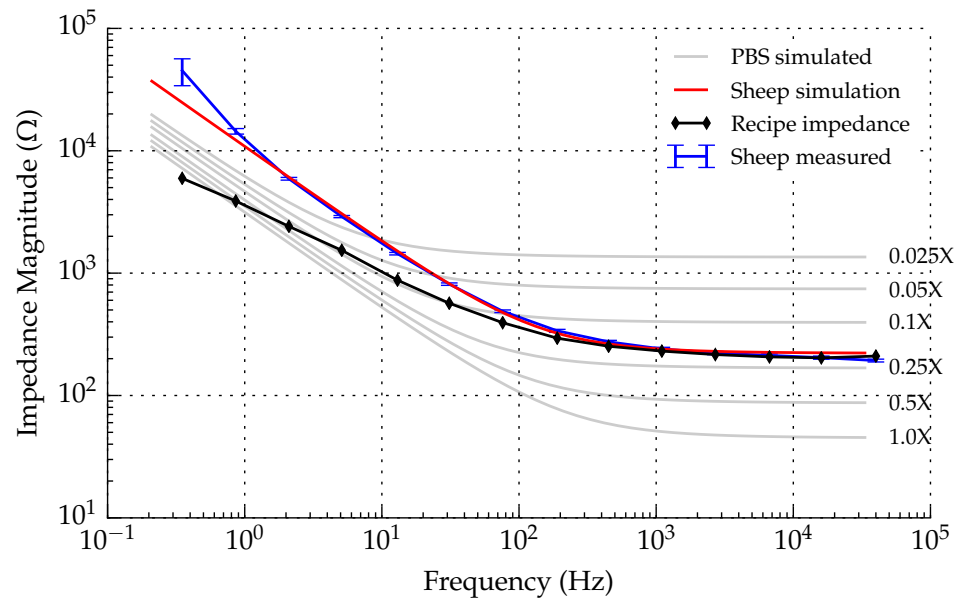


Figure 9.9: Plot of impedance magnitude versus frequency (log-log) for 250 g cornflour mixed with 180 ml distilled water and 1.9 g table-salt.

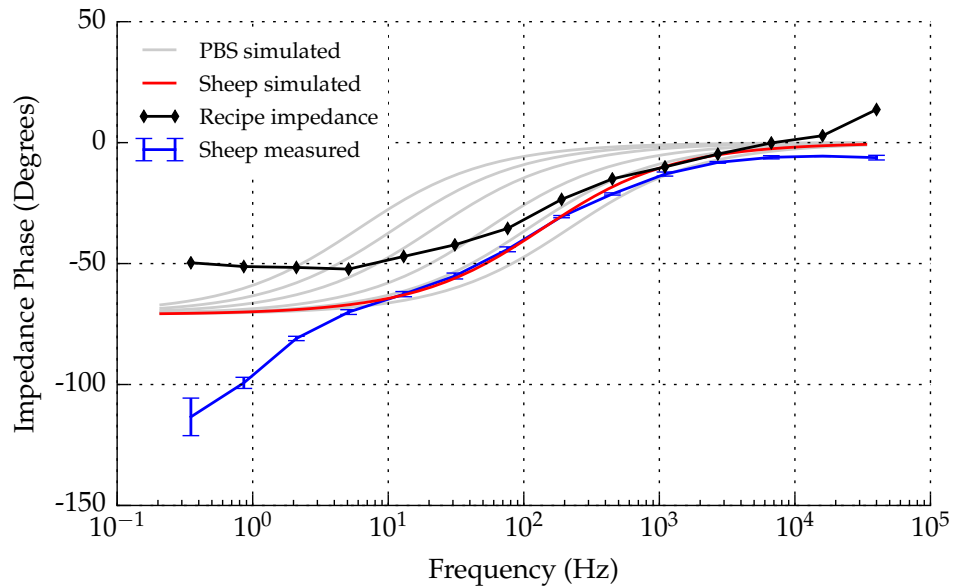


Figure 9.10: Plot of impedance phase versus frequency (log-log) for 250 g cornflour mixed with 180 ml distilled water and 1.9 g table-salt.

very small amount of extra water.

Improved Water, Corn-flour, and Salt

Figures 9.11 and 9.12 show the results of mixing the same set of ingredients as the previous measurement set, but with the closest fit to sheep spine obtained.

9.1.5 Discussion

These results show that it is possible to alter the CPE response and the bulk conductivity of the solution independently of one another. Figures 9.11 and 9.12 show a greatly improved match relative to that of any single concentration of PBS. Unbuffered saline solutions all dipped in impedance magnitude at low frequencies, something not observed when using buffered saline such as PBS. It is expected that using buffered saline solutions would

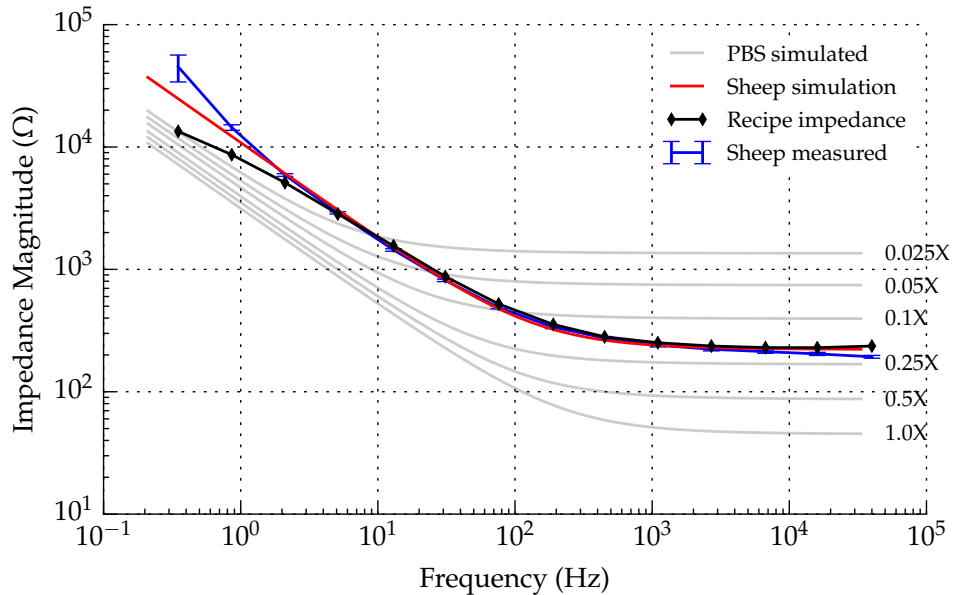


Figure 9.11: Plot of impedance magnitude versus frequency (log-log) for 190 g cornflour mixed with 190 ml distilled water and 0.858 g table-salt.

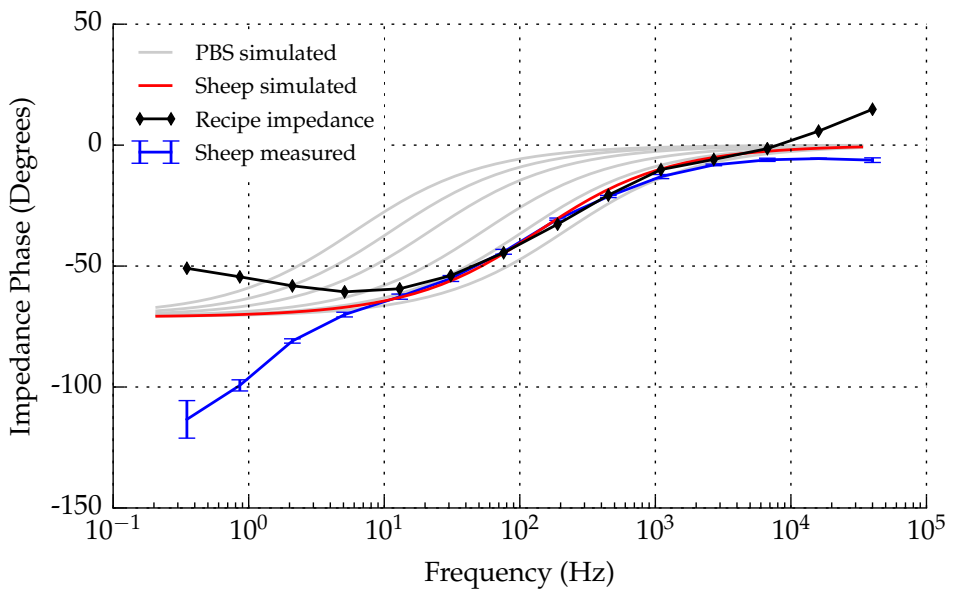


Figure 9.12: Plot of impedance phase versus frequency (log-log) for 190 g cornflour mixed with 190 ml distilled water and 0.858 g table-salt.

bring the low-frequency response back in line with the PBS trace. It may also be possible to select an appropriate buffering agent that better matches the response of the sheep's biological fluid. These results are promising and no doubt will be of use not only to implant designers but to anyone trying to mimic the electrical impedance of biological fluids.

Part III

Appendices

Chapter A

Charged Droplet Energy Harvester

In 1867 William Thomson (Lord Kelvin) described an apparatus that could generate electrostatic charge using drops of water (some of which are shown in Figure A.1) [50].

This apparatus works by inducing charge onto drops of water before they detached from the source of the drips. It is this apparatus that forms the basis for the investigation of the of charged drops of water to generate useful amount of power.

A.1 How charge is generated

Figure A.2 shows one of the charge generating mechanisms of Lord Kelvin's electrostatic generator. This mechanism is comprised of three main components, a jet of water that breaks to form droplets of water, an inductor surrounding the point at which the stream of water breaks and a receiver where the charged water droplets are condensed.

A simplified diagram of the apparatus is shown in Figure A.3 and will be used to explain the concept further.

The diagram illustrates the charge of each element by its colour. Equal and opposite amounts of electrical charge are accumulated in each of the

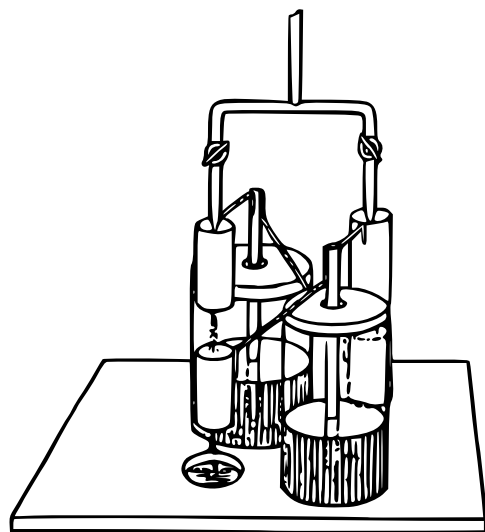


Figure A.1: Drawing of Lord Kelvin's electrostatic generator.

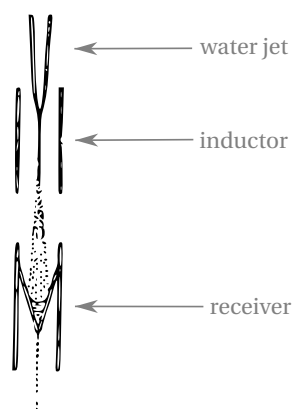


Figure A.2: Drawing of the charging mechanism for Lord Kelvin's electrostatic generator

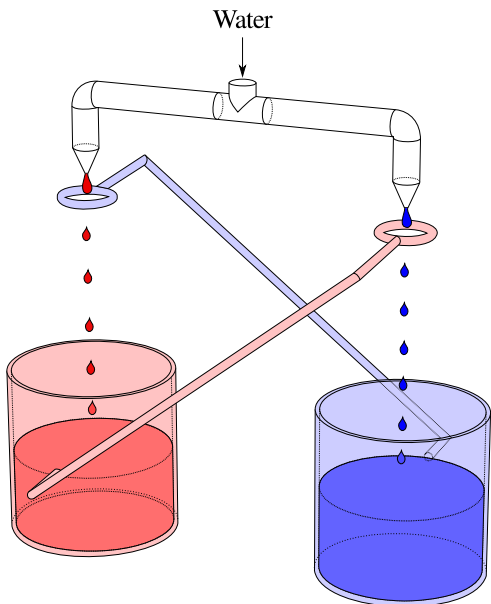


Figure A.3: Simplified diagram of Lord Kelvin's water dropper configuration

containers at the bottom. These containers are insulated from one another but are connected to the rings (near the droppers) of the opposite side. The rings are responsible for inducing excess charge on the drops (equivalent to the cylinder shaped inductor depicted in Figure A.2), which becomes trapped on the drop once it detaches from the dropper. Once detached, the drops are pulled by gravity into the containers below. Because the container below is charged with like charges there is a repulsive force between the falling drop and the container. It is this force acting over the distance through which the drop falls that is responsible for doing work (forcing the drop onto a body that has the same net polarity of as the drop) and thus increasing the voltage of the container/ring.

A.2 Replicating the experiment

The first step toward assessing the electrostatic generators ability to generate energy for the water meter was to replicate the experiment. This work was done by a Summer Research Scholarship student Jonathon McMullen.

A.3 Optimising output

Once the experiment had been replicated, questions arose regarding how to best optimise the design.

A.3.1 Drop volume and frequency

The first optimisation question in its most practical form was “is it better to have lots of small drops or less larger drops?”. To answer this question a more simplified experiment was performed with the help of another summer research student, Wayne Crump. The purpose of this experiment was to remove as many variables from the electrostatic generator experiment performed by Jonathan McMullen (see subsection A.2) in an attempt to isolate the effect of varying drop size, induction voltage and flow rate, independently.

Experimental setup

A photo of the measurement setup can be seen in Figure A.4. For clarity, a diagram of the experimental setup is shown in Figure A.5. As can be seen in this diagram, drips are formed from the end of a syringe needle, pass through the induction ring and land on a piece of tin foil before running off into a catchment container. A closeup of the needle and inductor is shown in Figure A.6. The frequency of drips is determined acoustically by the use of



Figure A.4: Photo of experimental setup for charge on drip measurements.

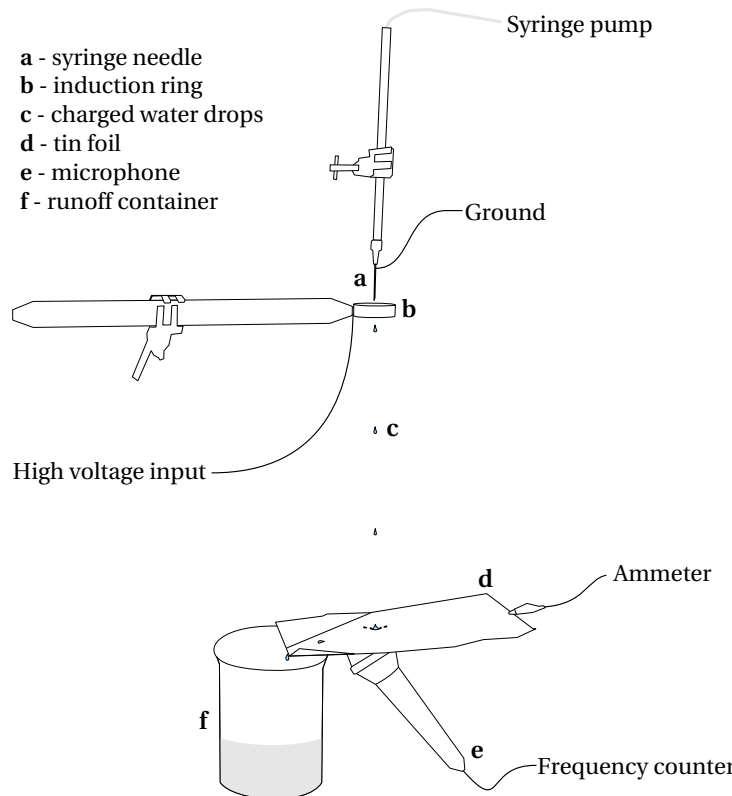


Figure A.5: Diagram of experimental setup for charge on drip experiments

the microphone and the flow of water is set by the syringe pump (as shown in Figure A.7).

The volume of each drip is calculate by dividing the flow rate by the drip frequency. The charge on each drop of water was determined by dividing the average current by the drip frequency. The size of drips was determined largely by the size of needle used but was also affected by the magnitude of the induction voltage placed on the ring.

Because the current being measured was so small (in the nano-amp range), direct measurement with a multimeter was not possible. Instead the multimeter (a Fluke series 115 handheld multimeter) was set to measure voltage in the mV range. In this setting the multimeter has an internal resistance of $10 M\Omega$ (as measured with another multimeter) over which the

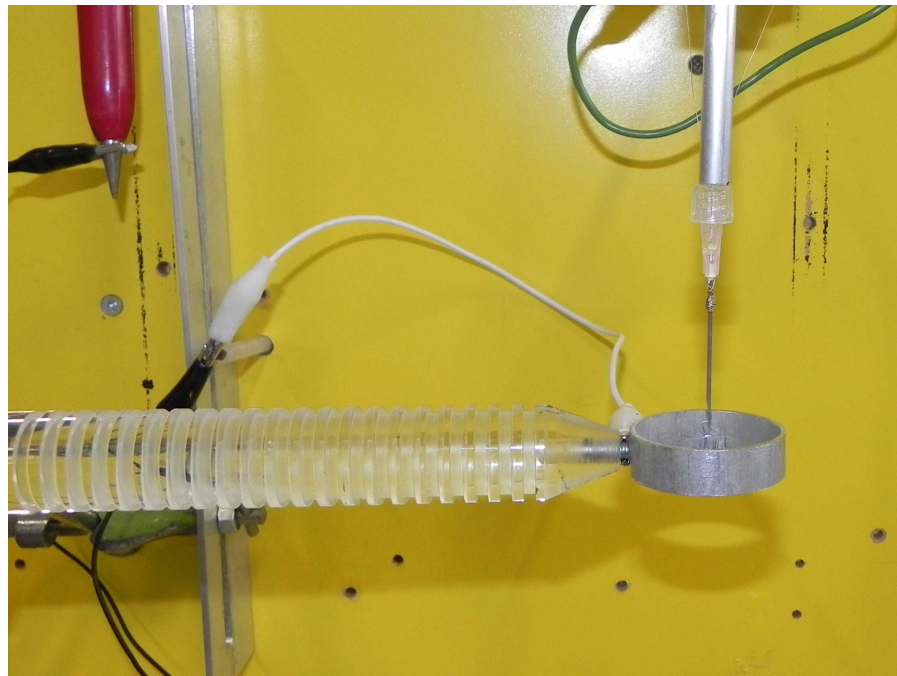


Figure A.6: Photo of the dropper and high voltage inductor.

voltage was being measured. Ohms law states:

$$V = IR \quad (\text{A.1})$$

Where V is voltage, I is current and R is resistance. Rearranging this equation and substituting in our resistance of $10 M\Omega$ we get

$$I = \frac{V}{10 \times 10^6} \quad (\text{A.2})$$

Where V is the output of the multimeter and I is the current through the multimeter, through which we assume all charge collected on the tin foil will flow.



Figure A.7: Syringe pump used to produce drops and control flow rate.

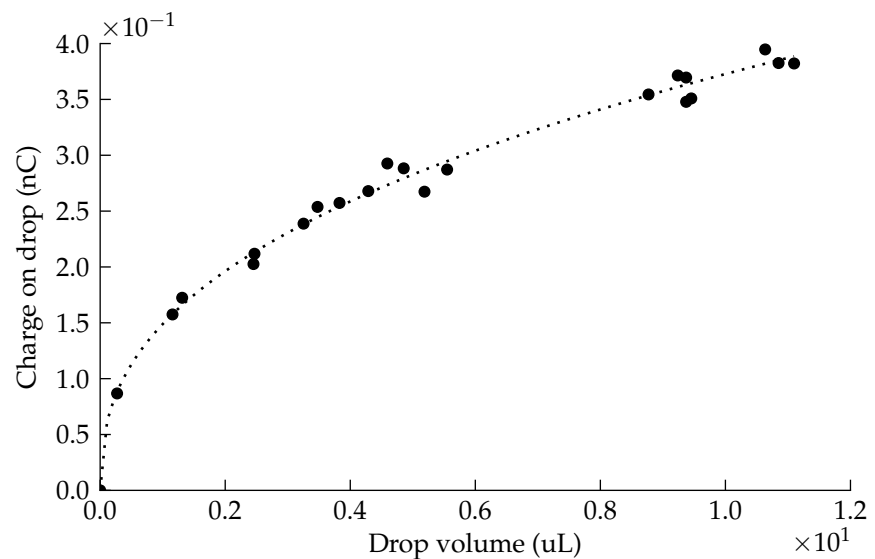


Figure A.8: Charge on drip versus drip volume for a fixed induction voltage of 2.5 kV.

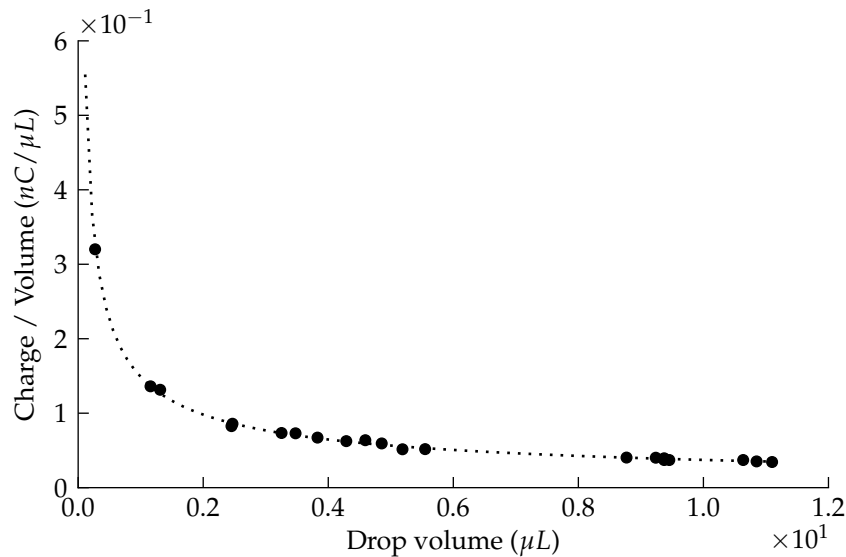


Figure A.9: Charge per volume versus drop volume for a fixed induction voltage of 2.5 kV.

Results

Figure A.8 shows the effect that changing the volume of each drop has on the amount of charge bound to that drop. The shape of this curve is similar to what one gets when plotting the surface area of a sphere against the volume of a sphere. This was expected to be the case since excess charge will position itself evenly over the surface of the drop and hence be proportional to its surface area. If the same data is plotted in terms of charge per volume versus volume of a drip, as is shown in Figure A.9, it is evident that smaller drop sizes equate to a higher charge per volume of water ratio.

Figure A.10 shows the results of changing the induction voltage on the average charge carried per drop. These results indicate that the charge induced on a drop is proportional to the induction voltage. Variation in the measurement data was due to differences in room temperature.

Figure A.11 shows the effect of increasing the flow on the output current

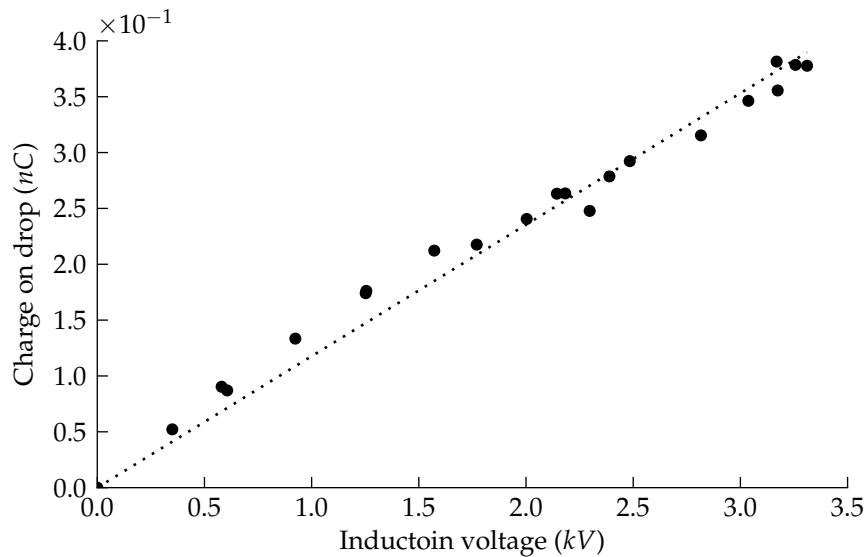


Figure A.10: Charge on drip versus ring induction voltage for a fixed drip volume

of the measurement setup, which is relatively linear.

Conclusion & discussion

Increasing the output of the initial apparatus is possible by doing any of the following things:

- Favour smaller drops at higher frequencies.
- Increase the total flow of water through the apparatus.
- Increase the induction voltage.

Increasing the total flow through the apparatus is difficult to achieve as this soon has adverse effects on the formation of drops. This usually leads to the formation of a stream of water from the needle, reducing the output as the drips aren't forming within the inductor.

Favouring small drops or increasing the induction voltage both increase the charge to mass ratio of individual drops. As this ratio increases the

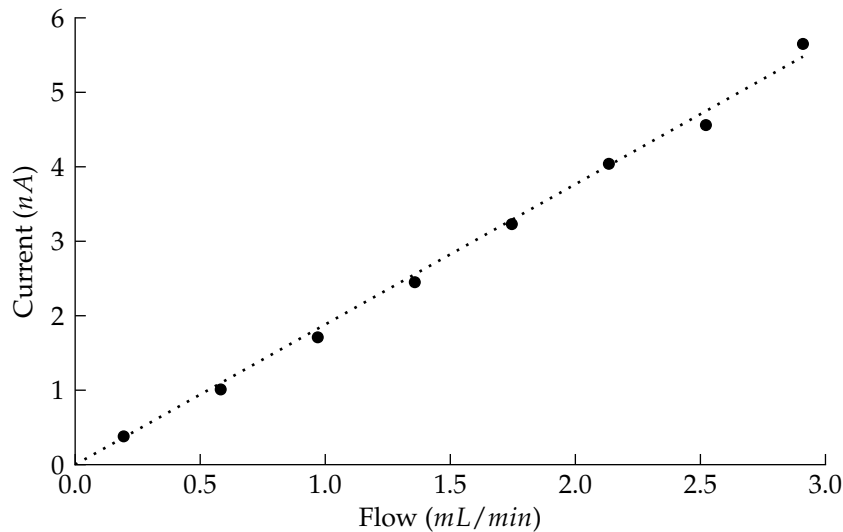


Figure A.11: Current versus flow rate for an induction voltage of 3.8 kV and drop volume of $3.1\text{ }\mu\text{L}$.

movement of the drops becomes increasingly dominated by electrostatic forces between the container and the drop. As this ratio increases so to does the tendency for drops to diverge from the path dictated by gravity. Eventually there comes a point where the drops no-longer fall and instead create a stream that loops to the nearest point on the induction ring. For this reason it is important that drop sizes are kept consistent as to maintain a stable charge to mass ratio to which the design can be optimised for.

A.3.2 Scale

Due to the size of the apparatus the fields generated had to be relatively large, requiring equally large voltages before useful amounts of power is generated. There are two problems with generating power at such large voltages:

1. Large voltage differences try very hard to neutralise each other. This means that the geometry and materials used may need to be modified

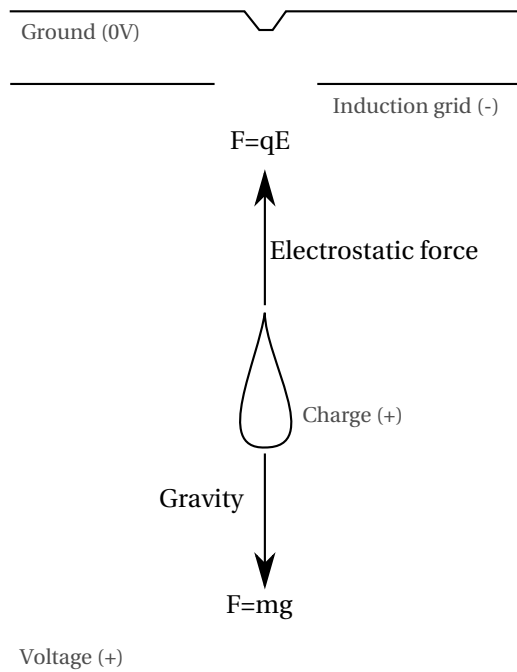


Figure A.12: Diagram of the electrostatic force and gravity acting on a drop of water.

in order to reduce charge migrating over insulating barriers.

2. Stepping these voltages down to a useful level is challenging and would be very inefficient. Electronic components and configurations that would usually be used to change voltage levels no longer work.

Scaling down the design would allow the device to generate its maximum practical output at voltages that are easier to deal with.

Investigation:

Figure A.12 shows a simplified diagram of the two dominant forces acting upon a charged drop as it falls towards a like charged plate from a grounded plane. These two forces are given by the following equations:

$$F_{down} = mg \quad (\text{A.3})$$

$$F_{up} = qE \quad (A.4)$$

Where m is the mass of the drop, g is the acceleration due to gravity, q is the charge on the drop and E is the electric field strength.

Chapter B

Streaming Cell Voltage Measurements

For compactness, the pressure/voltage graphs for individual streaming cell channel heights were omitted from chapter 3. They are presented here in order of increasing internal channel widths. The graph showing all results combined is presented earlier as fig. 3.11.

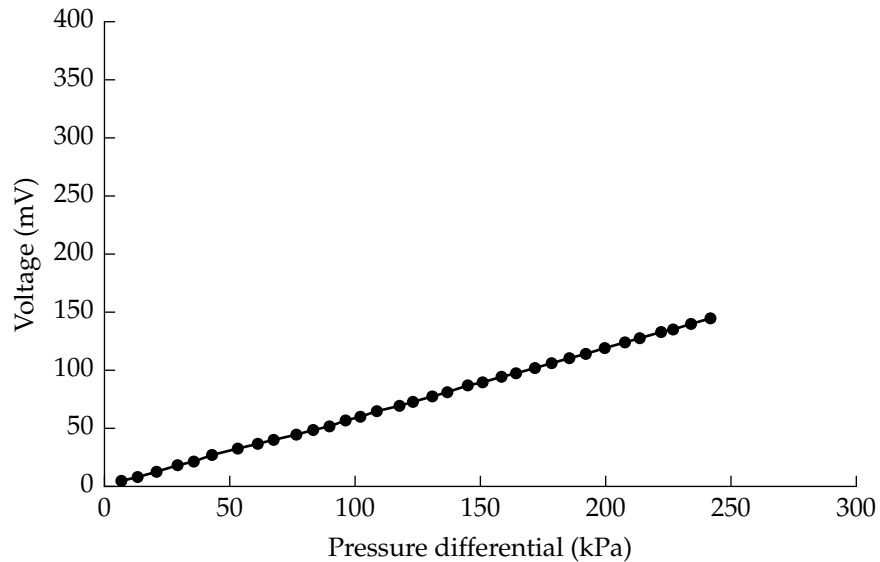


Figure B.1: Graph showing the voltage output with applied pressure differential across a 26 μm glass micro-channel (38 mV offset added)

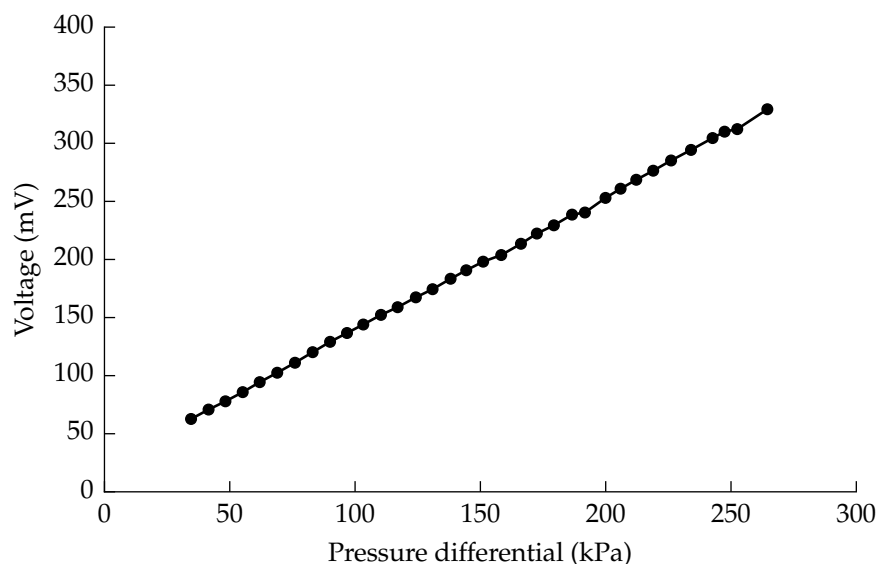


Figure B.2: Graph showing the voltage output with applied pressure differential across a 52 μm glass micro-channel (23 mV offset added)

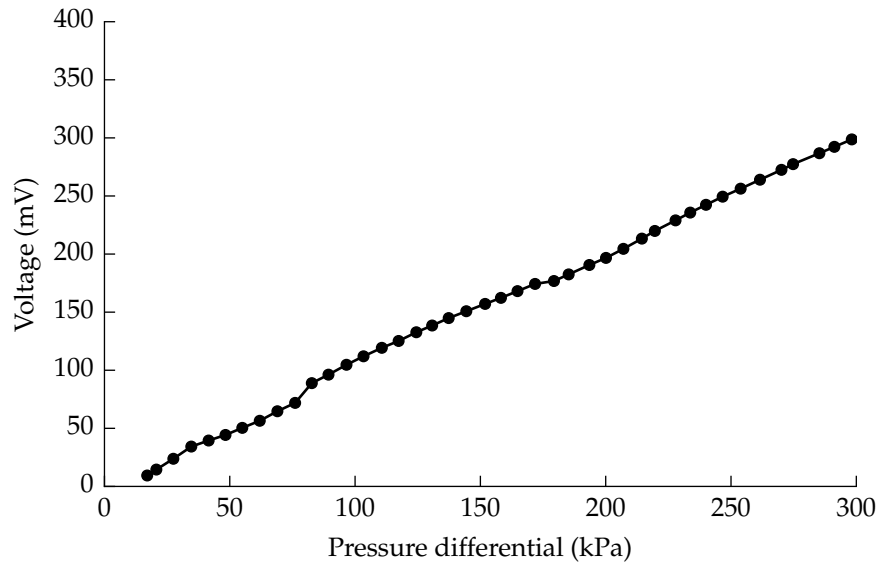


Figure B.3: Graph showing the voltage output with applied pressure differential across a 56 μm glass micro-channel (405 mV offset added)

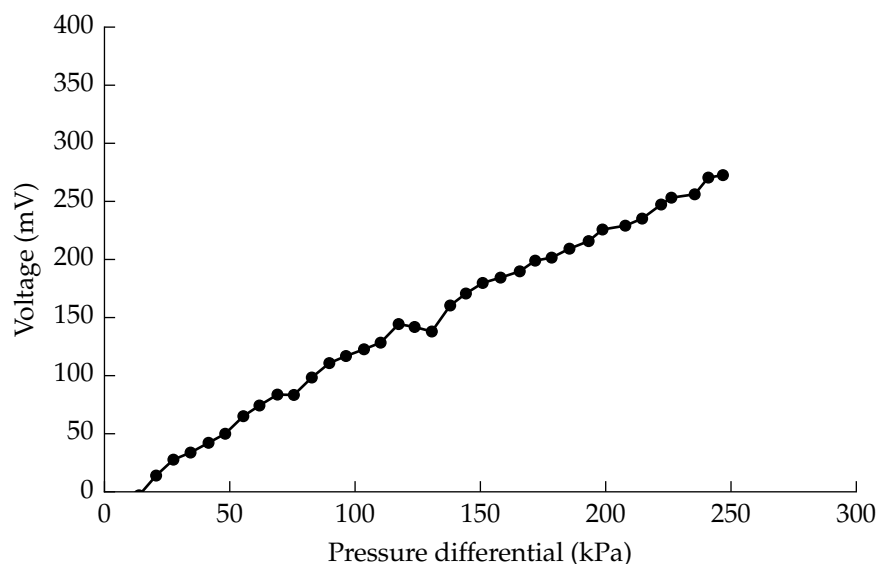


Figure B.4: Graph showing the voltage output with applied pressure differential across a 71 μm glass micro-channel (44 mV offset added)

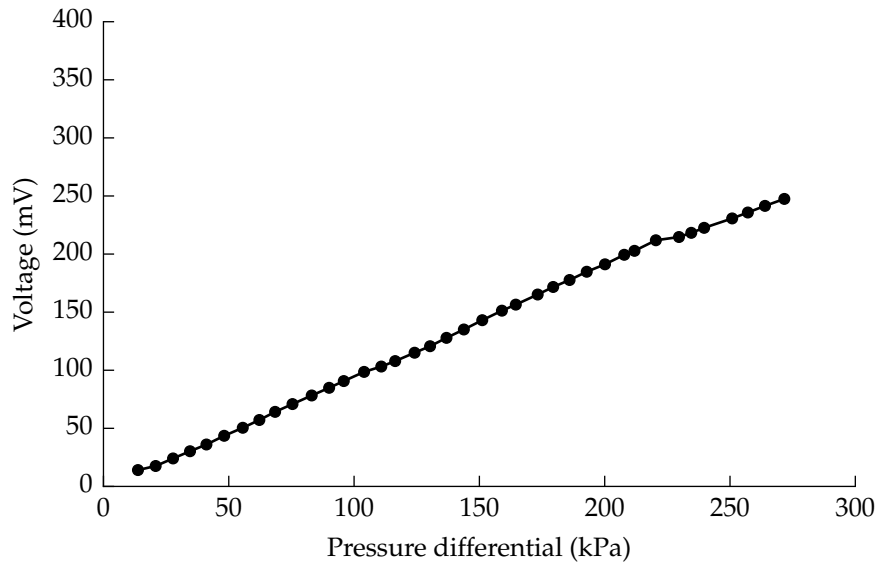


Figure B.5: Graph showing the voltage output with applied pressure differential across a 75 μm glass micro-channel (20 mV offset added)

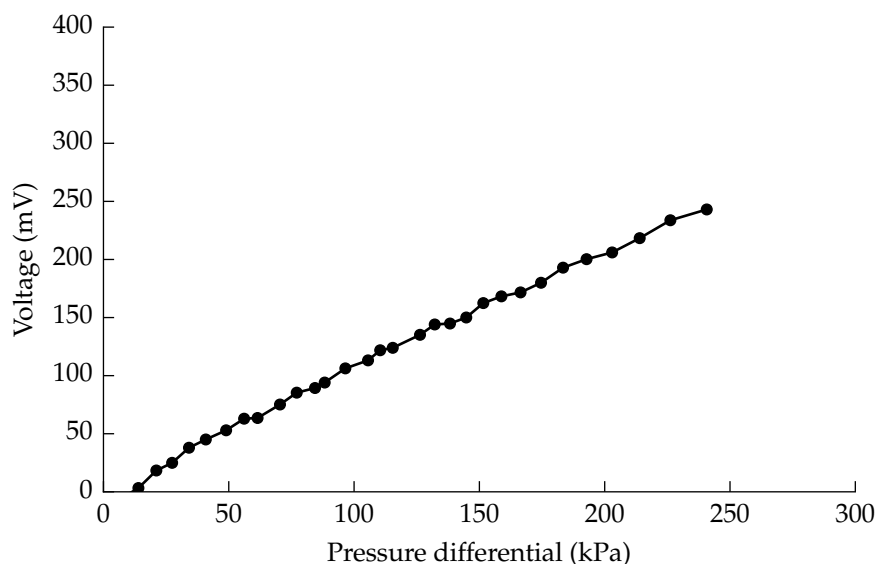


Figure B.6: Graph showing the voltage output with applied pressure differential across a 106 μm glass micro-channel (56 mV offset added)

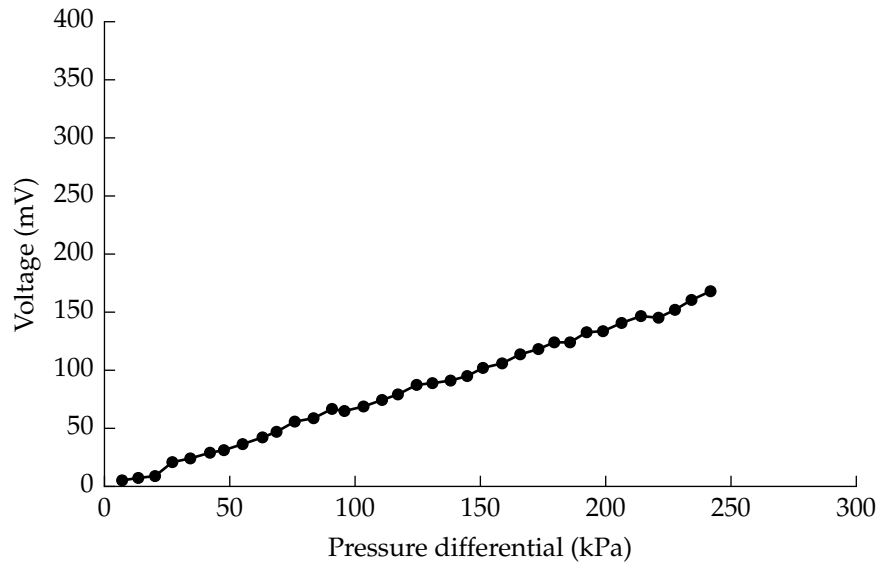


Figure B.7: Graph showing the voltage output with applied pressure differential across a 125 μm glass micro-channel (5 mV offset added)

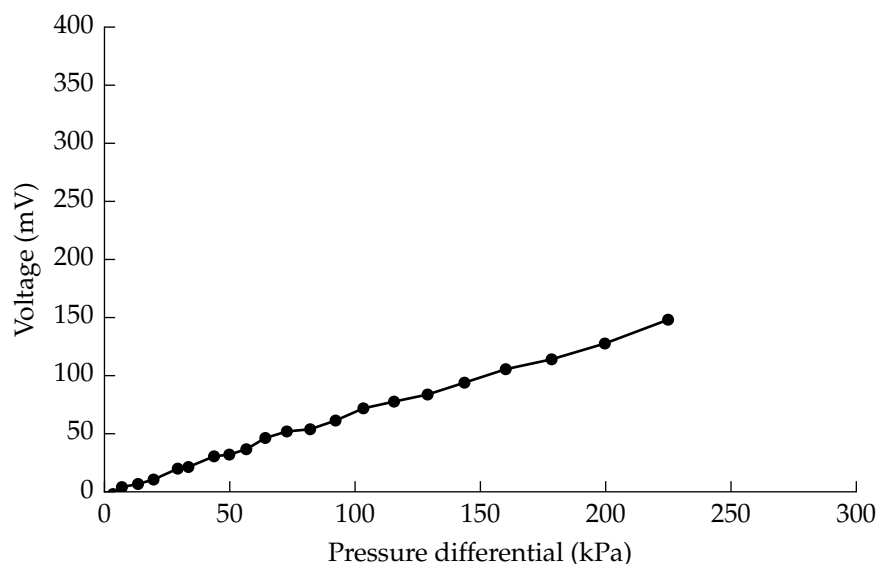


Figure B.8: Graph showing the voltage output with applied pressure differential across a 161 μm glass micro-channel (23 mV offset added)

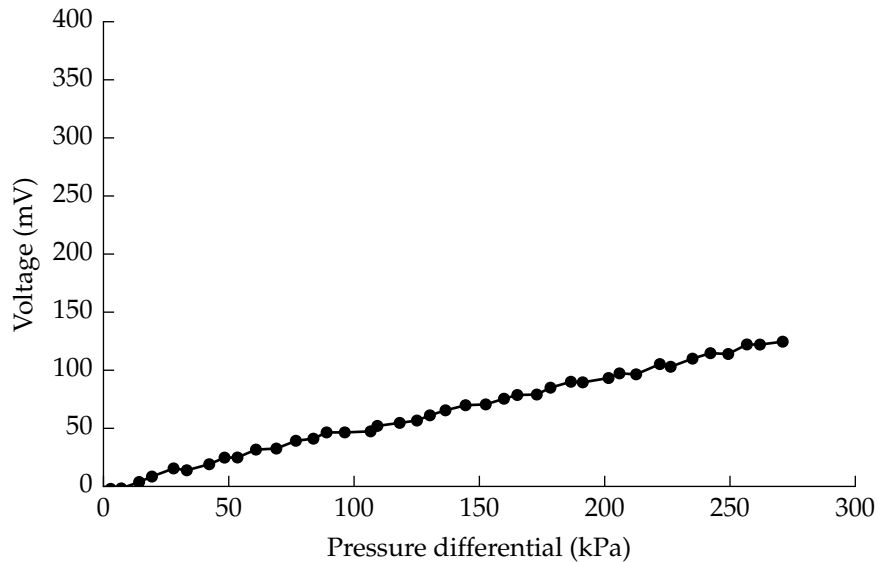


Figure B.9: Graph showing the voltage output with applied pressure differential across a 178 μm glass micro-channel (13 mV offset added)

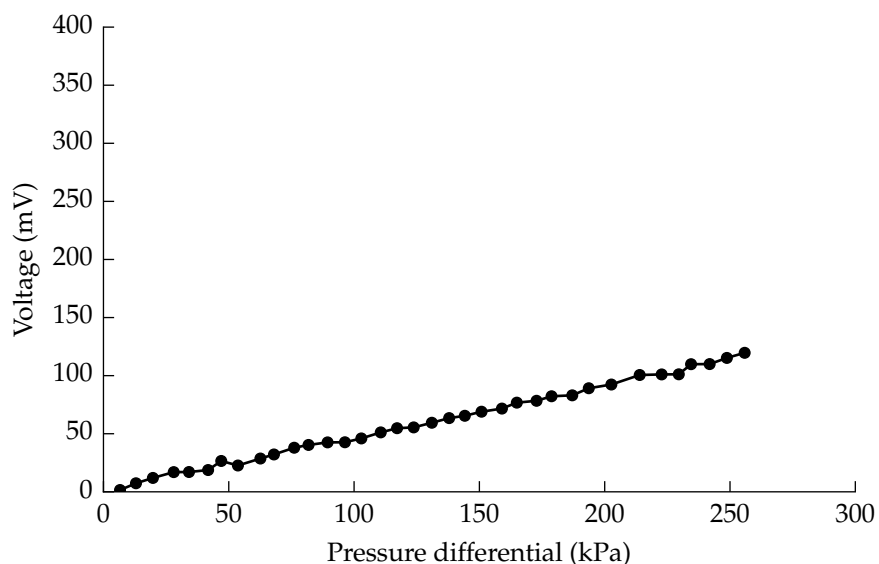


Figure B.10: Graph showing the voltage output with applied pressure differential across a 245 μm glass micro-channel (27 mV offset added)

Chapter C

Microprocessor Power Measurements

C.1 Measurement scripts

Energy consumption measurements were made using an Agilent E5270B 8-Slot Precision Measurement Mainframe, a Tektronix MSO 4054 Mixed Signal Oscilloscope and a desktop PC. Operation of the E5270 was done via GLIB interface using a USB connection and Agilent IO Libraries Version 16.0.1458.0. From here the machine was interfaced using custom Python scripts (appended) and PyVisa (available from <http://pyvisa.sourceforge.net/pyvisa/>).

C.1.1 E5270 Scripts

Measurement of chip energy consumption was carried out using the following measurement script. This script is written in Python and was executed using PyLab from the Enthought Python bundle.

C.2 Measurement data

It should be noted that the Freescale M9S08QG8 and the Microchip PIC16F1827 were unable to boot reliably into a low power state at 1.8V. To prevent this

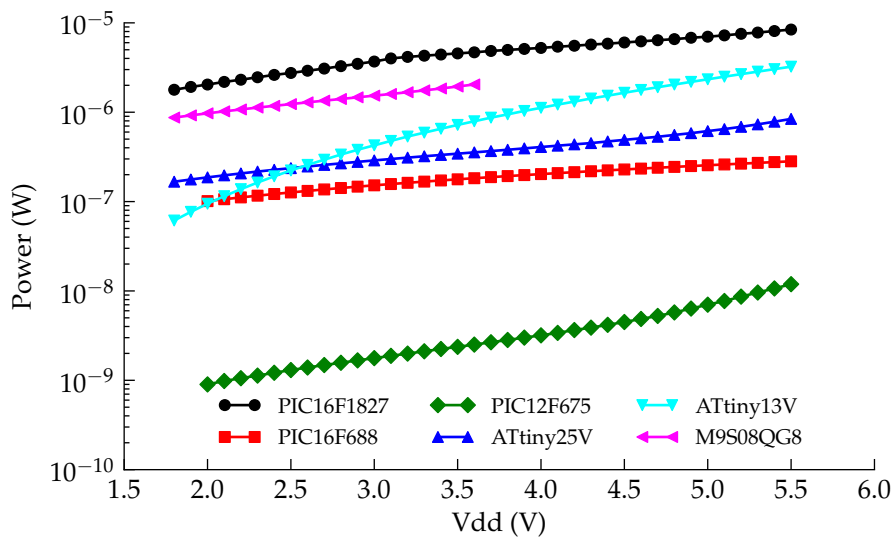


Figure C.1: Power usage of each microprocessor while in sleep mode

from happening the chips were booted at 2.0V and lowered to 1.8V to prevent the chips entering a state where current consumption was in the hundreds of microamps range.

C.2.1 Chips sleeping

The following tables list the unprocessed current measurements for a sweep of Vdd from 1.8V to 5.5V. Sweeps have been restricted to the input voltage ranges as specified in each chips datasheet.

Vdd	Tiny13V	Tiny25V	12F675	16F1827	M9S08QG8
1.80	3.41E-08	9.27E-08	N/A	9.914E-07	3.82E-04
1.90	4.04E-08	9.30E-08	N/A	1.008E-06	3.86E-04
2.00	4.73E-08	9.33E-08	4.497E-10	1.023E-06	4.88E-07
2.10	5.47E-08	9.36E-08	4.677E-10	1.038E-06	4.89E-07
2.20	6.26E-08	9.39E-08	4.797E-10	1.054E-06	4.91E-07
2.30	7.10E-08	9.42E-08	4.907E-10	1.068E-06	4.92E-07
2.40	7.99E-08	9.45E-08	5.057E-10	1.087E-06	4.94E-07
2.50	8.92E-08	9.47E-08	5.210E-10	1.102E-06	4.96E-07
2.60	9.90E-08	9.50E-08	5.347E-10	1.119E-06	4.99E-07
2.70	1.09E-07	9.53E-08	5.487E-10	1.137E-06	5.02E-07
2.80	1.20E-07	9.56E-08	5.610E-10	1.166E-06	5.05E-07
2.90	1.31E-07	9.59E-08	5.760E-10	1.195E-06	5.10E-07
3.00	1.42E-07	9.63E-08	5.903E-10	1.234E-06	5.15E-07
3.10	1.54E-07	9.66E-08	6.057E-10	1.290E-06	5.21E-07
3.20	1.67E-07	9.70E-08	6.217E-10	1.300E-06	5.28E-07
3.30	1.79E-07	9.74E-08	6.397E-10	1.301E-06	5.37E-07
3.40	1.92E-07	9.78E-08	6.590E-10	1.302E-06	5.47E-07
3.50	2.06E-07	9.82E-08	6.763E-10	1.301E-06	5.60E-07
3.60	2.20E-07	9.87E-08	6.970E-10	1.304E-06	5.75E-07
3.70	2.35E-07	9.93E-08	7.200E-10	1.307E-06	N/A
3.80	2.49E-07	1.00E-07	7.437E-10	1.309E-06	N/A
3.90	2.65E-07	1.01E-07	7.703E-10	1.311E-06	N/A
4.00	2.80E-07	1.02E-07	7.960E-10	1.312E-06	N/A
4.10	2.97E-07	1.03E-07	8.273E-10	1.317E-06	N/A
4.20	3.13E-07	1.04E-07	8.690E-10	1.319E-06	N/A
4.30	3.31E-07	1.05E-07	9.033E-10	1.330E-06	N/A
4.40	3.48E-07	1.07E-07	9.487E-10	1.334E-06	N/A
4.50	3.67E-07	1.09E-07	9.977E-10	1.342E-06	N/A
4.60	3.86E-07	1.11E-07	1.056E-09	1.351E-06	N/A
4.70	4.05E-07	1.13E-07	1.117E-09	1.360E-06	N/A
4.80	4.25E-07	1.16E-07	1.197E-09	1.373E-06	N/A
4.90	4.46E-07	1.19E-07	1.296E-09	1.385E-06	N/A
5.00	4.67E-07	1.23E-07	1.403E-09	1.401E-06	N/A
5.10	4.90E-07	1.27E-07	1.513E-09	1.422E-06	N/A
5.20	5.13E-07	1.32E-07	1.661E-09	1.445E-06	N/A
5.30	5.37E-07	1.38E-07	1.811E-09	1.469E-06	N/A
5.40	5.62E-07	1.45E-07	1.975E-09	1.497E-06	N/A
5.50	5.88E-07	1.53E-07	2.164E-09	1.529E-06	N/A

Table C.1: Raw sleep measurements (Vdd 1.8V – 5.5V)

Vdd	9.6 MHz	4.8 MHz	1.2 MHz	600 kHz	128 kHz	16 kHz
1.80	N/A	N/A	3.900E-04	2.148E-04	8.098E-05	5.393E-05
1.90	N/A	N/A	4.121E-04	2.258E-04	8.387E-05	5.499E-05
2.00	N/A	N/A	4.242E-04	2.329E-04	8.708E-05	5.608E-05
2.10	N/A	N/A	4.429E-04	2.421E-04	8.897E-05	5.721E-05
2.20	N/A	N/A	4.634E-04	2.523E-04	9.126E-05	5.839E-05
2.30	N/A	N/A	4.859E-04	2.632E-04	9.415E-05	5.964E-05
2.40	N/A	N/A	5.088E-04	2.748E-04	9.738E-05	6.099E-05
2.50	N/A	N/A	5.323E-04	2.865E-04	1.006E-04	6.214E-05
2.60	N/A	N/A	5.557E-04	2.984E-04	1.038E-04	6.396E-05
2.70	2.759E-03	1.664E-03	5.799E-04	3.108E-04	1.071E-04	6.560E-05
2.80	2.879E-03	1.742E-03	6.065E-04	3.235E-04	1.102E-04	6.743E-05
2.90	3.001E-03	1.834E-03	6.384E-04	3.366E-04	1.136E-04	6.926E-05
3.00	3.116E-03	1.945E-03	6.705E-04	3.540E-04	1.174E-04	7.100E-05
3.10	3.231E-03	2.022E-03	6.876E-04	3.582E-04	1.124E-04	6.809E-05
3.20	3.358E-03	2.109E-03	7.144E-04	3.710E-04	1.150E-04	6.878E-05
3.30	3.486E-03	2.199E-03	7.421E-04	3.843E-04	1.175E-04	6.996E-05
3.40	3.619E-03	2.295E-03	7.700E-04	3.979E-04	1.200E-04	7.115E-05
3.50	3.757E-03	2.394E-03	7.976E-04	4.114E-04	1.226E-04	7.235E-05
3.60	3.905E-03	2.491E-03	8.269E-04	4.251E-04	1.250E-04	7.354E-05

Table C.2: Atmel ATtiny13V clocking current (Vdd 1.8V – 3.6V).

Vdd	9.6 MHz	4.8 MHz	1.2 MHz	600 kHz	128 kHz	16 kHz
3.70	4.046E-03	2.580E-03	8.555E-04	4.392E-04	1.275E-04	7.471E-05
3.80	4.185E-03	2.661E-03	8.854E-04	4.535E-04	1.298E-04	7.706E-05
3.90	4.322E-03	2.740E-03	9.156E-04	4.685E-04	1.321E-04	7.701E-05
4.00	4.464E-03	2.822E-03	9.467E-04	4.834E-04	1.343E-04	7.814E-05
4.10	4.606E-03	2.900E-03	9.780E-04	4.990E-04	1.365E-04	7.929E-05
4.20	4.753E-03	2.932E-03	1.010E-03	5.152E-04	1.386E-04	8.045E-05
4.30	4.901E-03	2.991E-03	1.043E-03	5.313E-04	1.406E-04	8.163E-05
4.40	5.061E-03	3.001E-03	1.077E-03	5.491E-04	1.425E-04	8.283E-05
4.50	5.219E-03	2.987E-03	1.110E-03	5.655E-04	1.444E-04	8.406E-05
4.60	5.389E-03	3.073E-03	1.144E-03	5.833E-04	1.462E-04	8.531E-05
4.70	5.547E-03	3.162E-03	1.178E-03	6.002E-04	1.480E-04	8.661E-05
4.80	5.710E-03	3.257E-03	1.213E-03	6.216E-04	1.498E-04	8.795E-05
4.90	5.872E-03	3.348E-03	1.248E-03	6.395E-04	1.502E-04	8.932E-05
5.00	6.046E-03	3.443E-03	1.285E-03	6.567E-04	1.484E-04	9.072E-05
5.10	6.228E-03	3.548E-03	1.320E-03	6.746E-04	1.470E-04	9.213E-05
5.20	6.391E-03	3.647E-03	1.357E-03	6.940E-04	1.465E-04	9.346E-05
5.30	6.575E-03	3.753E-03	1.394E-03	7.134E-04	1.469E-04	9.482E-05
5.40	6.753E-03	3.857E-03	1.434E-03	7.331E-04	1.485E-04	9.640E-05
5.50	6.955E-03	3.970E-03	1.471E-03	7.526E-04	1.506E-04	9.818E-05

Table C.3: Atmel ATTiny13V clocking current (Vdd 3.7V – 5.5V).

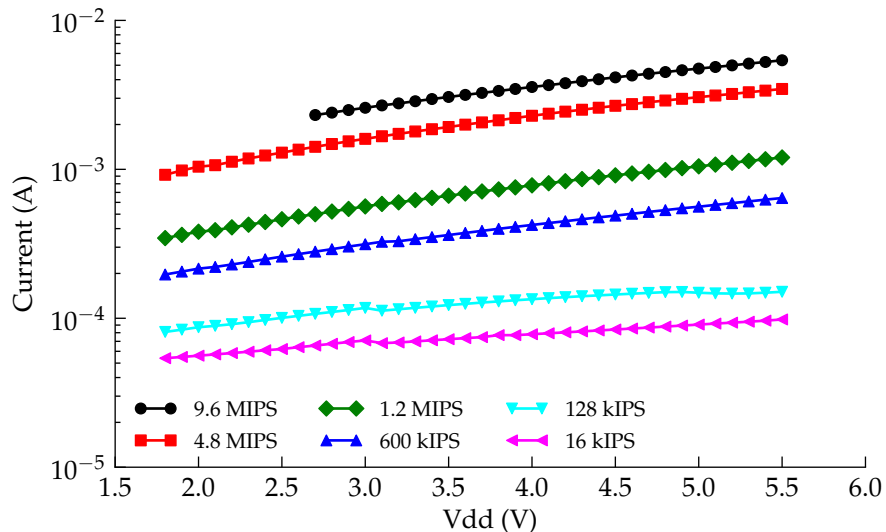


Figure C.2: Current consumption of the Atmel ATtiny13V while clocking

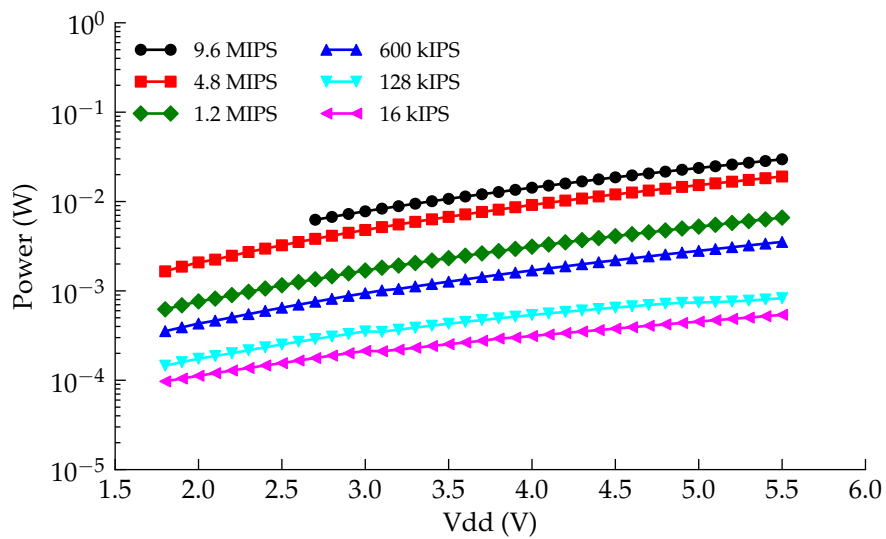


Figure C.3: Power consumption of the Atmel ATtiny13V while clocking

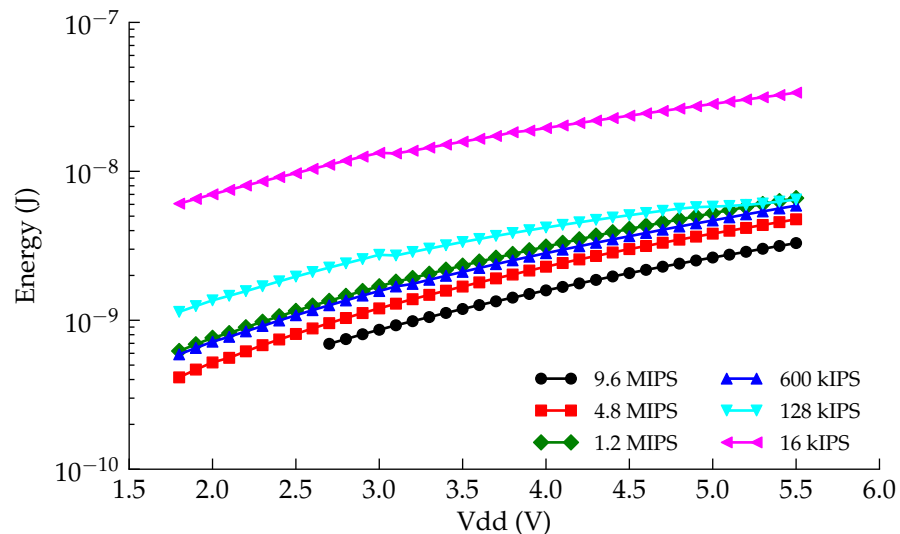


Figure C.4: Energy consumed per instruction for the Atmel ATtiny13V

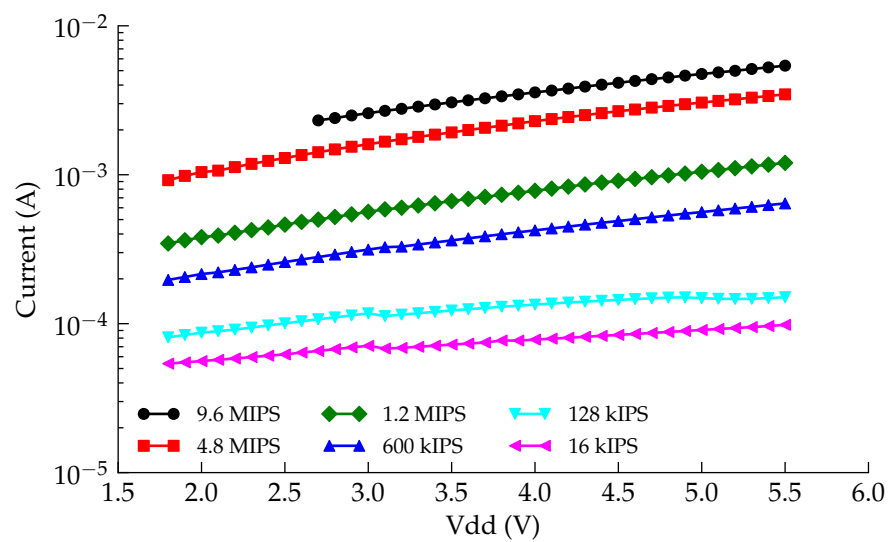


Figure C.5: Current consumption of the Atmel ATtiny25V while clocking

Vdd	16 MHz	8 MHz	6.4 MHz	2 MHz	1 MHz	800 kHz	128 kHz	16 kHz
1.80	N/A	N/A	N/A	1.148E-03	4.106E-04	1.146E-03	7.622E-05	1.666E-04
1.90	N/A	N/A	N/A	1.205E-03	4.319E-04	1.209E-03	7.858E-05	1.737E-04
2.00	N/A	N/A	N/A	1.261E-03	4.531E-04	1.274E-03	8.121E-05	1.813E-04
2.10	N/A	N/A	N/A	1.320E-03	4.754E-04	1.339E-03	8.464E-05	1.903E-04
2.20	N/A	N/A	N/A	1.378E-03	4.984E-04	1.404E-03	8.981E-05	1.994E-04
2.30	N/A	N/A	N/A	1.434E-03	5.195E-04	1.471E-03	9.486E-05	2.066E-04
2.40	N/A	N/A	N/A	1.491E-03	5.413E-04	1.537E-03	9.642E-05	2.126E-04
2.50	N/A	N/A	N/A	1.540E-03	5.671E-04	1.604E-03	9.903E-05	2.193E-04
2.60	N/A	N/A	N/A	1.597E-03	5.912E-04	1.671E-03	1.008E-04	2.257E-04
2.70	6.283E-03	3.124E-03	1.765E-03	1.651E-03	6.163E-04	1.740E-03	1.030E-04	2.320E-04
2.80	6.551E-03	3.256E-03	1.842E-03	1.706E-03	6.425E-04	1.811E-03	1.053E-04	2.378E-04
2.90	6.826E-03	3.392E-03	1.916E-03	1.766E-03	6.683E-04	1.883E-03	1.072E-04	2.414E-04
3.00	7.097E-03	3.537E-03	1.995E-03	1.832E-03	6.963E-04	1.959E-03	1.094E-04	2.434E-04
3.10	7.380E-03	3.682E-03	2.081E-03	1.906E-03	7.284E-04	2.050E-03	1.118E-04	2.440E-04
3.20	7.695E-03	3.825E-03	2.172E-03	1.973E-03	7.623E-04	2.131E-03	1.143E-04	2.469E-04
3.30	7.996E-03	3.975E-03	2.253E-03	2.036E-03	7.925E-04	2.210E-03	1.170E-04	2.521E-04
3.40	8.288E-03	4.122E-03	2.340E-03	2.101E-03	8.216E-04	2.286E-03	1.190E-04	2.587E-04
3.50	8.605E-03	4.271E-03	2.425E-03	2.165E-03	8.516E-04	2.371E-03	1.208E-04	2.657E-04
3.60	8.915E-03	4.421E-03	2.510E-03	2.230E-03	8.824E-04	2.452E-03	1.222E-04	2.732E-04

Table C.4: Atmel ATTiny25V clocking current (Vdd 3.7V – 5.5V)

Vdd	16 MHz	8 MHz	6.4 MHz	2 MHz	1 MHz	800 kHz	128 kHz	16 kHz
3.70	9.232E-03	4.582E-03	2.599E-03	2.298E-03	9.122E-04	2.535E-03	1.235E-04	2.805E-04
3.80	9.550E-03	4.754E-03	2.687E-03	2.365E-03	9.436E-04	2.622E-03	1.246E-04	2.867E-04
3.90	9.908E-03	4.921E-03	2.776E-03	2.436E-03	9.746E-04	2.706E-03	1.258E-04	2.950E-04
4.00	1.025E-02	5.077E-03	2.864E-03	2.506E-03	1.006E-03	2.795E-03	1.269E-04	2.951E-04
4.10	1.057E-02	5.245E-03	2.962E-03	2.578E-03	1.040E-03	2.882E-03	1.280E-04	3.015E-04
4.20	1.092E-02	5.422E-03	3.054E-03	2.652E-03	1.074E-03	2.970E-03	1.278E-04	3.085E-04
4.30	1.128E-02	5.607E-03	3.153E-03	2.724E-03	1.108E-03	3.062E-03	1.279E-04	3.159E-04
4.40	1.161E-02	5.783E-03	3.250E-03	2.795E-03	1.143E-03	3.155E-03	1.270E-04	3.235E-04
4.50	1.198E-02	5.958E-03	3.348E-03	2.873E-03	1.177E-03	3.248E-03	1.266E-04	3.313E-04
4.60	1.235E-02	6.139E-03	3.445E-03	2.949E-03	1.210E-03	3.340E-03	1.254E-04	3.390E-04
4.70	1.272E-02	6.312E-03	3.549E-03	3.027E-03	1.248E-03	3.430E-03	1.240E-04	3.468E-04
4.80	1.311E-02	6.501E-03	3.653E-03	3.105E-03	1.284E-03	3.528E-03	1.230E-04	3.547E-04
4.90	1.349E-02	6.689E-03	3.757E-03	3.190E-03	1.319E-03	3.633E-03	1.229E-04	3.625E-04
5.00	1.387E-02	6.898E-03	3.860E-03	3.270E-03	1.358E-03	3.732E-03	1.237E-04	3.703E-04
5.10	1.427E-02	7.099E-03	3.965E-03	3.356E-03	1.396E-03	3.832E-03	1.248E-04	3.781E-04
5.20	1.464E-02	7.302E-03	4.075E-03	3.437E-03	1.432E-03	3.931E-03	1.262E-04	3.857E-04
5.30	1.506E-02	7.502E-03	4.181E-03	3.527E-03	1.471E-03	4.033E-03	1.277E-04	3.930E-04
5.40	1.547E-02	7.713E-03	4.297E-03	3.616E-03	1.512E-03	4.142E-03	1.293E-04	3.999E-04
5.50	1.588E-02	7.908E-03	4.415E-03	3.705E-03	1.552E-03	4.245E-03	1.311E-04	4.063E-04

Table C.5: Atmel ATTiny25V clocking current (VDD 3.7V – 5.5V)

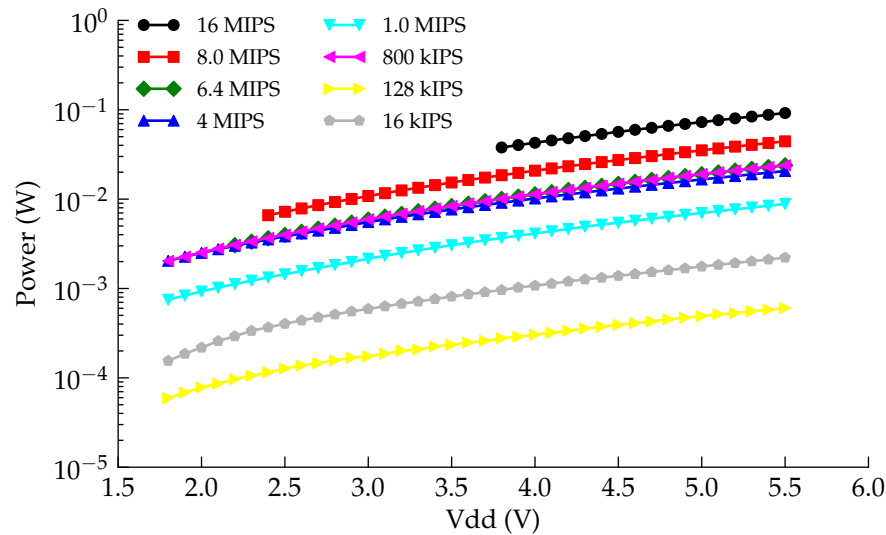


Figure C.6: Power consumption of the Atmel ATtiny25V while clocking

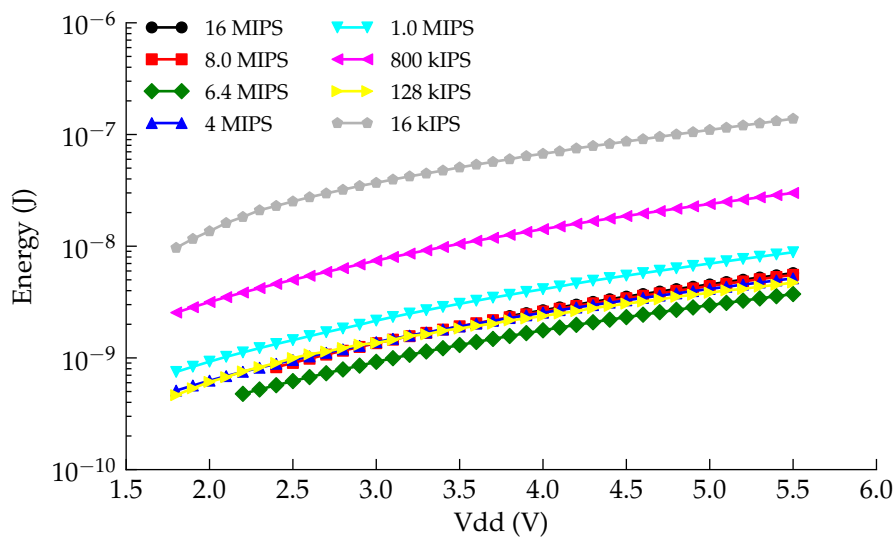


Figure C.7: Energy consumed per instruction for the Atmel ATtiny25V

Vdd	32 MHz	16 MHz	8 MHz	4 MHz	2 MHz	1 MHz	500 kHz	31 kHz
1.80	N/A	1.250E-03	8.043E-04	5.163E-04	3.912E-04	3.290E-04	1.322E-04	4.679E-06
1.90	N/A	1.322E-03	8.483E-04	5.391E-04	4.066E-04	3.405E-04	1.367E-04	4.892E-06
2.00	N/A	1.395E-03	8.930E-04	5.619E-04	4.220E-04	3.520E-04	1.402E-04	5.063E-06
2.10	N/A	1.468E-03	9.382E-04	5.848E-04	4.375E-04	3.637E-04	1.436E-04	5.307E-06
2.20	N/A	1.542E-03	9.841E-04	6.079E-04	4.528E-04	3.754E-04	1.471E-04	5.546E-06
2.30	N/A	1.620E-03	1.031E-03	6.310E-04	4.683E-04	3.870E-04	1.503E-04	5.796E-06
2.40	N/A	1.698E-03	1.078E-03	6.544E-04	4.838E-04	3.987E-04	1.535E-04	5.996E-06
2.50	2.711E-03	1.773E-03	1.126E-03	6.778E-04	4.996E-04	4.105E-04	1.567E-04	6.282E-06
2.60	2.826E-03	1.848E-03	1.172E-03	7.008E-04	5.150E-04	4.223E-04	1.599E-04	6.536E-06
2.70	2.939E-03	1.919E-03	1.214E-03	7.232E-04	5.301E-04	4.337E-04	1.631E-04	6.734E-06
2.80	3.050E-03	1.990E-03	1.255E-03	7.456E-04	5.450E-04	4.449E-04	1.662E-04	6.912E-06
2.90	3.163E-03	2.062E-03	1.297E-03	7.685E-04	5.605E-04	4.565E-04	1.695E-04	7.109E-06
3.00	3.277E-03	2.134E-03	1.338E-03	7.916E-04	5.758E-04	4.683E-04	1.728E-04	7.349E-06
3.10	3.391E-03	2.207E-03	1.380E-03	8.152E-04	5.917E-04	4.802E-04	1.763E-04	7.534E-06
3.20	3.507E-03	2.281E-03	1.422E-03	8.388E-04	6.074E-04	4.919E-04	1.797E-04	7.601E-06
3.30	3.623E-03	2.355E-03	1.465E-03	8.626E-04	6.235E-04	5.039E-04	1.829E-04	7.604E-06
3.40	3.445E-03	2.263E-03	1.438E-03	8.666E-04	6.386E-04	5.273E-04	1.940E-04	7.638E-06
3.50	3.445E-03	2.263E-03	1.439E-03	8.663E-04	6.390E-04	5.276E-04	1.942E-04	7.582E-06
3.60	3.447E-03	2.264E-03	1.439E-03	8.663E-04	6.389E-04	5.275E-04	1.943E-04	7.616E-06

Table C.6: Microchip PIC16F1827 clocking current (Vdd 0V – 3.6V)

Vdd	32 MHz	16 MHz	8 MHz	4 MHz	2 MHz	1 MHz	500 kHz	31 kHz
3.70	3.449E-03	2.265E-03	1.439E-03	8.663E-04	5.277E-04	1.945E-04	7.617E-06	
3.80	3.449E-03	2.265E-03	1.440E-03	8.665E-04	6.393E-04	5.279E-04	1.947E-04	7.649E-06
3.90	3.450E-03	2.265E-03	1.440E-03	8.667E-04	6.397E-04	5.283E-04	1.950E-04	7.603E-06
4.00	3.451E-03	2.267E-03	1.441E-03	8.669E-04	6.396E-04	5.283E-04	1.952E-04	7.634E-06
4.10	3.452E-03	2.267E-03	1.441E-03	8.672E-04	6.401E-04	5.286E-04	1.955E-04	7.633E-06
4.20	3.453E-03	2.268E-03	1.442E-03	8.673E-04	6.401E-04	5.286E-04	1.957E-04	7.667E-06
4.30	3.454E-03	2.269E-03	1.442E-03	8.675E-04	6.404E-04	5.290E-04	1.960E-04	7.620E-06
4.40	3.454E-03	2.269E-03	1.443E-03	8.679E-04	6.405E-04	5.293E-04	1.961E-04	7.660E-06
4.50	3.456E-03	2.270E-03	1.443E-03	8.681E-04	6.410E-04	5.294E-04	1.964E-04	7.663E-06
4.60	3.457E-03	2.271E-03	1.444E-03	8.684E-04	6.412E-04	5.297E-04	1.966E-04	7.704E-06
4.70	3.458E-03	2.271E-03	1.444E-03	8.687E-04	6.416E-04	5.300E-04	1.969E-04	7.664E-06
4.80	3.458E-03	2.272E-03	1.445E-03	8.690E-04	6.417E-04	5.303E-04	1.972E-04	7.710E-06
4.90	3.460E-03	2.273E-03	1.446E-03	8.692E-04	6.421E-04	5.307E-04	1.976E-04	7.721E-06
5.00	3.461E-03	2.274E-03	1.446E-03	8.695E-04	6.424E-04	5.310E-04	1.979E-04	7.757E-06
5.10	3.463E-03	2.275E-03	1.447E-03	8.697E-04	6.428E-04	5.314E-04	1.983E-04	7.733E-06
5.20	3.464E-03	2.276E-03	1.448E-03	8.699E-04	6.433E-04	5.319E-04	1.986E-04	7.762E-06
5.30	3.465E-03	2.277E-03	1.448E-03	8.703E-04	6.437E-04	5.326E-04	1.991E-04	7.797E-06
5.40	3.467E-03	2.278E-03	1.449E-03	8.708E-04	6.444E-04	5.332E-04	1.996E-04	7.777E-06
5.50	3.468E-03	2.279E-03	1.450E-03	8.711E-04	6.449E-04	5.336E-04	2.002E-04	7.833E-06

Table C.7: Microchip PIC16F1827 clocking current (Vdd 3.7V – 5.5V)

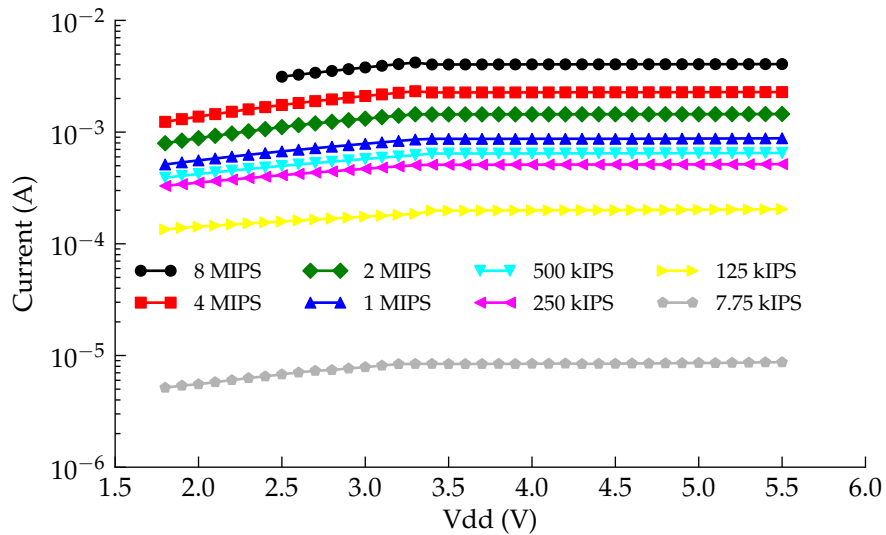


Figure C.8: Current consumption of the Microchip PIC16F1827 while clocking

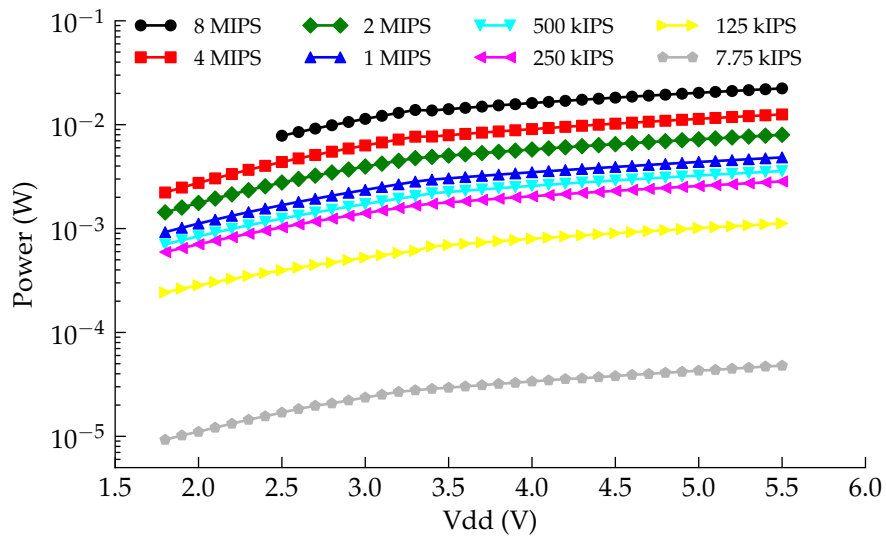


Figure C.9: Power consumption of the Microchip PIC16F1827 while clocking

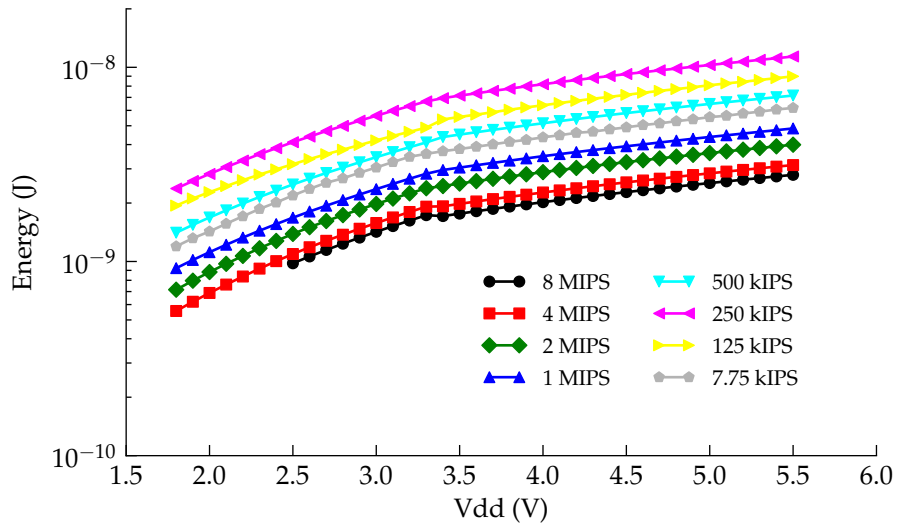


Figure C.10: Energy consumed per instruction for the Microchip PIC16F1827

C.2.2 Clocking

ATtiny13V

ATtiny25V

Microchip PIC16F1827

C.3 Microprocessor Test Code

C.3.1 ATMEL ATtiny13V and ATtiny25

Code was written in AVRStudio 4.18 (build 684) and compiled using WinAVR (AVR-GCC compiler for windows available from <http://winavr.sourceforge.net/>). Chip programming was done using an Atmel AVR STK500 demonstration board with serial interface.

Sleep

Programming fuses were all disabled (Watchdog, brown-out detect, clock divider) and clock selection was set to 'Int. RC Osc 128kHz; Start-up time; 14 CK + 0ms'

```

1 #include <avr/io.h>
2
3 int main(void)
4 {
5     //POWER REDUCTION TIPS:
6     // * Disable DWEN fuse
7     // * Disable BODLEVEL fuse
8
9     //Disable interrupts
10    SREG = 0x00;
11
12    //Set PortB as outputs
13    DDRB = 0b00000000;
14
15    //Disable analog comparitor
16    ACSR = 0x80;
17
18    //Disable digital input
19    DIDR0 = 0xFF;
20
21    //Disable ADC before sleep
22    ADCSRA = 0x00;
23
24    //Set GPIOs as high
25    PORTB = 0xFF;
26
27    //Sequence to disable brown-
28    //out detect while sleeping

```

```
29     MCUCR = 0b00110000;  
30  
31     while (1)  
32     {  
33         asm("sleep");  
34     }  
35 }
```

Listing C.1: ATtiny25V Sleep Procedure

Clocking

```
1 #include <avr/io.h>  
2  
3 int main(void)  
4 {  
5     unsigned char rand;  
6     SREG = 0x00;  
7     //Set PortB as outputs  
8     DDRB = 0b11111111;  
9     //Set pins high  
10    PORTB = 0xFF;  
11    for (;;) {  
12        rand++;  
13        asm("nop");  
14    }  
15}  
16  
17}
```

Listing C.2: ATtiny25V Clocking Procedure

C.3.2 Microchip 12F675

Code was written in MPLAB v8.6 in C and compiled using HI-TECH C v9.60. Chip programming was done using PICkit 2 Programmer software v2.61.¹

Sleep

C.3.3 Microchip 16F1827

Code written in MPLAB v8.6 in C and compiled using HI-TECH C v 9.60. Chip programming was done using PICkit 2 Programmer software v2.61, however in order to program the 16F1827 with the PICkit 2 programmer a patch was applied to the device file list. This patch was retrieved from <http://www.uploadarchief.net/files/download/pk2patch16x.zip> on the 12th May 2011.

Sleep

The specified sleep current of 30nA was not achievable. In an attempt to reach the specified current, the program was written in assembler. The assembler version of the code was used in the measurement data. The assembler version gave a lower sleep current than the C version, probably not as a result of the compiler but as due to a more thorough initialisation routine.

```

1 #include <htc.h>
2
3 _CONFIG(FOSC_INTOSC & WDTE_OFF & MCLRE_OFF & PWRTE_OFF
4   & BOREN_OFF & FCMEN_OFF & IESO_OFF & CLKOUTEN_OFF
5   & CP_OFF & CPD_OFF & LVP_ON & BORV_19 & STVREN_ON

```

¹Downloading to the 12F675s with MPLAB led to corruption of the internal oscillators, causing them fail.

```
6  & PLLEN_OFF & WRT_OFF);  
7  
8  
9 void main(void)  
10 {  
11     //Set system clock to Internal osc block  
12     SCS0 = 0;  
13     SCS1 = 1;  
14  
15     //Set internal osc freq = 31kHz  
16     IRCF3 = 0;  
17     IRCF2 = 0;  
18     IRCF1 = 0;  
19     IRCF0 = 0;  
20  
21     //Disable interrupts  
22     GIE = 0;  
23  
24     //Set all pins high (Tied to VDD via 10k)  
25     PORTA = 0xFF;  
26     PORTB = 0xFF;  
27  
28     //Put to sleep  
29     SLEEP();  
30     while(1)  
31     {  
32  
33     }  
34 }
```

Listing C.3: 16F1827 Sleep Procedure - HI-TECH C version

```
1 LIST    P=PIC16F1827  
2 #include <P16F1827.INC>
```

```

3
4  _CONFIG _CONFIG1 , _FOSC_INTOSC & _WDTE_OFF & _PWRTE_OFF &
   _MCLRE_OFF & _CP_OFF & _CPD_OFF & _BOREN_OFF & _CLKOUTEN_OFF
   & _IESO_OFF & _FCMEN_OFF
5  _CONFIG _CONFIG2 , _WRT_OFF & _PLLEN_OFF & _STVREN_OFF &
   _BORV_19 & _LVP_ON
6
7
8 ORG 0x0000 ; Specifies where to place the following code (which in
   this case is at the beginning of memory space )
9
10 START
11 ; Disable interrupts
12 BANKSEL INTCON
13 CLRF INTCON
14 ; Disable watchdog
15 BANKSEL WDICON
16 CLRF WDICON
17 ; Disable capacitive sensing
18 BANKSEL CPSCON0
19 CLRF CPSCON0
20 ; Disable modulation control
21 BANKSEL MDCON
22 CLRF MDCON
23 ; Disable perhiperal interrupts
24 BANKSEL PIE1
25 CLRF PIE2
26 ; Disable timer 1
27 BANKSEL T1CON
28 CLRF T1CON
29 ; Disable DAC
30 BANKSEL DACCON0
31 CLRF DACCON0

```

```
32 ; Disable ADC
33 BANKSEL ADCON0
34 CLRF ADCON0
35 BANKSEL ADCON1
36 CLRF ADCON1
37 ; Disable timers
38 BANKSEL T2CON
39 CLRF T2CON
40 BANKSEL T4CON
41 CLRF T4CON
42 BANKSEL T6CON
43 CLRF T6CON
44 ; Init PortA
45 BANKSEL PORTA ;
46 CLRF PORTA ;Init PORTA
47 BANKSEL LATA ;Data Latch
48 CLRF LATA ;
49 COMF LATA ;
50 BANKSEL ANSELA ;
51 CLRF ANSELA ;digital I/O
52 BANKSEL TRISA ;
53 CLRF TRISA ;SET AS OUTPUT
54 ;Init PortB
55 BANKSEL PORTB ;
56 CLRF PORTB ;Init PORTB
57 BANKSEL LATB
58 CLRF LATB ;
59 COMF LATB ;
60 BANKSEL ANSELB
61 CLRF ANSELB ;Make RB<7:0> digital
62 BANKSEL TRISB ;
63 ;and RB<3:0> as outputs
64 CLRF TRISB ;
```

```

65
66 LOOP ; Label this position (forms the start of a loop)
67 SLEEP
68 GOTO LOOP
69 END

```

Listing C.4: 16F1827 Sleep Procedure - MPASM assembler version

Clocking

```

1 #include <htc.h>
2
3 __CONFIG(FOSC_INTOSC & WDTE_OFF & MCLRE_OFF & PWRTE_OFF
4   & BOREN_OFF & FCMEN_OFF & IESO_OFF & CLKOUTEN_OFF
5   & CP_OFF & CPD_OFF & LVP_ON & BORV_19 & STVREN_ON
6   & PLLEN_ON & WRT_OFF);
7
8 unsigned int count;
9
10 void main(void)
11 {
12   //Set system clock to Internal osc block
13   SCS0 = 0;
14   SCS1 = 0;
15
16   //Set internal osc freq = 31kHz
17   IRCF3 = 1;
18   IRCF2 = 1;
19   IRCF1 = 1;
20   IRCF0 = 0;
21
22   //Disable interrupts
23   GIE = 0;
24

```

```
25 //Disable serial ports
26 SSP1CON1 = 0x00;
27 SSP2CON1 = 0x00;
28
29 ADCON0 = 0x00;
30
31 //Disable modulation
32 MDSRC = 0b10000000;
33 MDCARH = 0b10000000;
34 MDCARL = 0b10000000;
35
36 //Add pins as outputs
37 TRISA = 0x00;
38 ANSELA = 0x00;
39 TRISB = 0x00;
40 ANSELB = 0x00;
41
42 //Set all pins high (Tied to VDD via 10k)
43 PORTA = 0xFF;
44 PORTB = 0xFF;
45
46 //Put to sleep
47 while(1)
48 {
49     count++;
50 }
51 }
```

Listing C.5: PIC16F1827 Clocking Procedure

C.3.4 Freescale M9S08QG8

Code was written using Freescale's bundled IDE, CodeWarrior v5.90, and downloaded using a supplied USB demo board (DEMO9S08QG8E).

Sleep

```

1 #include <hidef.h> /* for EnableInterrupts macro */
2 #include "derivative.h" /* include peripheral declarations */
3
4 void main(void) {
5
6
7     SOPT1 = 0b00100000;
8     //      |||   ||
9     //      |||   \-- RESET Pin Enable (0)
10    //      |||   \-- Background Debug Mode Pin Enable (1)
11    //      ||\----- Stop Mode Enable (0)
12    //      |\----- COP Watchdog Timeout (1)
13    //      \----- COP Watchdog Enable (1)
14
15    //Enable low power bit
16    ICSC2 = 0b01001000;
17
18    //Disable Low Voltage Detect
19    SPMSC1 = 0x00;
20
21    //Enable power down control
22    //Disable partial power down
23    SPMSC2 = 0x02;
24
25    for (;;)
26    {
27        //Enter sleep mode

```

```
28     _Stop;  
29 }  
30 }
```

Listing C.6: M9S08QG8 Sleep Procedure

Chapter D

Solution Impedance Measurement

This section contains supplementary data to the measurements made in chapter 9. It details some of the testing done to ensure that the measurement setup was providing expected results, and test the electrodes for defects. It also contains measurements not presented in the thesis body. They have been included purely for interests sake.

D.1 Measurement Testing

Due to the impedance drop at low frequencies that was encountered when measuring the various solutions presented in chapter 9, some testing of the measurement setup was done. Figure D.1 shows the configuration used to test the electrode. The electrodes were included to determine whether they themselves were contributing to the impedance magnitude drop at low frequency.

D.1.1 Electrode array measuring resistors

Figures D.2 and D.3 show that the measurement setup *is* capable of measuring a target $10\text{ k}\Omega$ resistance placed between electrode 1 and 2. These measurements include the electrode array in the loop so any effect from the

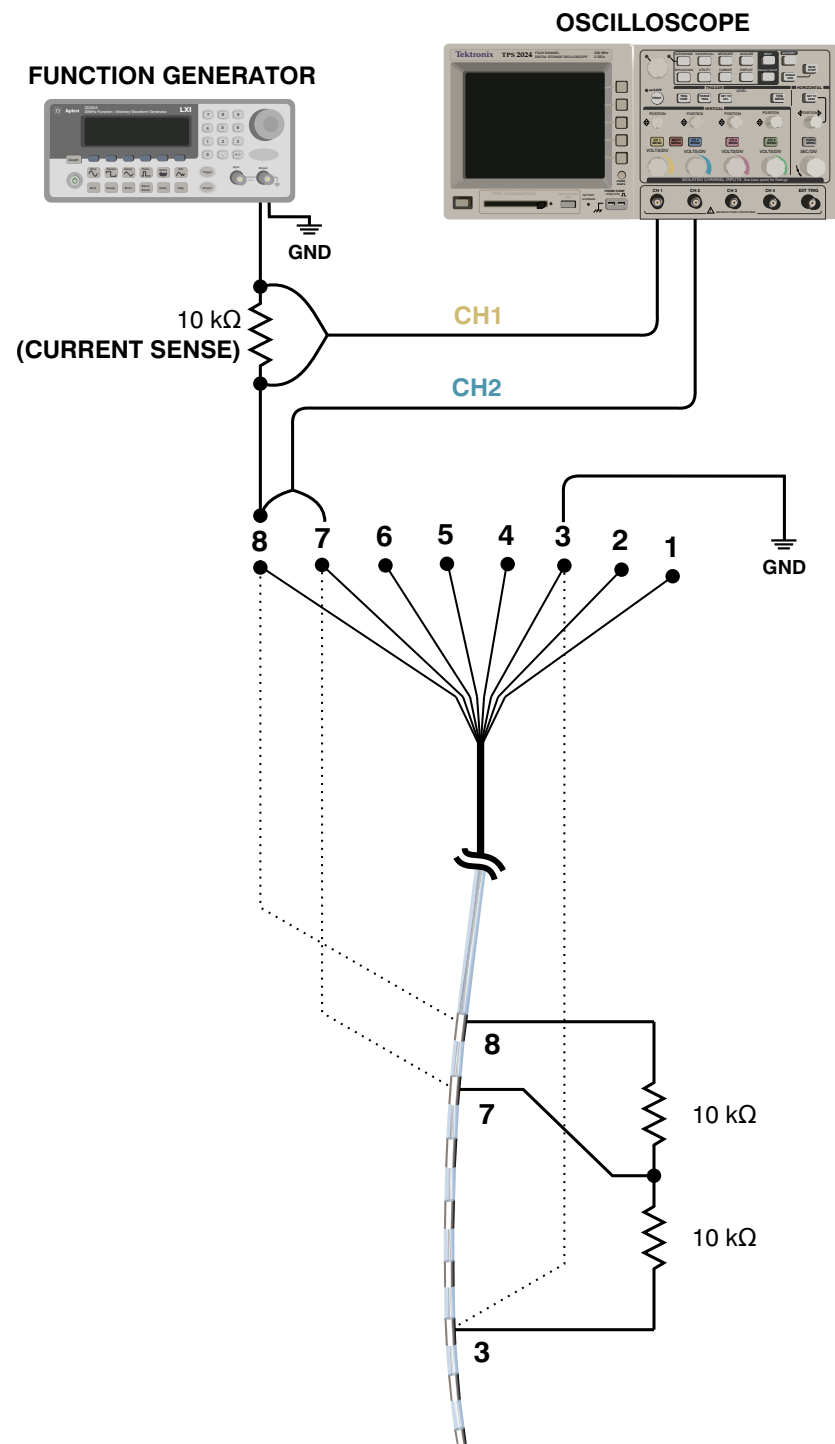


Figure D.1: Diagram showing the instruments and electrode configuration used to test the measurement setup.

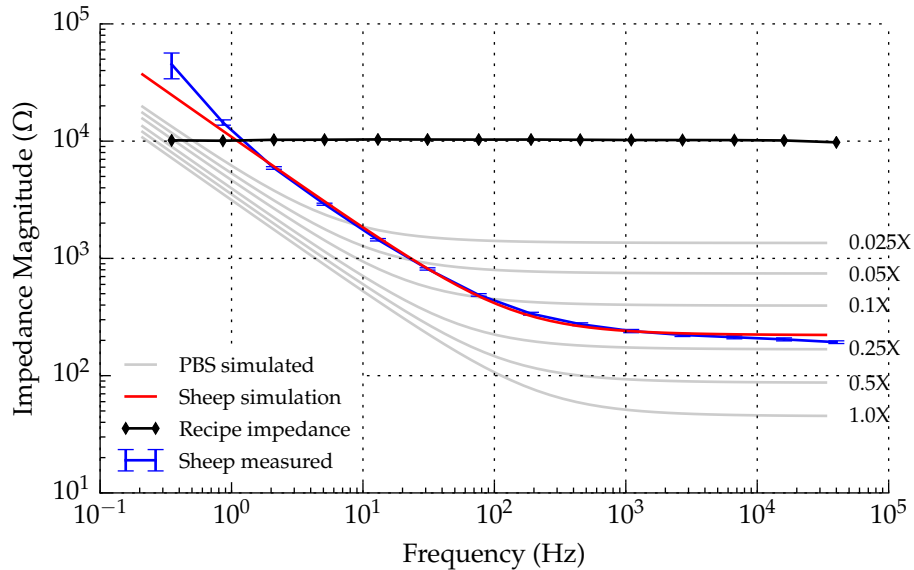


Figure D.2: Plot of impedance magnitude versus frequency (log-log) for a $10\text{ k}\Omega$ resistor placed between electrodes 1 and 2, and another $10\text{ k}\Omega$ resistor placed between electrodes 2 and 5.

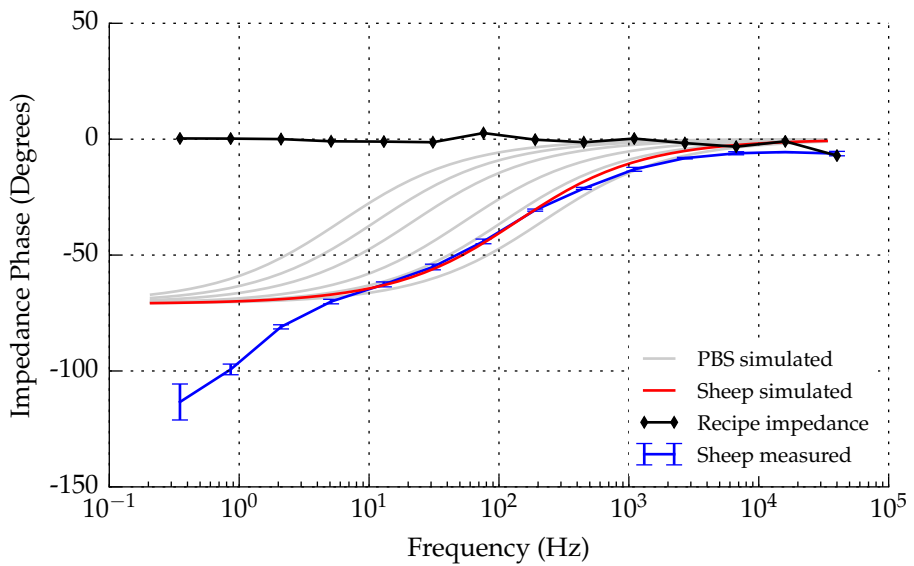


Figure D.3: Plot of impedance phase versus frequency (log-log) for a $10\text{ k}\Omega$ resistor placed between electrodes 1 and 2, and another $10\text{ k}\Omega$ resistor placed between electrodes 2 and 5.

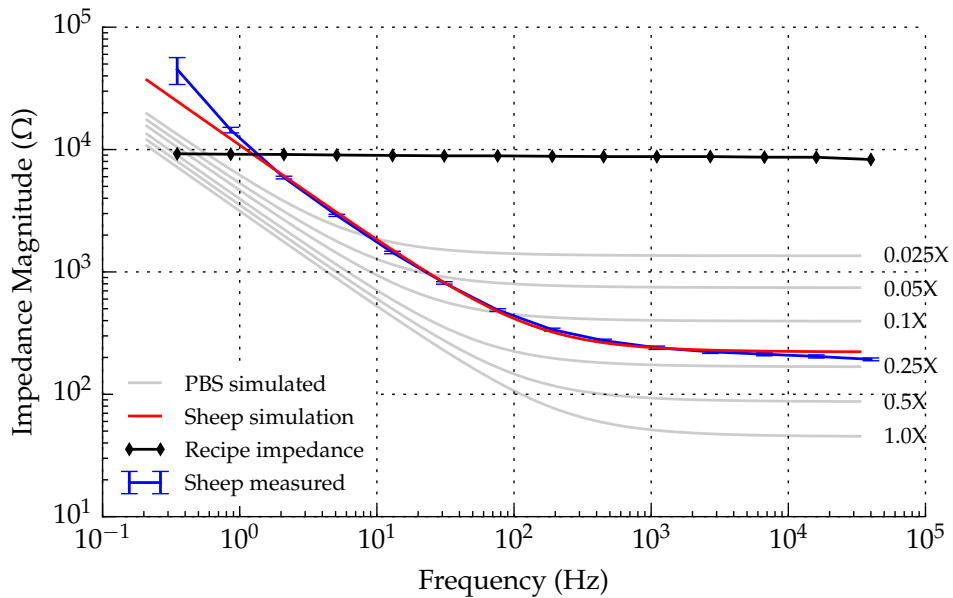


Figure D.4: Plot of impedance magnitude versus frequency (log-log) for a $10\text{ k}\Omega$ resistor placed between electrodes 1 and 2, and another $10\text{ k}\Omega$ resistor placed between electrodes 2 and 5. The electrodes and resistors are submerged in distilled water.

internal wiring will be evident here.

D.1.2 Electrode array submerged in distilled water measuring resistors

Figures D.4 and D.5 show the effect of submerging the electrode array in liquid. The resistors from the previous test are still in place, and therefore are also submerged. The resistance has dropped slightly, as expected, but no impedance deviation at low frequency is evident. This rules out the possibility of a wet electrode array having an effect on the measurement results due to leakage.

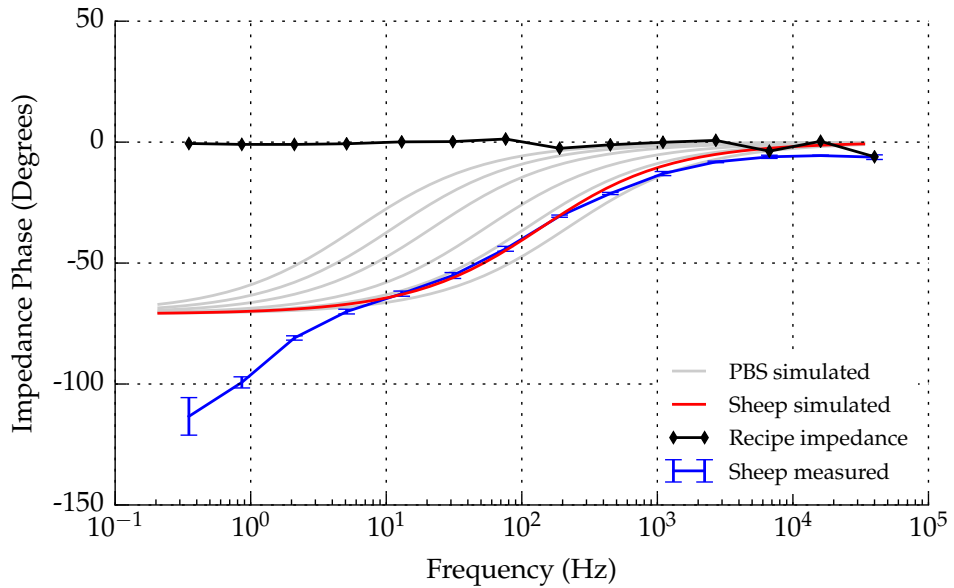


Figure D.5: Plot of impedance phase versus frequency (log-log) for a $10\text{ k}\Omega$ resistor placed between electrodes 1 and 2, and another $10\text{ k}\Omega$ resistor placed between electrodes 2 and 5. The electrodes and resistors are submerged in distilled water.

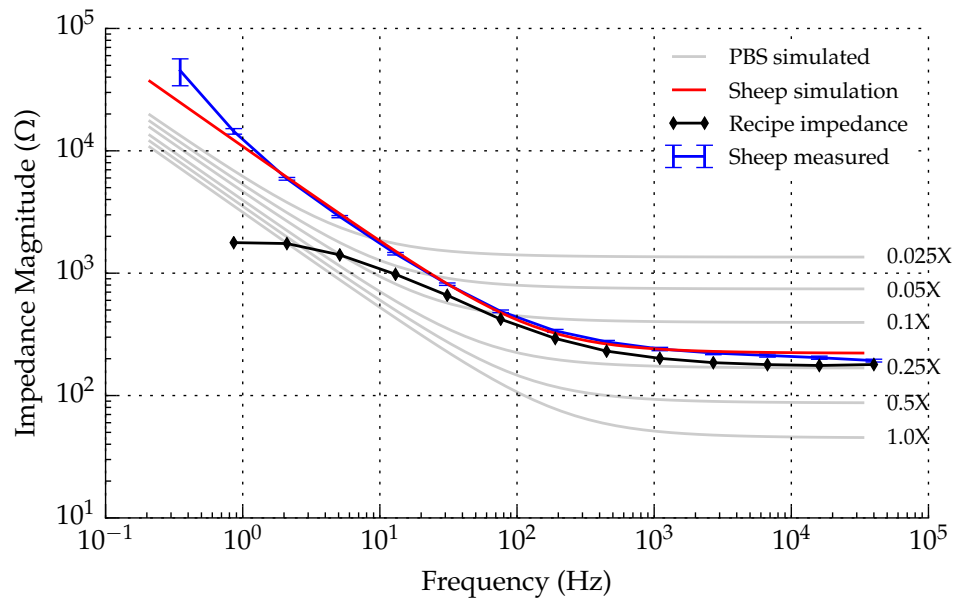


Figure D.6: Plot of impedance magnitude versus frequency (log-log) for a $10\text{ k}\Omega$ resistor placed between electrodes 1 and 2, and another $10\text{ k}\Omega$ resistor placed between electrodes 2 and 5. The electrodes and resistors are submerged in saline.

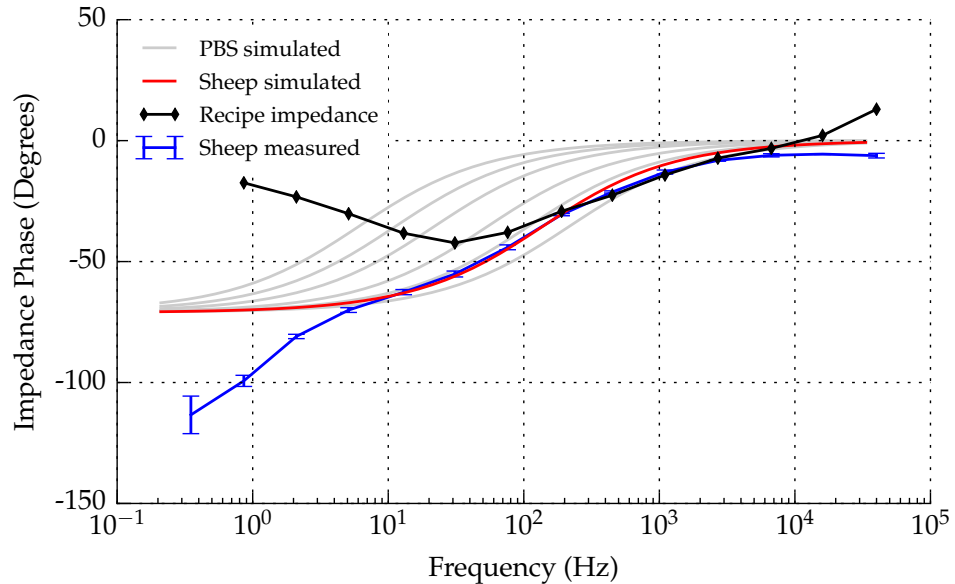


Figure D.7: Plot of impedance phase versus frequency (log-log) for a $10\text{ k}\Omega$ resistor placed between electrodes 1 and 2, and another $10\text{ k}\Omega$ resistor placed between electrodes 2 and 5. The electrodes and resistors are submerged in saline.

D.1.3 Electrode array submerged in saline measuring resistors

Figures D.6 and D.7 shows the effect of adding salt to the solution. That the characteristic impedance drop at low frequencies is evident. This result adds weight to the theory that it is ions in the solution that is responsible for the impedance magnitude drop at low frequency.

Newspaper Article on Streaming Cells

NEWS

HAMILTON PRESS, FEBRUARY 29, 2012 13

Making smart meters smarter still

By GEOFF LEWIS

COMMERCIAL interest is already appearing following news of research being undertaken at Waikato University focused on a self-powered water metering device.

The work is the focus of a PhD project undertaken by Mark Jones assisted by second year Bachelor of Science student Wayne Crump and is titled "The design and viability of a power harvesting wireless smart water meter".

Accurate water metering is becoming increasingly important for local authorities due to the huge costs of providing reticulated drinkable water.

Mr Jones said most existing meters worked on a mechanical principle and had to be read by council staff or contractors.

More modern "smart" meters used batteries and transmitted their data back to a collection point by way of mobile phone networks, he said.

These work in areas accessible to the cellular system.

However, the device Mr Jones is working on is called a "streaming potential cell" and makes use of an effect where water passing through a small glass tube naturally creates a current.

This current can then be used to read and transmit data produced by a mechanical system.

The device, using existing parts, is cheap to produce and allows data to be remotely read. It also removes the need for batteries and the waste caused by the disposal of spent cells.

One downside of the new technology is that it only reports water flow when the water is running and, as a result, may be less effective in gauging water loss due to leaks in the system.

Mr Jones, who is supervised by electronics professor Jonathan Scott, said there had already been three inquiries from organisations interested in the outcome of the research.

Photo: GEOFF LEWIS

IMPORTANT RESEARCH: Waikato University electronics PhD student Mark Jones with prototype electricity generators which could be used to read water meters.



ADVERTISEMENT

Big news for the Waikato

Ven-lu-ree, New Zealand's leading window coverings manufacturer and supplier now in the Waikato!



Ben & Rose Vivian - "Your local Ven-lu-ree specialist"

After spending over 7 years living in Christchurch, Ben and Rose Vivian and their three young children have returned home to the North Island to embark on a new venture serving the North Waikato area with Ven Lu Ree (established 1966) specialists in blinds, curtains, shutters, awnings, screens and security doors.

The earthquakes certainly unsettled their plans and the decision was made to come back to the Waikato. The question was - to do what? How could they find a role or a business to potentially involve both of them, capitalising on their combined strengths and experience?

Ven Lu Ree was the perfect answer to that question. Bens practicality and ability to provide clients with tailored solutions, combined with Rose's creativity and interior design expertise makes for a winning combination. They

know that the right solution and good value for money is what's important to people - because it's important to them too! Ven Lu Ree offers a top quality product across its wide range and has a fantastic reputation for being a company who will go the distance to satisfy their customers.

Now with fantastic discount offers and 12 months interest free terms there has never been a better time to look at window coverings.

So call us today on 0800 836 587

and we'll come to you

and save with our introductory offer of up to
35% off blinds, curtains, awnings and screens.

**VEN
LU
REE**

For a Limited
Time Only

**35%
OFF
BLINDS**

**PLUS
12 Months
Interest
FREE**

0800 836 587
Blinds • Curtains • Screens
• Security • Awnings • Shutters

45%

Figure D.8: Cut-out from the local newspaper (Hamilton Press) of an article on the streaming cell research conducted during this thesis.

Notes

The text width of this thesis is 360.0pt.

The text height of this thesis is 595.80026pt.

Bibliography

- [1] Atmel Corporation. ATtiny13. Technical Datasheet, 2010. 5.1.2
- [2] Atmel Corporation. ATtiny25/25V/45/45V/85/85V, 2010. 5.1.2
- [3] Allen J. Bard, Hector D. Abruna, Chris E. Chidsey, Larry R. Faulkner, Stephen W. Feldberg, Kingo Itaya, Marcin Majda, Owen Melroy, and Royce W. Murray. The electrode/electrolyte interface - a status report. *The Journal of Physical Chemistry*, 97(28):7147–7173, 1993. (document), 2.13
- [4] Allen J. Bard and Larry R. Faulkner. *Electrochemical methods: Fundamentals and Applications*. JOHN WILEY & SONS, INC., 1980. 2.1.2, 2.1.2
- [5] Tracy C. Britton, Rodney a. Stewart, and Kelvin R. O'Halloran. Smart metering: enabler for rapid and effective post meter leakage identification and water loss management. *Journal of Cleaner Production*, 54:166–176, September 2013. 4.1
- [6] Peter Bruesch. The electric double layer at a metal electrode in pure water. *Journal of Applied Physics*, 95(5):2846, 2004. 2.1.1

- [7] D Burgreen and F. R. Nakache. Electrokinetic flow in ultrafine capillary slits1. *The Journal of Physical Chemistry*, (1):1084–1091, 1964. 2.2.1
- [8] D. Burgreen and F. R. Nakache. Efficiency of Pumping and Power Generation in Ultrafine Electrokinetic Systems. *Journal of Applied Mechanics*, pages 675–679, 1965. 2.2.1
- [9] Chih-Chang Chang and Ruey-Jen Yang. Electrokinetic energy conversion in micrometer-length nanofluidic channels. *Microfluidics and Nanofluidics*, 9(2-3):225–241, December 2009. 2.2.1
- [10] Nancy Chang. Smart Gas And Water Meter Trends: Impacts on Meter Designs. *Metering International*, (4):38—39, 2012. 4, 4.1
- [11] David Leonard Chapman. LI. A contribution to the theory of electrocapillarity. *Philosophical Magazine Series 6*, 25:475–481, 1913. 2.1.2
- [12] Hirofumi Daiguji, Yukiko Oka, Takuma Adachi, and Katsuhiro Shirono. Theoretical study on the efficiency of nanofluidic batteries. *Electrochemistry Communications*, 8(11):1796–1800, November 2006. 2.2.1
- [13] Hirofumi Daiguji, Peidong Yang, Andrew J. Szeri, and Arun Majumdar. Electrochemomechanical Energy Conversion in Nanofluidic Channels. *Nano Letters*, 4(12):2315–2321, December 2004. 2.2.1
- [14] Christian Davidson and Xiangchun Xuan. Effects of Stern layer conductance on electrokinetic energy conversion in nanofluidic channels. *Electrophoresis*, 29(5):1125–30, March 2008. 2.2.1
- [15] Christian Davidson and Xiangchun Xuan. Electrokinetic energy conversion in slip nanochannels. *Journal of Power Sources*, 179(1):297–300, April 2008. 2.2.1

- [16] Jan C T Eijkel. Liquid slip in micro-and nanofluidics: recent research and its possible implications. *Lab on a Chip*, pages 299–301, 2007. 2.2.1
- [17] Elster. KENT V100T PSM Product Specifications, 2008. (document), 4.5
- [18] Freescale Semiconductor Inc. MC9S08QG8/4 Data Sheet, 2009. 5.1.2
- [19] L a Geddes. Historical evolution of circuit models for the electrode-electrolyte interface. *Annals of biomedical engineering*, 25(1):1–14, 1997. 2.1.2
- [20] Matthias Heinrich. Water End Use and Efficiency Project (WEEP): Final Report. Technical Report 159, BRANZ Ltd, 2007. 4.3
- [21] Matthias Heinrich. Water Use in Auckland Households: Auckland Water Use Study (AWUS). Technical Report October 2008, BRANZ Ltd and WaterCare Services Ltd, 2008. (document), 4.1, 4.3
- [22] Mark Donald Hill, Norman Paul Jouppi, and Gurindar Sohi. *Readings in Computer Architecture*. 2000. 5.1.2
- [23] Honeywell. Installation Instructions for the 26PC SMT Series Pressure Sensor, 2003. (document), 3.8
- [24] KW Horch and GS Dhillon. *Neuroprosthetics: theory and practice*. Volume 2 edition, 2004. 2.1.2
- [25] Jacob N. Israelachvili. *Intermolecular and Surface Forces*. Academic Press, 2011. 2.1.3
- [26] Zhijun Jiang and Derek Stein. Electrofluidic gating of a chemically reactive surface. *Langmuir : the ACS journal of surfaces and colloids*, 26(11):8161–73, June 2010. 2.1.3

- [27] Brian J Kirby and Ernest F Hasselbrink. Zeta potential of microfluidic substrates: 1. Theory, experimental techniques, and effects on separations. *Electrophoresis*, 25(2):187–202, January 2004. 2.2
- [28] AA Kornyshev. Double-layer in ionic liquids: paradigm change? *The Journal of Physical Chemistry B*, 2007. 3.1.1
- [29] Shahar Kvatinsky, Keren Talisveyberg, Dmitry Fliter, Avinoam Kolodny, Uri C. Weiser, and Eby G. Friedman. Models of memristors for SPICE simulations. In *2012 IEEE 27th Convention of Electrical and Electronics Engineers in Israel*, pages 1–5. IEEE, November 2012. 7.1.1.4
- [30] Ming-Chang Lu, Srinath Satyanarayana, Rohit Karnik, Arun Majumdar, and Chi-Chuan Wang. A mechanical-electrokinetic battery using a nano-porous membrane. *Journal of Micromechanics and Microengineering*, 16(4):667–675, April 2006. 2.2.1
- [31] G Mala. Flow characteristics of water through a microchannel between two parallel plates with electrokinetic effects. *International Journal of Heat and Fluid Flow*, 18(5):489–496, October 1997. 3.3
- [32] Malcolm Souness - WEL Networks. Private communication, 2012. 5.2
- [33] ET McAdams, A Lackermeier, J.A. McLaughlin, D. Macken, and J. Jossinet. The linear and non-linear electrical properties of the electrode-electrolyte interface. *Biosensors and Bioelectronics*, 10(1-2):67–74, January 1995. 7.1.1.3
- [34] Daniel R Merrill, Marom Bikson, and John G R Jefferys. Electrical stimulation of excitable tissue: design of efficacious and safe protocols. *Journal of neuroscience methods*, 141(2):171–98, February 2005. 7.1.1.3

- [35] B Meters. Hydrolink Remote Reading Systems, 2014. (document), 4.2, 4.1
- [36] Microchip Technology Inc. PIC12F629/675. Technical Datasheet, 2003. 5.1.2
- [37] Microchip Technology Inc. PIC16F/LF1826/27. Technical Datasheet, 2010. 5.1.2
- [38] R Morrison. RC Constant-Argument Driving-Point Admittances. *IRE Transactions on Circuit Theory*, 6(3):310–317, 1959. (document), 7.4, 7.1.1.2
- [39] W Olthuis, B Schippers, J Eijkel, and A Vandenberg. Energy from streaming current and potential. *Sensors and Actuators B: Chemical*, 111-112(April):385–389, 2005. 2.1.2, 2.2.1, 3.1.1, 3.1.2
- [40] JF Osterle. Electrokinetic energy conversion. *Journal of Applied Mechanics*, pages 161–164, 1964. (document), 2.2.1, 2.11
- [41] Sumita Pennathur, Jan C T Eijkel, and Albert van den Berg. Energy conversion in microsystems: is there a role for micro/nanofluidics? *Lab on a chip*, 7(10):1234–7, October 2007. 2.2.1
- [42] Python-ivi. python-vxi11, 2014. 3.3.1
- [43] Yongqiang Ren and Derek Stein. Slip-enhanced electrokinetic energy conversion in nanofluidic channels. *Nanotechnology*, 19(19):195707, May 2008. 2.2.1
- [44] CL Rice and R Whitehead. Electrokinetic flow in a narrow cylindrical capillary. *The Journal of Physical Chemistry*, 69(11), 1965. 2.2.1

- [45] G B Salieb-Beugelaar, K D Dorfman, A van den Berg, and J C T Eijkel. Electrophoretic separation of DNA in gels and nanostructures. *Lab on a chip*, 9(17):2508–23, September 2009. 2.1.2
- [46] Peter J. Scales, Franz Grieser, Thomas W. Healy, Lee R. White, and Derek Y. C. Chan. Electrokinetics of the silica-solution interface: a flat plate streaming potential study. *Langmuir*, 8(3):965–974, March 1992. 3.3
- [47] Jonathan Scott, Senior Member, and Peter Single. Compact Nonlinear Model of an Implantable Electrode Array for Spinal Cord Stimulation (SCS). *JOURNAL OF BIOMEDICAL ENGINEERING*, pages 1–8, 2013. 7.1, 7.1.1.3
- [48] Jonathan Scott and Peter Single. Compact nonlinear model of an implantable electrode array for spinal cord stimulation (SCS). *IEEE Transactions on Biomedical Circuits and Systems*, 8:382–390, 2014. 7.1.2, 7.3.1, 8.1
- [49] Otto Stern. Theory of the electrical double layer. *Electrochemistry*, 30:508–516, 1924. 2.1.2
- [50] Sir William Thomson. Sir W. Thomson on an Apparatus. *Philosophical Magazine and Journal of Science*, 34:391–396, 1867. A
- [51] Frank van der Heyden, Derek Stein, and Cees Dekker. Streaming Currents in a Single Nanofluidic Channel. *Physical Review Letters*, 95(11):9–12, September 2005. 2.2.1
- [52] Frank H. J. van der Heyden, Douwe Jan Bonthuis, Derek Stein, Christine Meyer, and Cees Dekker. Electrokinetic energy conversion effi-

- ciency in nanofluidic channels. *Nano Letters*, 6(10):2232–7, October 2006. 2.2.1, 2.2.1, 3.3, 6
- [53] Frank H. J. van der Heyden, Douwe Jan Bonthuis, Derek Stein, Christine Meyer, and Cees Dekker. Power generation by pressure-driven transport of ions in nanofluidic channels. *Nano Letters*, 7(4):1022–1025, 2007. 2.2.1, 2.2.1
- [54] I K Varga and R S Seymour. Observation of electrical effects with cavitating liquid flow. *Journal of Physics D: Applied Physics*, 19:2293–2300, 1986. (document), 3.2, 3.2.1
- [55] "Water New Zealand". Metering Overview, 2011. 4.1
- [56] Watercare New Zealand. Private communication, 2014. 4.3
- [57] Yanbo Xie, Xinwei Wang, Jianming Xue, Ke Jin, Long Chen, and Yugang Wang. Electric energy generation in single track-etched nanopores. *Applied Physics Letters*, 93(16):163116, 2008. 2.2.1
- [58] Chun Yang, D Li, and JH Masliyah. Modeling forced liquid convection in rectangular microchannels with electrokinetic effects. *International Journal of Heat and Mass Transfer*, pages 3118–3138, 1998. 3.1.1
- [59] J Yang, F Lu, LW Kostiuk, and DY Kwok. Electrokinetic microchannel battery by means of electrokinetic and microfluidic phenomena. *Journal of Micromechanics* . . . , 13:963–970, 2003. 2.2.1, 2.2.1
- [60] Jun Yang, Fuzhi Lu, Larry W Kostiuk, and Daniel Y Kwok. Electrokinetic Power Generation via Streaming Potentials in Microchannels: A Mobile-Ion-Drain Method to Increase Streaming Potentials. In Dr. Wael Badawy and Dr. Walied Moussa, editors, *International Conference on*

MEMS, NANO and Smart Systems, number 780, pages 675–679, Banff, Alberta - Canada, 2004. IEEE. 2.2.1

- [61] Gu Yongan and Dongqing Li. The ζ -Potential of Glass Surface in Contact with Aqueous Solutions. *Journal of Colloid and Interface Science*, 226(2):328–339, June 2000. (document), 3.1.1, 3.1.1, 3.2.1, 3.2.2, 3.3, 3.5, 3.5, 3.16